MODELLING THE EFFICIENCY OF AN AUTOMATED SENSOR-BASED SORTER

Submitted by

Ofonime Bassey Udoudo

to

The University of Exeter as a thesis for the degree of Doctor of Philosophy by research in Earth Resources, September 2010.

I certify that all materials in this thesis which is not my work has been identified and that no material has previously been submitted and approved for the award of a degree by this or any other University.

(Signature) .....

ABSTRACT

For future development of automated sensor-based sorting in the mining industry, an improvement in the separation efficiency of the equipment is desirable. This could be achieved through a better understanding of the identification and separation aspects of the automated sorter. For automated sorters that undertake separation through the use of compressed air jets, the problem of poor separation efficiency has been linked with co-deflection losses. Co-deflection losses occur as particles meant to pass on to the 'accept' bin are co-deflected with the particles (which are to be deflected) meant to go to the 'reject' bin.

To study co-deflection losses and suggest means of improving automated sorter separation efficiency, this research investigates the effects of particle size, shape, throughput, together with the proportion of particles (out of the total test batch) required to be deflected on separation efficiency. The effect of the air valve configuration on separation efficiency was also studied. Presented also is a mathematical model which could be used to predict automated sorter separation efficiency.

All separation efficiency investigations were undertaken using a TiTech Combisense© (BSM 063) automated sorter. Samples of granite were sized into -20+15mm, -15+10mm and -10+6mm size fractions and grouped into cubic and flaky shape fractions. These fractions were then divided into two with one portion painted for colour separation efficiency investigations.

The separation efficiency results confirmed earlier research indicating that particle size and the fraction requiring deflection affects separation efficiency, with separation efficiency decreasing with a decrease in particle size and an increase in throughput. It was observed that co-deflection loss occurs when correctly identified 'accept' particles are co-deflected due to their close proximity to 'reject' particles that are to be deflected. Observations from the tests indicate that an increase in the proportion of

particles requiring deflection increases the probability of finding ‘accept’ particles in close proximity to ‘reject’ particles leading to co-deflections.

Monte Carlo simulations were used to produce a random distribution of particles on the conveyor belt as would be obtained from actual investigations. From these simulations particle proximity relationships and particle co-deflections were studied. Results indicate that the Monte Carlo simulations under-predicts particle proximity associations.

The effect of shape on co-deflection was investigated with results indicating that flaky shaped particles produce higher number of co-deflections compared to cubic shaped particles. It was also observed that the valve sensitivity determined from valve opening and closing times is of importance to the selectivity (precision) of the separating air jets.

A mathematical separation efficiency model is presented which contains two variables, the belt loading (calculated using particle size, shape and throughput) and the particle fraction of the total test batch that are to be deflected (% deflection). The separation efficiency can be calculated once these two variables are determined.

ACKNOWLEDGEMENTS

I have enjoyed support and assistance from many parties too numerous to list here during the course of this research, my thanks to you all.

I thank my sponsors the Akwa Ibom State government. I also would like to thank my supervisors Dr. Richard Pascoe and Prof. Hylke Glass for their contributions and useful suggestions while undertaking this research. I also wish to express my thanks to Dr. Robert Fitzpatrick and Steve Pendray for helping in the laboratory; and to Stefan Juergensen of TiTech for helping with some of the technical information with respect to the automated sorter.

To my colleagues Adam, Dan, Edward, James, KP, Matt, Philip and Solomon thanks a lot for all the camaraderie we enjoyed and the various tips we shared to enhance the research experience. Finally to my wife, I say thank you dear for your patience and support as I spent long hours away from home undertaking this research. Glory to God!

LIST OF CONTENTS

Page No.

LIST OF FIGURES

Figure No.

Page

LIST OF PLATES

Page No.

LIST OF TABLES

Page No.

LIST OF ABBREVIATIONS AND ACRONYMS

2D: Two-dimensional

AOTF: Acousto-Optical Tunable Filter

CCD: Charge-coupled device

CYMK: Cyan-Yellow-Magenta-blacK

DE-XRT: Dual energy x-ray transmission

DMS: Dense medium separation

ELV: End of life vehicle

EM: Electromagnetic

FIR: far Infrared

HDPE: High-density polyethylene

LDPE: Low-density polyethylene

LED: Light-emitting diodes

LIBS: Laser induced breakdown spectroscopy

LIF: Laser induced fluorescence

MIR: mid Infrared

NIR: near Infrared

PET: Polyethylene terephthalate

PP: Polypropylene

PVC: Polyvinyl chloride

RGB: Red-Green-Blue

UV: Ultraviolet

WEEE: Waste electrical and electronic equipment

XRD: X-ray diffraction

XRF: X-ray fluorescence

XRT: X-ray transmission

YUV: Y (luma/luminance/brightness) UV (chroma) colour scale

LIST OF SYMBOLS

A = Absorbance of materials, m

B = Magnetic induction, T

B_L = Belt loading, %

c = Velocity of electromagnetic radiation in a vacuum, ms^{-1}

— = Magnetic field gradient, T/m

ΔE = A quantum (photon) of energy, J

E_{electr} = Energy associated with the electrons in the various outer orbitals of the molecules, J

E_{over} = The overall energy, J

E_{rot} = Energy associated with the rotation of molecules about the centre of gravity of the atom, J

E_{vib} = Energy due to inter-atomic vibrations, J

F = The magnetic force, N

H = Magnetic field strength, A/m

h = Planck's constant, 6.626 x 10^{-34} J

I = intensity of light transmitted through the sample at a given wavelength, m

I_o = intensity of incident light on the sample at a given wavelength, m

k = volume magnetic susceptibility

N_d = blue deflect, %

R_b = Recovery of blue painted particles, %

R_g = Recovery of granite particle, %

S.E = Separation efficiency, %

Tot_E = Total efficiency, %

λ = Wavelength of the electromagnetic radiation, m

μ = Magnetic permeability, H/m

CHAPTER 1

INTRODUCTION

1.0 THESIS STRUCTURE

This thesis is divided into 7 Chapters with 3 Appendices. Chapter 1 states the aims of the research, gives a background to the research together with a summary of the research methodology.

Chapter 2 reviews the literature on the subject of automated sensor-based sorters looking at the feeding and presentation, identification and classification, and separation components. The applications of sensor-based sorters (also referred to as automated sorters in this thesis) and challenges to improve the separation efficiency are also discussed. Other subjects reviewed include dense medium separation which is a competing technology with sensor-based sorting as a mineral pre-concentration tool; a previous performance model, and Monte Carlo analysis stating some of its applications in mining related research. Lastly, the analytical method applied in the research to measure separation efficiency is also described.

Chapter 3 describes the automated sensor-based sorter utilised for the separation efficiency investigations, including how the sorter was set-up for investigations. In Chapter 4 the sample preparation and experimental test procedures (including the optimisation, calibration and setting-up test procedures undertaken in all the separation efficiency investigations) are described. Lastly, particle size and surface area data obtained from the image processing analyser (a particle characteristics recorder) of the sensor-based sorter are presented.

Chapter 5 presents the results of the separation efficiency investigations indicating the effects of throughput, particle size and shape on sorter separation efficiency. The Monte Carlo procedures and results are also presented in this Chapter.

Chapter 6 presents the proposed model which is based on two variables: number of particles on the belt (belt loading) and fraction of particles required to be deflected. The model validation test procedures are described together with the presentation of the validation test results. Chapter 7, the last Chapter discusses the research conclusions and recommendations for further research.

1.1 AIMS OF STUDY

The aims of the study were to:

- Study the separation aspects of our automated sorter investigating particle interactions (such as “touching” particles) at the identification point of the automated sorter and relating this information to separation efficiency.
- Suggest recommendations to achieve a better separation for our automated sorter through the study of the effect of various particle sizes and shapes at varying throughput.
- Produce a mathematical model to predict automated sorter efficiency based on material and automated sorter (machine) properties. Material properties considered were colour, size, shape and throughput (belt loading). The model was calculated based on optimal automated sorter properties including deflection air pressure and valve deflection configuration.

1.2 BACKGROUND AND JUSTIFICATION OF RESEARCH

The application of sensor-based sorters for separation purposes in the mining industry is over a century old with the major sub-processes (feeding and presentation, identification and classification, and separation) being the subject of research (Arvidson, 2002; Salter and Wyatt, 1991; Schapper, 1977). Each sub-process contributes to separation efficiency to various degrees. To achieve higher throughputs particles are typically presented for identification on fast moving conveyor belts or from the discharge of a chute. The conveyor belt length is designed to allow the presented particles time to settle on the belt before reaching the identification sensors. Some manufacturers have fitted stabilising belts over the conveyor belt to force the particles to remain stationary (Schapper, 1977).

Advances in spectroscopy has increased the types of sensors available for sorting from the earlier x-ray attenuation and radiometric sensors to ultraviolet, visible and infra-red sensors (Salter and Wyatt, 1991). Suppliers of automated sensor-based sorters now offer up to three cameras fitted in a way to ensure 360° identification making it possible to identify objects as small as 4mm at throughputs ranging between 1 and 5tonnes/hr (Bayram and Oner, 2006; Delwiche *et al,* 2005). This design is useful when sorting particles with heterogeneous composition. The challenges associated with the speed of identification of particles have been addressed with an improvement in computing speed allowing for faster processing of information acquired by the sensors. Faster processing also indicates that higher throughputs of particles could be processed (Manouchehri, 2003).

Separation of particles following identification is typically achieved using compressed air jets. Other means include water jets, suction valves and mechanical flaps (Forsthoff, 2000; Pascoe, 2000). The mechanical flaps which deflect particles at the slowest rate are utilised mainly for coarse sized particles. The sensitivity of the air jets, associated with the opening and closing times of the air valves is an important variable in the effectiveness of the sorting process. Another factor is the sizing (longest/shortest diameter) of the particles. This is to allow for accurate particle deflection by the compressed air jets. The top/bottom sieve size

ratio representing the longest/shortest diameter is typically 3:1 (Arvidson, 2002).

Automated sensor-based sorting has been utilised in the mining industry for the separation of gemstones such as tanzanite and diamonds from gangue. Other applications include the pre-concentration of metallic sulphide ore, together with the upgrading of marble (Arvidson, 2002; Arvidson, 1998; Salter and Wyatt, 1991). However, despite these applications automated sensor-based sorting is not widely used in the mining industry when compared to the recycling or food processing industries. Applications in the recycling industry include the separation of plastics, glass and scrap metal (Mesina *et al*, 2007; De Jong and Fabrizi, 2004; Cutmore and Eberhardt, 2002; Salter and Wyatt, 1991).

It has been suggested that the application of automated sensor-based sorters in the mining industry has been limited due to high installation and operational cost, poor separation efficiency when compared to other pre-concentration methods and the complex technical nature of the sorter (Cutmore and Eberhardt, 2002; Salter and Wyatt, 1991).

The relatively high cost of installation and operation are subject to variables such as mine location and placement of the sorter in the mineral processing plant design flowchart. Cost is also linked to material type. Gemstone production for instance could find the use of the sorter ideal for pre-concentration purposes when compared to talc production. This is based on the assumption that exploited gemstones could easily pay for the cost of automated sorter installation.

The limitations of poor performance and the sensor-based sorters' complex technical nature can be overcome with a better understanding of the presentation and separation method. This study is an attempt to provide a better understanding of the separation aspects of the sorter through the study of the effects of particle and automated sorter characteristics on the sorter separation efficiency.

Research by Arvidson (2002); Salter and Wyatt (1991) and King (1978) identified the presentation, identification and separation components to be important to separation efficiency with poor presentation or separation leading to separation losses. This research sought to determine the effects of particle size on separation efficiency also studying separation “dilution” (co-deflection loss), which occurs when a correctly identified ‘accept’ particle is inadvertently co-deflected with a ‘deflect’ particle as a result of “touching” particles. These particles may appear as ‘composites’ of two or more particles at the identification point.

The effect of particle shape on co-deflection previously not documented is also presented in this thesis. Another area of interest of this research was the sensitivity of the separation system (compressed air jets), due to the fact that the particles may be identified correctly but get co-deflected due to poor sensitivity of the separation system. This is the first time that the factors that affect deflection efficiency have been quantified and presented in literature.

This research also set out to produce a mathematical model to calculate automated sorter separation efficiency for our automated sorter. The mathematical model is based on two variables: the percentage of materials that requires deflection and material belt loading. A quantitative model for the determination of automated sorter separation efficiency was proposed by King (1978). The model utilised experimentally determined identification and deflection probabilities. In this research the King model has been improved with identification and deflection probabilities obtained from a colour camera based automated sorter. Identification probabilities were simplified to a value of approximately 1, by painting the samples with a clearly identified colour. Deflection probabilities were obtained at varying machine and material properties such as size, shape and belt loading/throughput.

1.3 RESEARCH METHODOLOGY

Separation efficiency tests and measurements of identification and deflection probabilities were undertaken using a TiTech Combisense sensor-based colour sorter on granite samples collected from the Carnsew aggregate quarry in Penryn, United Kingdom.

The effects of material size were studied using fine (-10+6mm), intermediate (-15+10mm) and coarse (-20+15mm) size fractions. The intermediate and coarse size fractions were further classified into flaky and cubical shape fractions utilising Lees (1964) aggregate classification method. To achieve identification probabilities of approximately 1, half of the samples were painted blue. Blue was determined to be ideal as there was none of this colour in the natural granite. The colour of the natural granite was grey (some particles had reddish hue).

The camera of the automated sorter operates using reflected light identifying particles when they come off the conveyor belt over a lit background, hence a background colour which will contrast with the particle colours had to be selected. The background colour was determined to be green by inspection on a Y-(brightness) U-V (chroma) colour space as this colour did not interfere with the painted and natural granite (more in Chapter 4).

The separation efficiency tests involved measuring the efficiency of separation for each size and shape fraction at varying throughputs and fraction of the blue particles requiring deflection (% deflection). This was after the optimal automated sorter conditions (delay time, splitter positioning and air pressure) were determined. The delay time is the processing time (for image processing and valve activation) between particle identification and deflection. That is from the line of sight of the camera to the bank of compressed air nozzles. The splitter positioning allows for separation of particles into the two collector bins while the air pressure determines the amount of compressed air released to the valves to deflect particles. Separation efficiency was calculated using the methodology suggested by Dodbiba *et al*, (2004).

The separation efficiency tests were configured such that the blue particles were always deflected. From these tests, it was observed that the recovery of blue particles was generally >99% which meant that the cause of poor separation efficiency was related to deflection inefficiencies. These inefficiencies were observed to be related to particle "touching" and forming composites especially where the composite contained a blue particle, because the blue particles were programmed to be deflected.

To study the probability of composite formation, it was necessary to measure the average area a particle occupies on the belt and use this information to determine the area of the belt that two or more particles would occupy. To ensure that the particles do not rest on top of each other approximately 1000 particles of each size and shape fraction was passed one-by-one over the automated sorter. The particle characteristics such as size and surface area were obtained from the image processing analyser of the automated sorter. The average surface area calculated was taken to represent the cut point surface area of a single particle. Through an iterative process discussed further in Chapter 4, sub-section 4.2.4 the area that particles of a given throughput would occupy was determined (assuming that the particles don't rest on top of each other). The results obtained were used to determine the composites and separation inefficiency (co-deflection) relationships.

Composite formation was also simulated using Monte Carlo simulation. Firstly the particle size was calculated based on the sieve size and particle thickness. The area a particle occupies on a belt was then calculated. An area representing the actual belt configuration for a test batch was simulated using Monte Carlo analysis. The random number generator of Microsoft *Excel*© software was used to generate random numbers and allocate particles into a grid corresponding to the determined area. Within this area using the belt coverage data, particle classification (whether an 'accept' or 'reject') was undertaken from which the number of composites were predicted. Particle classification is discussed in detail in Chapter 5 sub-section 5.2.5. This data was compared with actual composite data obtained from the image processing analyser.

The relationship between the calculated belt loading and actual co-deflection data was used to calculate the proposed model discussed further in Chapter 6. The model was then validated by undertaking separation efficiency tests following similar procedures described in Chapter 4, sub-section 4.1 and 4.2.

CHAPTER 2

LITERATURE REVIEW

This Chapter reviews literature on the subject of automated sensor-based sorting discussing the major components found in the various automated sorter designs together with their applications. Some other topics reviewed are the challenges to achieving a high separation efficiency of the automated sorter, a competing technology to automated sorting and a previous model used to determine sorter performance based on deflection and identification probabilities.

2.0 SENSOR-BASED SORTER COMPONENTS AND CONFIGURATIONS

A sensor-based sorting system consists of four main components (Arvidson, 2002; Salter and Wyatt, 1991; King, 1978):

a) a feeding system
b) a presentation system
c) an identification system
d) a separation system

Figure 2.1 shows the typical order of operation (from 1 to 4) of a sensor-based sorting system.

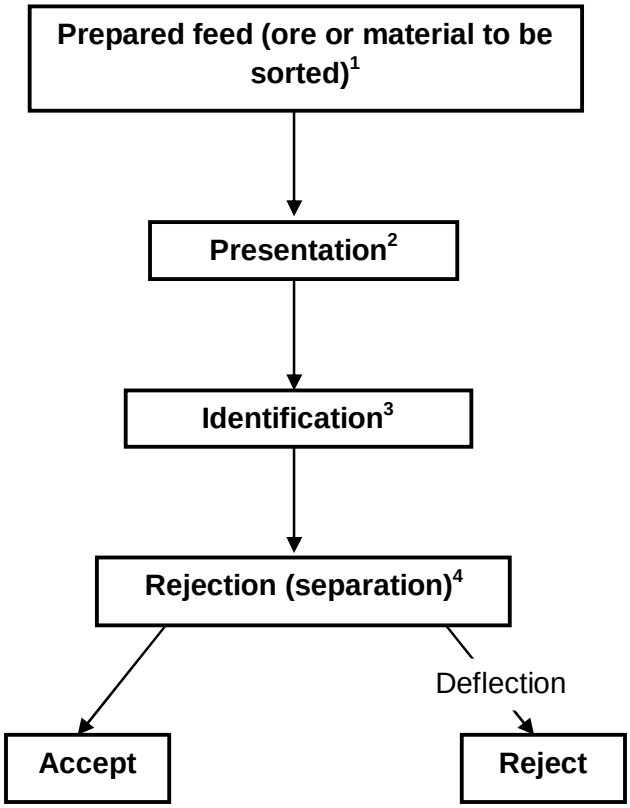

Figure 2.1: Schematic flow sheet of a typical sorting system

2.0.1 The feeding and presentation systems

Well designed feeding and presentation systems are important for the operation and achieving of a high separation efficiency of automated sorting. Usually the feed travels onto a chute before being transported to the presentation system. The chute design is important to material acceleration and stabilisation on the belt. This is because the feed particles should not bounce as they come off the chute eliminating the tumbling (or tracking) of particles as they meet the conveyor belt (Stuart-Dick and Royal, 1992). Ideally the particle should leave the chute close to the belt speed.

Schapper (1977) noted that particles of feed materials need to be presented individually to achieve adequate identification and appropriate deflection after identification. According to Arvidson (2002) the size of the materials should conform to a 3:1 or 2:1 ratio of top size to smallest size in the feed. This ratio is linked to correct valve and pressure selection to ensure efficient separation.

The presentation system is designed to aid the feed materials travel to the identification zone. Designs of feed presentation systems include free fall from a chute, discharge from a conveyor belt or the use of rotatory discs as shown in Figures 2.2 and 2.3. Other designs applied to low throughput high separation efficiency conditions such as sorting of seeds have the feed come off the chute onto channelled (constricted) conveyor belts which transport the materials for identification (Blasco *et al,* 2009).

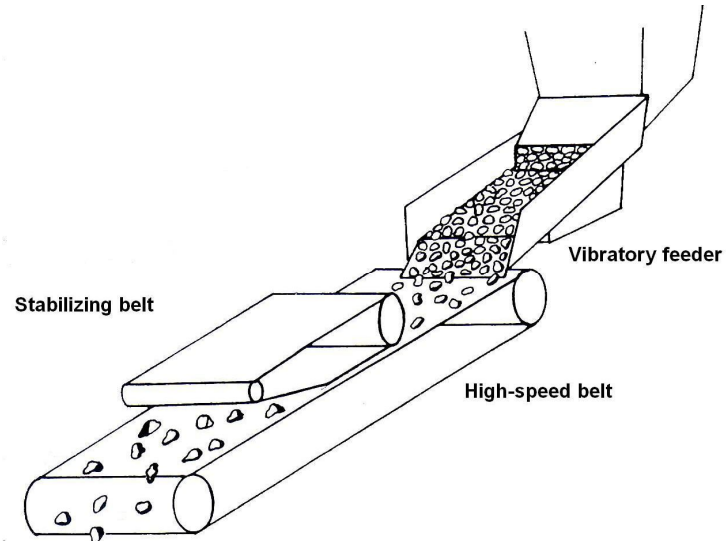

Figure 2.2: The feed and presentation system - conveyor belt configuration (from King, 1978)

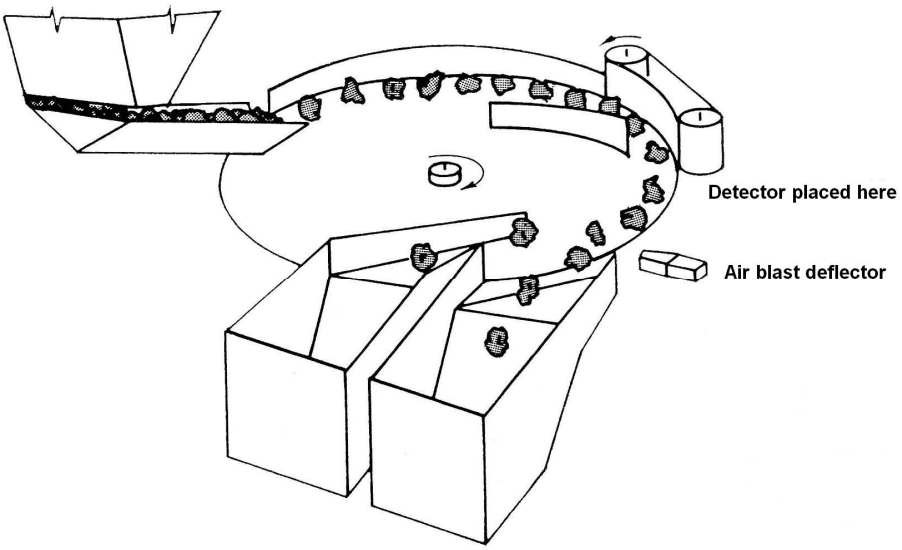

Figure 2.3: The feed and presentation system - rotatory disc configuration (after King, 1978)

In a free fall configuration, the feed particles are transported from the feed trough which spreads out the particles from where they free fall under the influence of gravity to an identification and separation zone (see Figure 2.4). An advantage of this configuration is the ease of coupling two cameras for triaxial (360°) identification (CommoDas, 2006). This configuration is also advantageous for mineral processing operations that have a space constraint, as it requires less floor space to set up.

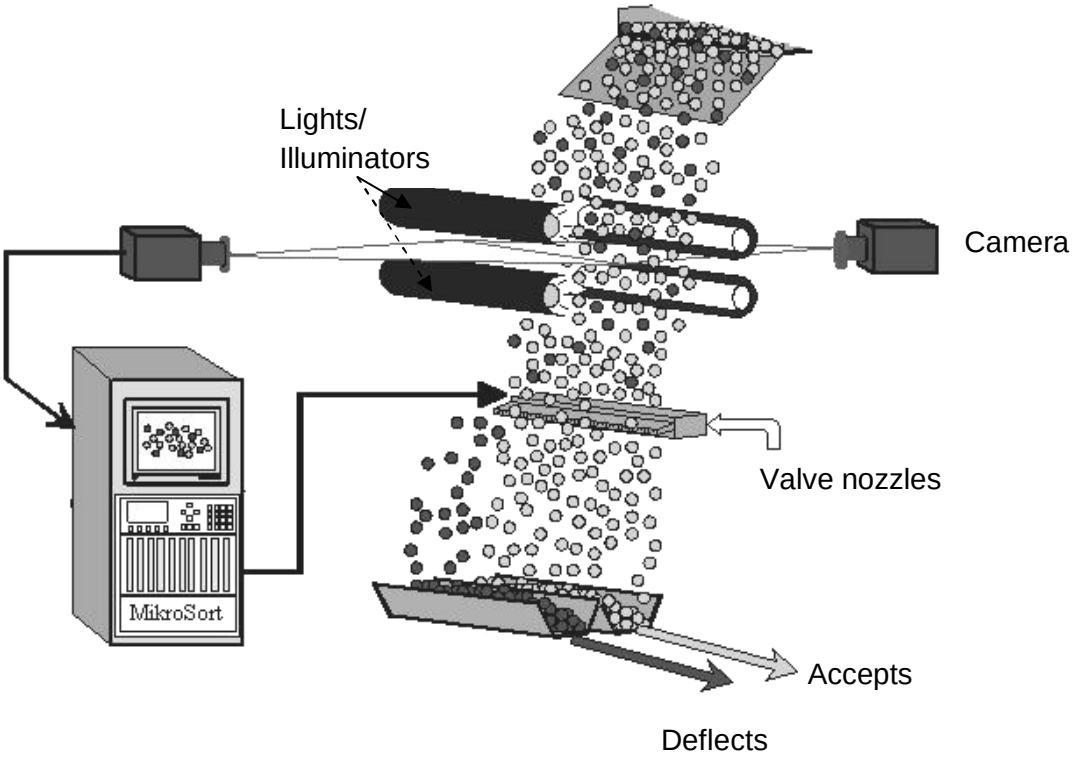

Figure 2.4: The presentation system in free fall configuration (from CommoDas, 2006)

De Jong and Harbeck (2005) suggested that the sample size could be used as a guide for the presentation design with 40 to 250mm size fraction presented in free fall while 2 to 40mm fraction are presented by discharge from a conveyor belt.

The conveyor belt (on-belt) configuration is another design. In this design the feed particles are passed onto a conveyor belt, from which the typical distance a particle travels is between 2 to 5m. This distance is meant to achieve feed stability for identification and minimise the amount of overlapping feed particles. Feed stability has been a challenge of this design. Previously, some of the automated sorter designs had stabilisation belts above the main conveyor to stabilise the particles. The particles were compressed into the soft belt, which formed a mould around the particles (King, 1978). This design feature is not found in current automated sorters as the design hampered the ability to achieve higher throughputs with greater wear and tear on the conveyor belts. Some suppliers utilise conveyor belts designed like a continuous wire mesh (referred to as gravity

conveyors) which they suggest overcomes the limitation of feed instability on the belt (KEY, 2010).

2.0.2 The identification system

The identification system comprises the sensor array with sensors such as conductivity sensors, monochromatic, colour or infrared cameras; as well as lighting sources such as fluorescent and light-emitting diodes (LED) lighting. The sensors could be placed underneath or overlooking the conveyor belt. For automated sorters with a free fall design, the sensor is placed in the trajectory of flight of the material.

According to Skoog *et al,* (1996) each material that requires sorting must have properties that can be utilised for identification and classification. Information such as size, shape, colour and brightness could be obtained. Figure 2.5 shows the various material properties which may be measured and or classified.

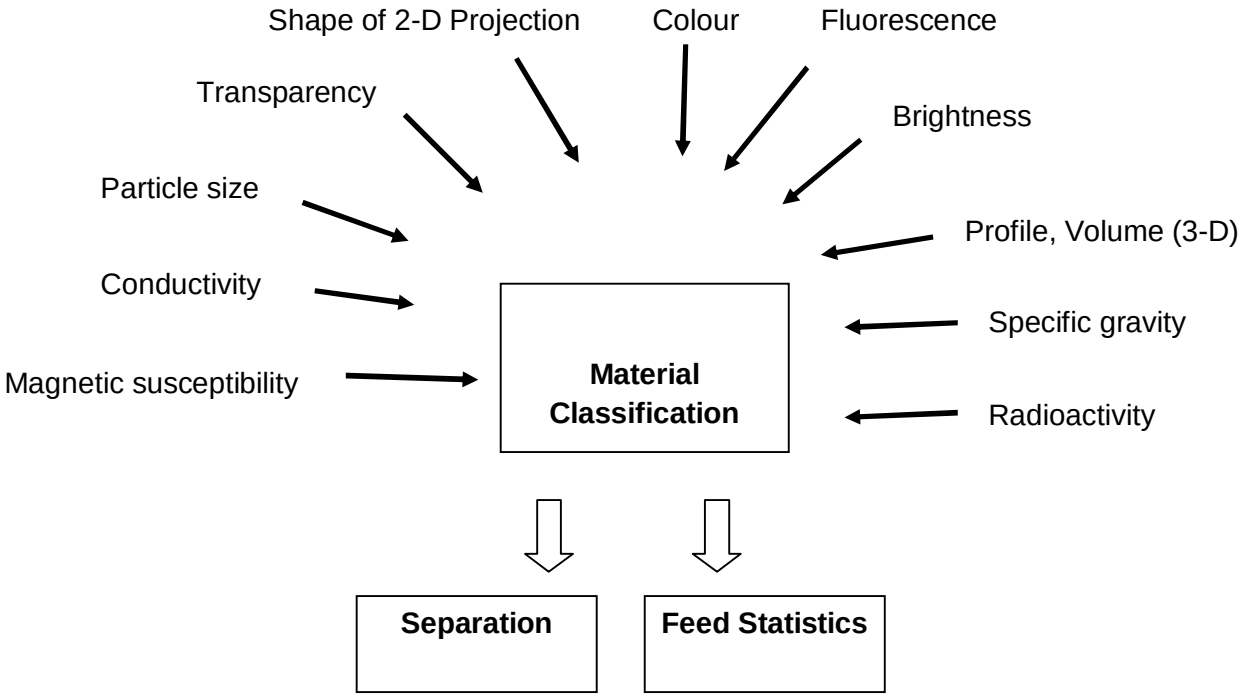

Figure 2.5: Some material information that could be used for identification classification and sorting (after Manouchehri, 2006; Arvidson, 1988)

This information forms the basis for separation of the object identified. For instance a sensor which measures radioactivity would identify radioactive ore such as uranium or its daughter products and could then be utilised to separate the uranium rich ore from gangue.

According to Kattentidt *et al* (2003) the performance of automated sorting equipment could be improved if quality data is obtained from the fitted sensor(s). As such some recent automated sorters have been fitted with multiple sensors. The processing speed and accuracy of data obtained from the sensor array is of importance. Having a good balance between processing speed and efficiency of identification is also essential.

Data processing involves the application of image processing procedures. Figure 2.6 is a schematic of the image processing procedure, which broadly represents the "material classification" portion in Figure 2.5.

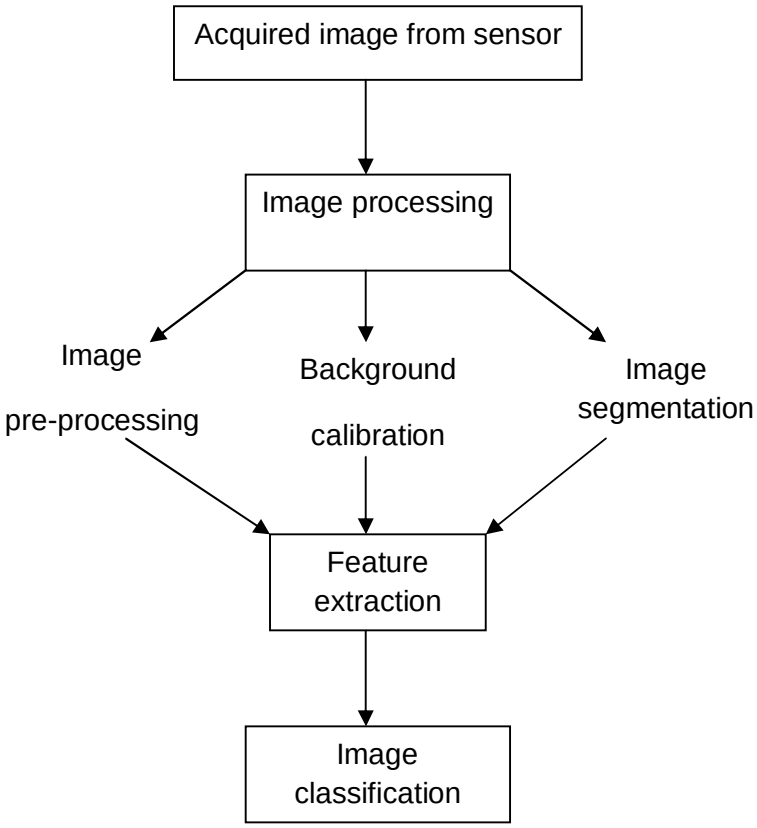

Figure 2.6: Schematic of the image processing procedure(s) (after Kattentidt *et al* 2003, Cinque and Lombardi, 1995)

For a sensor such as a camera, the acquired image is pre-processed to remove noise and distortions. The measure of light intensity of the object is utilised to gather information in pixels (picture elements). The background has to be separated from the image together with other objects in the image (image segmentation). Afterwards the image features are extracted (Acharya and Ray, 2005; Kattentidt *et al* 2003; Gonzalez and Woods, 1992). Following feature extraction, depending on the pre-defined classes, the images are then classified. This information is then utilised for the separation of the materials.

2.0.2.1 Sensors applied to sorting

The fields of spectroscopy, artificial intelligence, optics and mathematics have contributed to sensor design. The process of design may progress from a laboratory to the pilot plant and then full scale commercial production. Some of sensor designs utilise electromagnetic radiation, others measure conductivity and magnetic susceptibility. Sensors based on

the electromagnetic spectrum are more common. A schematic of the general working principle of a sensor utilising energy reflection is shown in Figure 2.7.

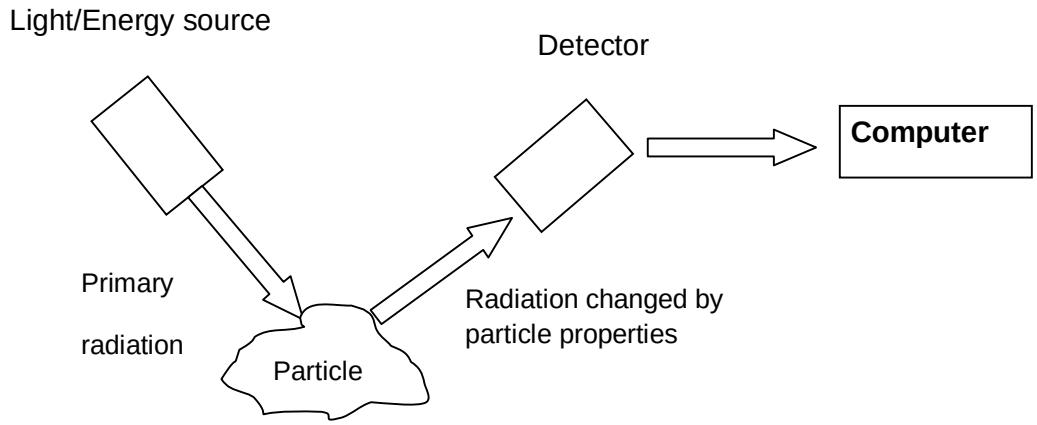

Figure 2.7: The general working principle of a sensor (after Killmann and Pretz, 2006)

Theory of Electromagnetic radiation: Electromagnetic energy is observed in numerous forms such as visible light, heat energy and invisible (to the human eye) forms such as x-rays. The properties of electromagnetic radiation are described by a sinusoidal wave model (see Figure 2.8) and as discrete wave packets of energy called photons (Skoog *et al,* 1996). The magnetic field vector is at right angles to the electrical field vector which is shown in Figure 2.8.

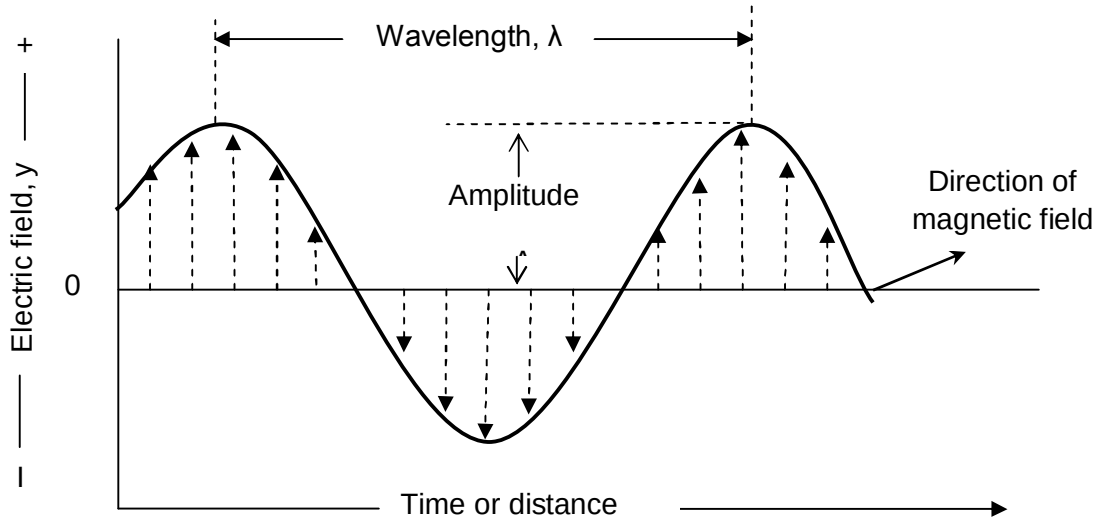

Figure 2.8: Two-dimensional representation of the electromagnetic vector (after Skoog *et al*, 1996)

Energy transition between energy states leads to the formation of all spectra. A change in internal energy occurs when a molecule absorbs or emits electromagnetic (EM) radiation (Straughan and Walker, 1976). A measure of the transmitted spectrum indicates the portion of the incident beam of energy that has been absorbed by the material (Brockington *et al,* 1985). Molecules in the path of the incident beam will collide with photons. A quantum (photon) of energy (ΔE) is related to the wavelength (λ) of radiation by:

$$\Delta E \text{ (J)} = \frac{hc}{\lambda} \qquad (2.1)$$

Where

h = Planck's constant (6.626 x 10^{-34} J)

c = Velocity of electromagnetic radiation in a vacuum (ms^{-1})

λ = Wavelength of the electromagnetic radiation (m)

According to Skoog *et al* (1996), when a material decreases the intensity of certain frequencies of the electromagnetic spectrum, absorption is said to occur. A photon of radiation causes a sample ion or molecule to be converted to a higher energy (excited) state and emits fluorescent energy or heat (through vibrational and rotational motions), then it returns back to

its ground (non-excited) state after some time. The relationships of these excited state is shown in Figure 2.9.

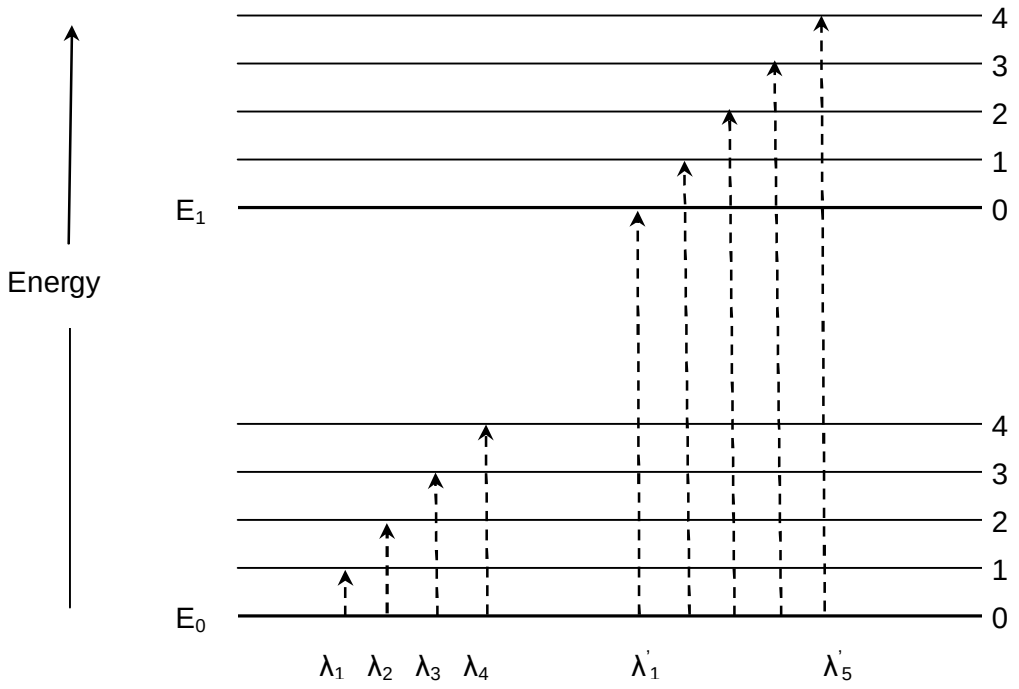

Figure 2.9: Schematic of energy states/changes that occur during molecular absorption (after Skoog *et al*, 1996)

The overall energy (E_{over}) that may be emitted by the material may be represented by equation 2.2.

$$E_{over} = E_{electr} + E_{vib} + E_{rot} \quad (2.2)$$

Where

E_{electr} = is the energy associated with the electrons in the various outer orbitals of the molecules (J).

E_{vib} = is the energy due to inter-atomic vibrations (J).

E_{rot} = is the energy associated with the rotation of molecules about the centre of gravity of the atom (J).

Beer's law (see Equation 2.3) indicates the relationship between light absorption and the amount of incident light absorbed by the medium the light passes through (transmittance), and is important for sensors that measure the absorbance (A) of materials (Skoog *et al* 1996).

$$A(m) = -log_{10} \frac{I_o}{I}$$

(2.3)

Where

I_o = intensity of incident light on the sample at a given wavelength (m)

I = intensity of light transmitted through the sample at a given wavelength (m)

The various modes of measurement of light energy are shown in Figure 2.10.

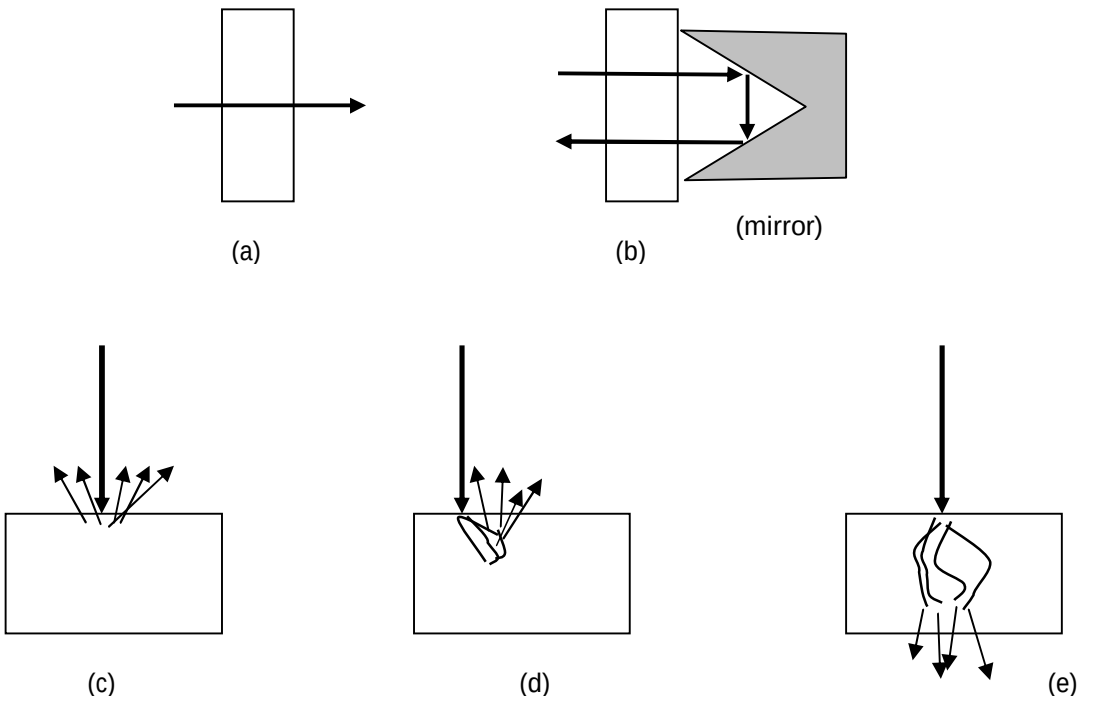

Figure 2.10: Modes of light energy measurements a) transmission; b) transflectance; c) diffuse reflection; d) interactance; e) transmission through scattering medium (after Pasquini, 2003)

Now discussed are two broad modes of energy measurement: reflection and transmission, which are applied in spectroscopy to classify and identify materials.

Reflection: Feed material can reflect waves when wave energy from a light source is incident upon it (see Figure 2.10). A material could emit photons (fluorescence) by reflection in response to wave energy incident upon it.

For instance white light which comprises all the colours of the electromagnetic spectrum incident on an opaque object will reflect the object colour back to the human eye or camera.

Transmission: Occurs when wave energy passes through a material and the sensor measures the wave intensity of the deflected wave. Transmission occurs through wave refraction. Some x-ray sorters use this principle (De Jong *et al,* 2005).

Electromagnetic radiation based sensors and classification devices:

The electromagnetic spectrum is divided into seven major regions (see Figure 2.11). A summary of the region specific sensors and their applications is outlined below.

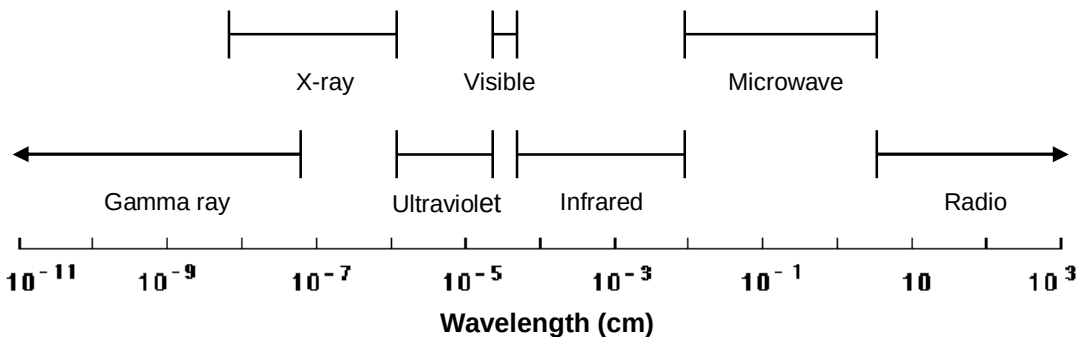

Figure 2.11: A diagram of the electromagnetic spectrum (after Skoog *et al*, 1996)

Generally all the sensors follow a specific design which includes a source of the energy, a system which disperses the light energy (monochromator) and a detector which measures the absorbance through or reflectance from the sample material. The source could be natural light, deuterium arc lamps or tungsten filament lamps depending on the sensor type. The wavelength of the incident energy is split using a monochromator which could be a prism or a diffraction grating (See Figure 2.12). The detector could be a scintillation counter or photomultiplier tube (Denney and Sinclair, 1987).

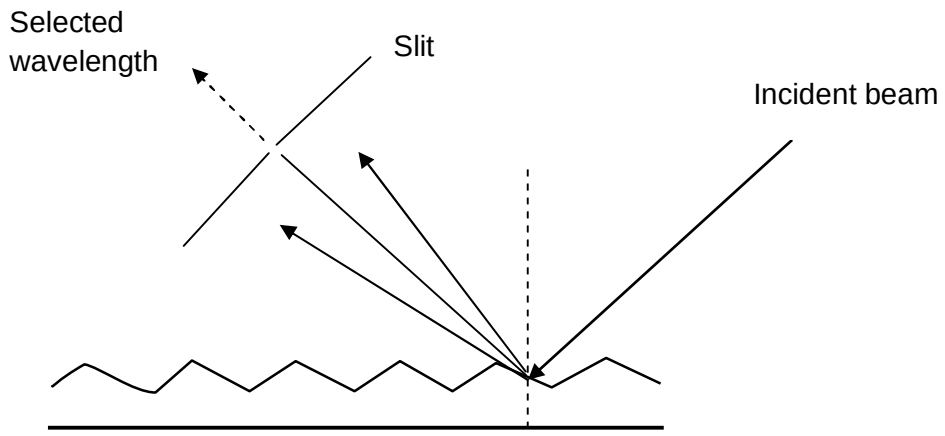

Figure 2.12: Monochromation by a diffraction grating (after Denney and Sinclair, 1987)

Gamma sensors: Gamma waves have a wavelength of less than 0.01 nanometres (nm). A radioactive nucleus emits energy as a result of radioactive decay or induced nuclear reactions. The intensity of emissions are then measured by the detector/sensor and utilised for material identification (Adams and Gasparini, 1970).

Automated sorters fitted with gamma sensors have been utilised to identify radioactive minerals that are composed of radioactive elements such as the daughter products of uranium. The Kelly and Hutter (K+H) M6/M17 sorters were used at the Mary Kathleen Uranium Company (Bibby, 1982) for separation of uranium rich ore from gangue. Gamma sensors were utilised to separate gold ore where the gold was hosted in uranium bearing ore (Salter and Wyatt 1991; Arvidson, 1988). The gamma sensor-based method is sometimes referred to as radiometric sorting.

X-ray sensors: X-rays are waves with wavelength from 0.01 to 10nm. X-rays originate from the electron cloud surrounding the nucleus of the sample material (Adams and Gasparini, 1970). Excitation produces energy when a sample material is irradiated. The intensity of the emission at a specific wavelength can be measured and utilised for material identification. The intensity of emission can also be linked to elemental concentration using a calibration procedure (Goldbook, 2009).

There are various analytical methods that utilise x-rays including x-ray diffraction (XRD), transmission (XRT) and fluorescence (XRF). XRD involves diffraction by crystalline materials to obtain their crystal structure. XRF involves the detection of elemental information through re-emission of the incident radiation on a material (Straughan and Walker, 1976). An advantage of XRF is its ability to differentiate similarly coloured plastics (Dalmijn and De Jong, 2004). Other sensors based on the use of x-ray methods include XRT and dual energy x-ray transmission (DE-XRT). DE-XRT determines the average atomic number as well as the approximate volume of material to be separated while XRT determines mainly the internal structure of material (Dalmijn and De Jong, 2004; Mesina *et al*, 2007).

For DE-XRT, two x-ray beams of differing energy level irradiate the material to be identified. As XRT measures material thickness, it can be limited for very thick materials where the penetration of the x-rays could be dampened (Fleischer and Bergmann, 2004). Due to the fact that the intensity of x-ray transmission depends on the material density and thickness which are not surface properties, x-ray sensor measurements are not affected by dust as is the case with surface properties such as colour (visible light).

OPTICAL SENSORS: Due to similarities in instrumentation and interactions with matter, ultraviolet, visible and infrared sensors are sometimes referred to as optical sensors (Skoog et al, 1996). Some of these sensors have been combined in some sorter designs for multispectral identification (Delwiche *et al*, 2005; Dowell *et al*, 2002).

Ultraviolet sensors: Ultraviolet (UV) sensors make use of the 10 to 400nm wavelength range. Electrons in certain materials are excited when exposed to UV light. Such materials absorb light energy at wavelengths corresponding to electron transition (Skoog *et al*, 1996). The sensors detect UV light reflected (fluoresce) or transmitted from the material to be identified. The intensity of the absorption signal can be analysed to obtain material information.

Ultraviolet (UV) sensors can identify fluorescence. UV-VIS which is a combination of ultraviolet and visible light sensors has been utilised for the

measurement of firmness and defects in satsuma mandarins (Gomez *et al*, 2006).

Visible light sensors: This is the range the human eye is sensitive to, with wavelengths ranging from 400 to 700nm. Cameras are the common sensors of this spectral range. The sorter utilised in this research is fitted with a colour line scan camera measuring light intensity in colour (Red-Green-Blue). The operating procedure of this sorter is discussed in detail in Chapter 4.

Visible light sensors may be utilised for a wide variety of applications including the separation of plastic, gemstones, industrial minerals, glass and grain (Anselmi and Harbeck, 2000; Zeiger, 2005; Pascoe, 2000; Dowell *et al,* 2002; Delwiche *et al*, 2005). The surface of the samples to be identified has to be clean, which can be a disadvantage in applications where there may be fine particles on the surface.

Infrared sensors: The infrared range comprises wave energy with a wavelength ranging between 700nm and 1.5mm. It can be further divided into the near, mid and far infrared ranges. The near infrared (NIR) ranges from 700 to 2500nm, the mid infrared (MIR) wavelength ranges from 2500 to 5000nm and the far infrared (FIR) ranges from 5000nm to 1.5mm.

The material to be identified is irradiated with infrared light energy and the absorbance and or transmitted intensity measured. This intensity represents the atomic and chemical bonding of the material and is usually recorded as a pattern of peaks and troughs corresponding to the frequencies of the radiation that were most highly absorbed (Krummenacher *et al*, 1998; Skoog *et al*, 1996). The intensity signature of each material can then be compared against a predetermined signature database for material identification (Bruno, 2000). This absorbance signature is usually over the whole wavelength range.

Other designs such as the Acousto-Optical Tunable Filter (AOTF) NIR sorter achieves faster processing time as the filter can be tuned to only suitable

wavelengths (UNICE, 2009). Thus when measuring absorbance for a polymer of known response wavelength range, only that range is measured.

Specific material properties may be best identified in one of the three ranges (near, mid or far-infrared). For instance, NIR sensors are applied for plastics separation (Polyethylene terephthalate {PET} from Polypropylene {PP}) because of its speed of identification and sorting when compared to the mid infrared which have a slower processing speed (Pascoe, 2000). Sensors designed in these three ranges of the infrared spectra have been utilised for the classification and sorting of car components (Pascoe, 2000; Leitner *et al*, 2003). Others have also been utilised for classification and separation purposes in the mining, pharmaceutical and agricultural industries (Serranti *et al*, 2006; De Jong *et al,* 2005; Dowell *et al*, 2002).

Research indicates that the absorbance peaks of plastics (High-density polyethylene {HDPE}, Low-density polyethylene {LDPE} and PET) are more distinct than those of minerals in infrared spectroscopy (USGS, 2006). This may be due to homogeneity of composition as minerals may have varied composition which could mask other spectra (Gaydon *et al,* 2009).

Other identification techniques which have been applied to ore characterization and classification include spectroscopic methods such as laser induced fluorescence (LIF) and laser induced breakdown spectroscopy (LIBS).

For LIF, the material to be examined is excited with a laser pulse, causing the material to emit photons through energy reflection. The fluorescence of the emitted photon is then measured with a detector. In Kiruna, Sweden, LIF has been applied to bulk sort iron ore. The phosphorous content of buckets of iron ore is measured and those buckets with an excessively high phosphorus content are not processed (MRA, 2004).

For LIBS the material to be examined is excited by a laser pulse causing a small portion of the material to be ablated in a plasma plume. The ablated material breaks down into excited ionic and atomic species which are then measured by a detector. Mesina *et al* (2007) stated that LIBS has been used to sort steel from metal alloys. LIBS has also been applied for

separating non-ferrous metals from heavy media separation plants (Nijkerk and Dalmijn, 1998).

Raman spectroscopy is another identification technique. The material to be examined is excited with a laser pulse. The low-frequency vibrational and rotational behaviour of the interaction of the atoms in the material is measured and used for material identification. Raman spectroscopy is similar in operation to infrared (IR) spectroscopy, except that Raman spectroscopy measures the scattered light of excited molecules responding to incident energy while infrared measures the absorption of incident energy (Straughan and Walker, 1976). Lamprecht *et al* (2007) discussed the application of pulsed laser Raman spectroscopy for the identification of diamonds. The pulsed laser could have a wavelength ranging from the visible to the infrared spectrum (Lamprecht *et al*, 2007).

Microwave sensors: The microwave range covers wavelengths from 1 to 300 mm. When electromagnetic energy is absorbed by a material, the friction caused by the movement of the molecules in the material lattice gives off heat. Materials that absorb microwave radiation are referred to as dielectrics (Kingman *et al*, 2000). The dielectric property of the material is used for classification and separation.

Microwave technology has been applied for moisture determination of materials (Cutmore *et al*, 2000; Pickles, 2005) and thermal assisted ore liberation (Amankwah *et al*, 2005; Kingman *et al*, 2004). Kelly and Rowson (1995) discussed the application of microwave radiation in extractive metallurgy where pre-oxidised illmenite ore was reduced. The reduction process was undertaken with a variable power (0 - 1500kW) 2.45 GHz microwave oven. A microwave dielectric probe has been utilised in coal and iron ore characterisation and measurement of moisture content (Cutmore *et al,* 2000; Cutmore *et al,* 1998). However for sorting purposes there is no report of microwave technology application in the literature.

Radiowave sensors: This range comprises waves of greater than a 300mm wavelength. Methods such as electron spin resonance and nuclear magnetic resonance spectroscopy make use of this spectral range (Skoog *et*

al, 1996). Radiowave technology has application in the fields of astronomy but to date no application for sorting in the mining industry is available in the literature.

Non electromagnetic spectrum based sensors and classification devices:

The electromagnetic spectrum based sensors can be used to measure most of the properties shown in Figure 2.5. However other automated sorter designs are available that utilise non electromagnetic spectrum based sensors. These include magnetic and conductivity separation devices.

In an electromagnet, an electric charge creates a magnetic field in the space surrounding it. The magnetic field exerts a force on the electric charge moving through the field, this force is referred to as magnetic flux density (Fuerstenau and Han, 2003). The magnetic field that surrounds a magnet is described quantitatively by the magnetic field strength (H). The magnetic induction (B) also referred to as the magnetic flux per unit area is related to the magnetic field strength by the relationship indicated in equation 2.4.

$$B = \mu H \tag{2.4}$$

Where

B = Magnetic induction, T

H = Magnetic field strength, A/m

μ = Magnetic permeability H/m

The magnetic force (F) exerted on a particle is stated in equation 2.5 indicating that for a higher applied magnetic field strength, the force on the particle would also be higher (Wells and Rowson, 1992).

$$F(N) = kVH\frac{dH}{dx} \tag{2.5}$$

Where

k = volume magnetic susceptibility

H = Magnetic field strength, A/m

V = Volume, Kg/m^3

— = Magnetic field gradient, T/m

There are three classes of magnetic materials; ferro-, para- and diamagnetic materials. Diamagnetic minerals are repelled along the lines of magnetic force to points of lesser magnetic field intensity. Paramagnetic minerals are attracted along the lines of magnetic force to points of greater magnetic field intensity. Ferromagnetic minerals retain magnetism after removal from the magnetic field. They can be considered as having 'stronger' paramagnetic properties than paramagnetic minerals (Kingman *et al*, 2000). The differences in magnetic susceptibility of minerals may be exploited for their separation.

The conductivity sensor measures electrical properties of samples as they are transported over an electrically charged drum or zone. As an object passes over a transmitter producing electrical pulses/flux, the object dampens the flux, yielding a difference between the transmitter and object fluxes. This difference is used to determine the object composition dimensions and can be applied for separation. Figure 2.13 shows an object attenuating the flow of conductivity as it crosses the coils that generate the electrical pulses.

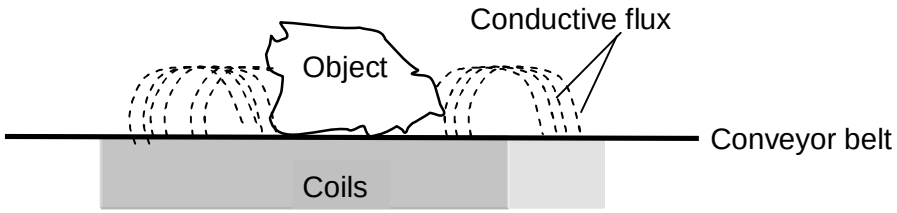

Figure 2.13: Operation of a conductivity sensor (after CommoDas, 2006)

Applications of magnetic and conductivity sorters include the S+S sorter utilised for de-shaling of coal, where the electric conductivity and magnetic properties between shale and coal were utilised for separation (De Jong *et al*, 2003). Coal lumps of 20 to 50mm size range were separated from shale. The sorter design involved feeding the coal and shale to the sensor via a conveyor belt travelling between 2 and 3ms^{-1}. Another sorter designed by International Sorting Systems Corporation was applied to sort copper from waste rock utilising electric conductivity (Sivamohan and Forssberg, 1991).

2.0.3 The separation system

Once particles have been identified the next step in the sorting process is separation. Manouchehri (2003) suggested the importance of a fast and accurate separation system to the increased applications of automated sorters in the mining industry. The separation system may consist of air or water jets valves, mechanical splitters or suction valves. Forsthoff (2000) discussed the utilization of water jets in separation of coarse dolomite. Water jets are not recommended if the material sorted is water soluble.

For coarser feed sizes (>250mm), mechanical flaps are used instead of compressed air for economic reasons (Arvidson, 2002). Eriez manufacturers have designed an automated sorter utilising mechanical flaps which is capable of about 8 deflections per second. This separation method is of advantage as there could potentially be savings on compressed air since no compressed air is required (ERIEZ, 2009). Suction valves have been used to suck away from a moving conveyor belt material requiring separation (Pascoe, 2000). The most widely used design however is

compressed air jets (Arvidson, 2002). Its high usage is linked to the speed and accuracy (precision) when compared to the other designs.

The identified or classified materials whose travel trajectory has been determined are passed through the separation system to accept or reject collector bins depending on the material properties. A short burst of compressed air deflects the materials off their travel trajectory into the appropriate collector bins. The bins are separated with a splitter which prevents the separated materials from mixing. The valve nozzles are usually in the flight trajectory of the materials with various configurations shown in Figure 2.14 (Bayram and Oner, 2006; CommoDas, 2006).

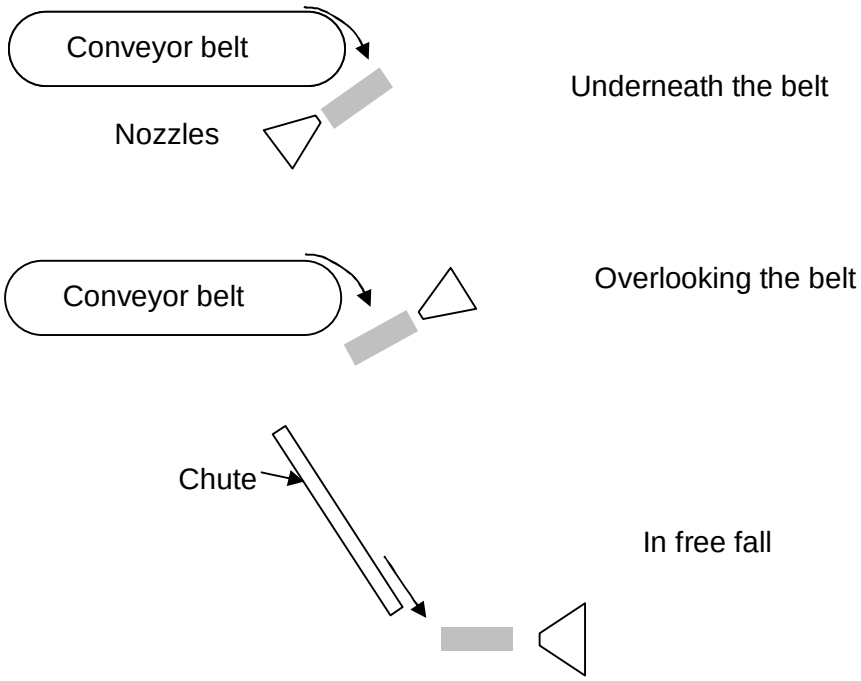

Figure 2.14: Various configurations of deflection nozzles

Although there are other air valve types, solenoid (electrically controlled) valves are utilised mainly because of their faster response times. The valve response times are controlled by electric current through a solenoid coil. When the valve is activated by the electric current, the solenoid converts the electrical energy into mechanical energy opening the valve orifices. The valve remains shut when not triggered. The opening (energising) and closing (de-energising) times vary with design but the most effective valve designs have a total opening and closing time ranging between 1 and 10ms (MAC, 2008; FESTO, 2009). Figure 2.15 shows a picture of a MAC valve.

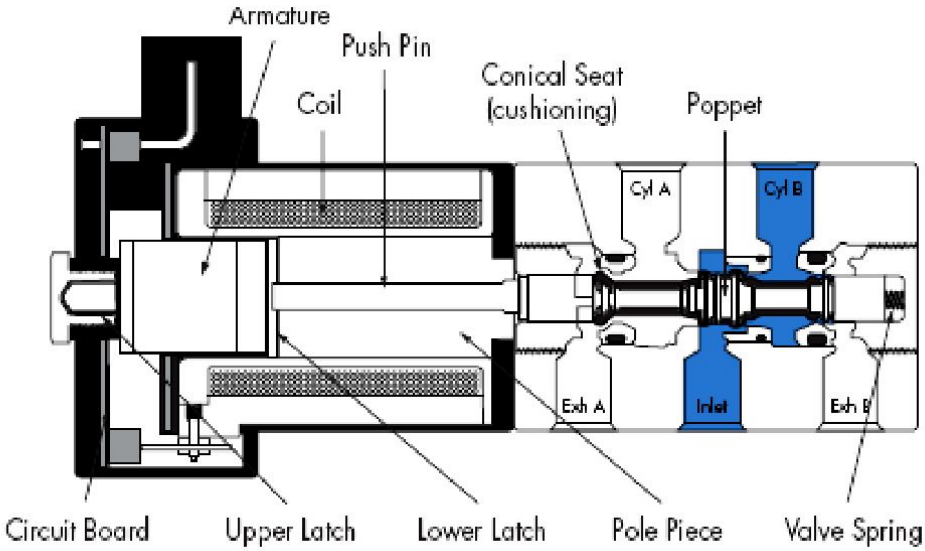

Figure 2.15: A diagram of a MAC latching solenoid valve (after MAC, 2008).

According to MAC (2008) "the poppet valve type uses a magnetic armature to seal off the poppet when power is disconnected from the solenoid. To shift the poppet in the opposite direction the polarity of the voltage is reversed reducing the attractive magnetic forces on the latch. The return spring in the valve is used to move the poppet to its other sealing position and the magnet is attracted to the upper latch. Reversing the polarity to the solenoid releases the latch from its previous position moving the poppet to the other shifted position."

2.1 DEVELOPMENTS OF SENSOR-BASED SORTERS IN THE MINING INDUSTRY

The application of automated sorters in the mining industry has developed from the single sensor, radiometric/x-ray based sorters to multiple sensor equipment. Automated sorter manufacturers included Gunson Sortex, Kelly and Hutter who were prominent until the 1980's. More recent manufacturers include the TiTech group, Applied Sorting, Eriez, Steinert, RTT, SINTEF, S&S Inspection in Europe and Satake operating from Japan (Kolacz and Chmelar, 2002; Zeuch, 2005; Graham, 2005; Habich, 2007). As sorters can be adapted to other industries, these suppliers/manufacturers produce sorters which are not limited to the mining industry applications.

A chronological list of sorter developments in the mining industry is shown in Table 2.1.

Table 2.1: Applications/developments of sorting machines in the Mining Industry

Model/ manufacturer name	Year of manufa-cture	Sensor(s)	Application(s)	Reference
Lapointe picker	1946	Radiometric	Uranium	Salter and Wyatt, 1991
NA	1952	Photometric Monochromatic	Coal	Salter and Wyatt, 1991
Ore Sorters/Kelly & Hutter (K+H) M6	1959	Photometric Coloured	Uranium	Salter and Wyatt, 1991
Gunson Sortex	1965§	Photometric coloured	Limestone	Sivamohan and Forssberg, 1991
(K+H) M13	1972	Photometric Coloured	Gold	Schapper 1977, Adorjan 1985
(K+H) M16	1975	Photometric Coloured and Laser scan	Magnesite, wolframite, phosphates, gold	Bibby 1982
(K+H) M17	1978	Photometric Coloured and Laser scan	Uranium	Bibby 1982
(K+H) M19	1980	Conductivity and magnetic	Copper sulphide ores	Salter and Wyatt, 1991
Outokumpu/Precon	1980	Gamma	Uranium	Salter and Wyatt, 1991
LKA International USA/Beryllometre	1988	Gamma activation	Emerald	Salter and Wyatt, 1991
NA	1988§	Microwave attenuation	Diamond bearing kimberlite ore	Sivamohan and Forssberg 1991
Applied sorting	2000	X-ray (fluorescence), radiometric and laser optics	Nickel, Diamonds	AU, 2008
X-tract	2004	X-ray transmission	Coal	Anon, 2006

*** NA = Not available, '§' approximated from publication**

After the World wars, automated sorters were occasionally utilised in the mining industry, to replace the traditional separation technique of hand sorting. The 'Kelly and Hutter' M-series sorting machines were prominent between the 1950's to the 1980's to sort ore such as gold and coal. These sorting machines were fitted with radiometric, photometric (optical) and x-ray sensors (Arvidson, 2002; Salter and Wyatt, 1991).

The use of sensor-based sorters declined between 1980 and 1990 (Arvidson, 2002; Salter and Wyatt, 1991). Salter and Wyatt suggested that mining operations found the use of the automated sorter expensive because of the sorters' capital and operating costs. Cutmore and Eberhardt (2002) noted that there was no major increase in the application of automated sorting machines between 1980 and 2000. They were however optimistic

that with the technological and innovative applications of computer technology at the time and image processing that there would once again be an increase in automated sorter utilisation in the mining industry. Kolacz and Chmelar (2002) suggested the amenability of the automated sorter to specific separation purposes is an advantage. There is also the link between sorter application and development of analytical techniques (Salter and Wyatt, 1991). Advances in analytical techniques are likely to feed into improved sensor development for automated sorting machines.

For the waste and recycling industry, the application of automated sensor-based sorting may be linked to disposal challenges. In the USA and Europe, there is the challenge of the limited availability of landfill sites for waste disposal and the growing environmental awareness of the problems associated with disposal of hazardous materials. Governments of these countries (USA, Europe) have addressed these concerns using legislation, increasing the cost of waste disposal in landfills and encouraging the reuse and recycling of products such as glass, plastics and construction and demolition wastes (Rayner, 2005; Barlow, 2001). End of life vehicle (ELV) and waste electrical and electronic equipment (WEEE) legislation have also led to increased product recycling or reuse (Dalmijn *et al,* 2004; Mesina *et al,* 2007; Rayner, 2005; Killmann and Pretz, 2006). These factors have led to the innovative design of automated sorting machines capable of sorting waste which cannot be separated economically using manual (hand) sorting.

The innovative design includes both new sensors, multispectral and multiple sensor configurations. Examples of multiple sensor configurations include optical sorting machines fitted with two or more cameras for 360° (triaxial) inspections of the feed material thereby enhancing identification (Arvidson, 2002). Multispectral configurations utilise cameras that can identify materials in more than one range of the electromagnetic spectrum for example the visible-infrared sensors, which make use of both the visible and near infrared range of the electromagnetic spectrum (Gomez *et al*, 2006).

Other industries that have applied automated sorting include agricultural (for fruits, seeds and grains processing) and the pharmaceutical industries.

2.2 APPLICATIONS OF SENSOR-BASED SORTERS

A review of the literature suggests that the mining, agricultural and waste/recycling industries were the greatest users of automated sensor-based sorting machines. In the following sections the potential benefits of automated sorting in the mining and waste/recycling industries are discussed.

2.2.1 Mining Industry

The mining industry employs the automated sorter for pre-concentration of sulphide ores, and ore associated with uranium (Gordon and Heuer, 2000). Alternatively automated sorters can be applied to produce a final product such as coal (De Jong *et al,* 2005), marble (Varela *et al,* 2006), feldspar (Harbeck, 2001), diamonds and gemstones (Salter and Wyatt, 1991). Savings to the overall mine operation costs may be possible with automated sorters (Manouchehri, 2006). The sorter is particularly amenable to operations where a small fraction of the materials (whether ore or waste) is due to be separated, especially at sizes larger than 5mm as this reduces cost (compressed air) and can improve efficiency (Manouchehri, 2006).
Some other benefits include:

- Reduction of the environmental impact of a mine through sorting of ore from gangue after primary crushing. This is an advantage as the production of coarse tailings reduces the rate of leaching undesirable metals (Arvidson, 2002).
- Higher recovery of ore by processing ore of marginal grade (Cutmore and Eberhardt, 2002).
- Reduced operating costs as the sensor-based sorter machine allows separation at coarser size fractions, potentially reducing comminution costs (Manouchehri, 2006).
- Increased production rate of minerals such as gemstones, when compared to hand sorting especially when between 5 to 10% of the material is ore requiring deflection. The use of sorters also eliminates other challenges such as theft by workers (Arvidson, 1988).
- Application of automated sorting technology in climatic regions where dry processing is of advantage (De Jong and Harbeck, 2005).

2.2.2 Waste and Recycling Industry

The applications of the automated sorter in the waste and recycling industry include:

- Separation of glass by colour (Zeiger, 2005).
- Automated sorters fitted with NIR and x-ray sensors, are used to sort plastics made up of Polyvinyl chloride (PVC) and PET; where the x-ray fluorescence of PVC is utilised in separation (Killmann and Pretz, 2006; Pascoe, 2000).
- Sorting of construction waste where metal is removed by x-ray sorting (Zieger, 2005; Dalmijn and De Jong, 2004; De Jong *et al*, 2004).
- Automated sorters fitted with dual energy x-ray sensors are utilised to sort stainless steel from waste, nonferrous scrap metal and end-of-life car parts (Dalmijn and De Jong, 2004; Mesina *et al*, 2007).
- Separation of metals from non-metals using conductivity based sensors.

2.3 COMPETING TECHNOLOGY WITH AUTOMATED SENSOR-BASED SORTING IN THE MINING INDUSTRY

In the mining industry the major use of automated sorting has been for pre-concentration of ores. The main competing technology is dense medium separation (DMS). This method utilises differences in the density of materials for separation and can process material in a similar size range to automated sensor-based sorting.

The principle of DMS is shown in Figure 2.16. The feed, of certain density is passed through a separating medium of known density. The feed particles of lower density relative to the separating medium floats while those of higher density sink. The 'sinks' and 'floats' are collected for further processing.

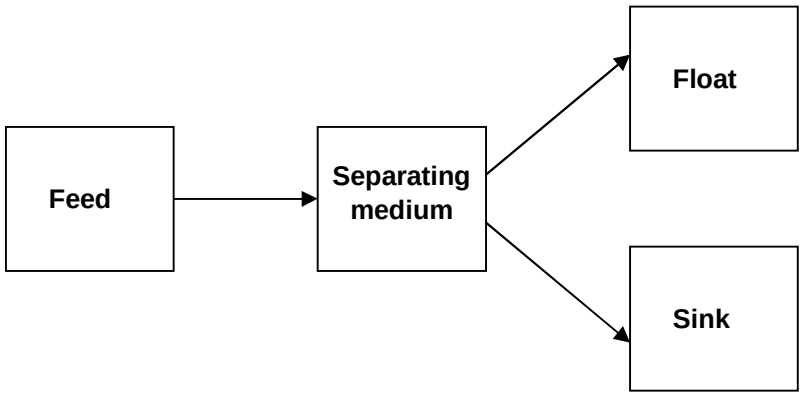

Figure 2.16: Principle of DMS sorting

The major advantage of DMS over the other mineral processing methods, such as jigging, is its efficiency of separation. Wills (2006) noted that this method can be utilised to separate different materials with a specific gravity difference of 100kgm^{-3} for particles over 2mm in diameter. Therefore materials with a very close density difference could be separated efficiently when compared to other methods. It is also an effective method for separation of coarse particle sizes, with separation efficiency reducing as particles get smaller due to slower settling velocities of the sinks. A summary of the differences between DMS and automated sorting is shown in Table 2.2, based on information from Wills (2006) and Arvidson (2002).

Table 2.2: Summary of differences between DMS and sensor-based sorting

Parameters	DMS	Sensor-based sorting
Size range	Approximately 0.5 to > 250mm	Approximately 2 to 250mm
Versatility	Underground design challenging	Has been operated underground
Ancillary equipments	Crushing and wet screening	Crushing and wet screening
Operating costs (main consumables)	Media – Magnetite/Ferrosilicon	Compressed air
Throughput	Not very dependent on particle size. Approximately 2 to > 250 Tonnes/hr	Dependent on particle size. Approximately 2 to >200 Tonnes/hr
Applications	Its major use is for separating high-ash coal from shale. However DMS is also use in pre-concentration of diamonds, ores of tin, tungsten, and sulphide metals. It has applications in plastic metal and glass separation (recycling waste sorting)	See section 2.2 for details
Location advantages	Processing in extremely cold climates becomes expensive where the water used has to be heated e.g. beneficiation of Pb/Zn in Greenland	Potentially a dry process so easier to operate in cold climates

2.4 CHALLENGES TO IMPROVING SENSOR-BASED SORTING EFFICIENCY

The challenges to improving senor-based sorting efficiency are mainly associated with the sorter identification and separation/deflection capability (Arvidson, 2002, King 1978). For sorters that measure surface properties such as colour or brightness identification may be limited when only a side of an object is scanned such as the case where a camera overlooks an object on a conveyor belt. This is an issue when the object is heterogeneous and may display more than one colour depending on which side faces up while passing through the identification point. Identification challenges could be overcome by the application of automated sorters with more than one camera to allow for triaxial (360°) identification. Surface-related identification issues are not a challenge for sorters fitted with sensors which measure internal properties such as x-ray sorters (Dalmijn and De Jong 2004; Arvidson, 2002).

Compressed air jets are the most widely used separation method. For feed presented either in free fall or travelling off a vibratory chute or conveyor belt, separation is most effective when the materials are presented to the sensors singly, without overlaps. This situation is not achieved for high throughput particle sorting as overlapping particles (composites) are considered to be a drawback (De Jong and Harbeck, 2005). This situation may occur when one particle touches another particle as they travel together at the identification zone. The probability of 'composite' occurrence increases with throughput.

De Jong and Harbeck (2005) studied the effect of overlaps, to understand the capacity limitations of particle sorting machines. They studied the theoretical area a particle would occupy, utilising this information to determine the probabilities of overlapping. Particles were randomly spread on a defined area 'A', the fraction of the area (A) free of particles, occupied by one particle; two particles and so on were calculated. Assuming that a dynamic image frame (frame captured in motion) is equal to a stationary image frame, the probable zone (A_p) where the particle is free from overlaps was determined.

Considering an area index 'I', I = 0 for a free area; I = 1 for area occupied by a single particle and I = 2 for area occupied by two particles. P(i) is the existence probability at the different area indexes. 'N' represents the number of particles in area A. Hence for N = 0, P(0) = 1. It follows that as N increases, P(i) decreases. This relationship is represented in equations 2.6 and 2.7.

$$\Delta P(0) = -\frac{A_p}{A} P(0) \tag{2.6}$$

$$\Delta P(i)_{i=1}^{\infty} = \frac{A_p}{A} P(i-1) - \frac{A_p}{A} P(i+1) \tag{2.7}$$

Figure 2.17 is a graphical representation of the belt area covered as number of particles increase. The authors also suggested that overlaps of particles greater than two were not significant as the particles would rearrange on the conveyor. A simpler and more precise method of determining overlaps is discussed in this thesis calculated using the image processing data obtained from the sensor-based sorter.

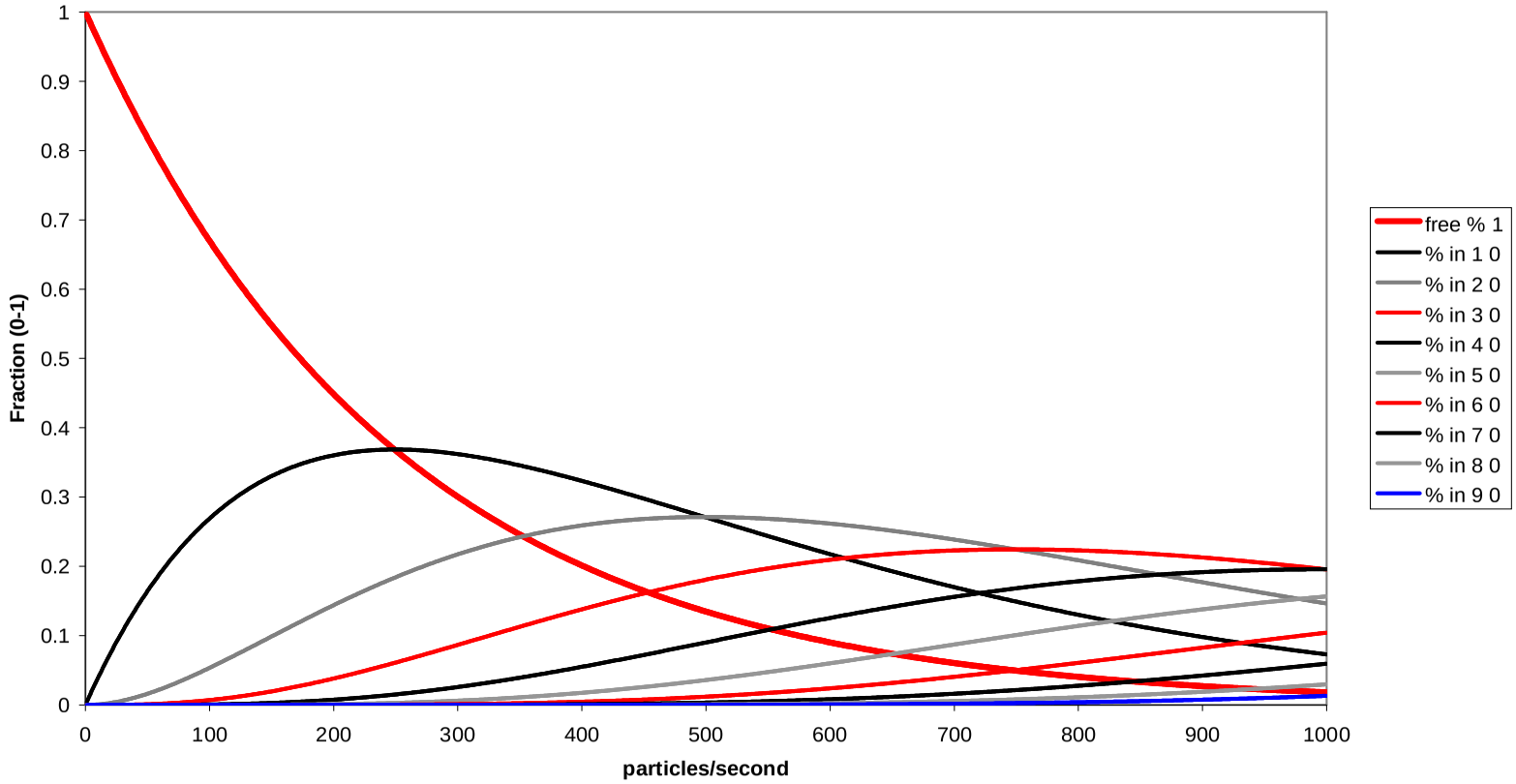

Figure 2.17: Existence probabilities of n-th particle overlap planes as a function of the particle rate; n is given in the table to the right (after De Jong *et al*, 2005).

Another separation challenge is the feed sizing. There has to be close sizing for effective separation. Traditionally the maximum to minimum size fed unto the sorter for effective separation is restricted to a 3:1 ratio with the possibility of a 5:1 ratio for ore that requires a lower separation precision (Zeiger, 2005; Arvidson, 2002). According to Manouchehri (2003) this ratio is influenced by the valve and pressure selection required. Arvidson suggests the maximum size of about 250mm for rock with density of 3000kgm^{-3}. Particle size also controls the throughput as shown in Figure 2.18.

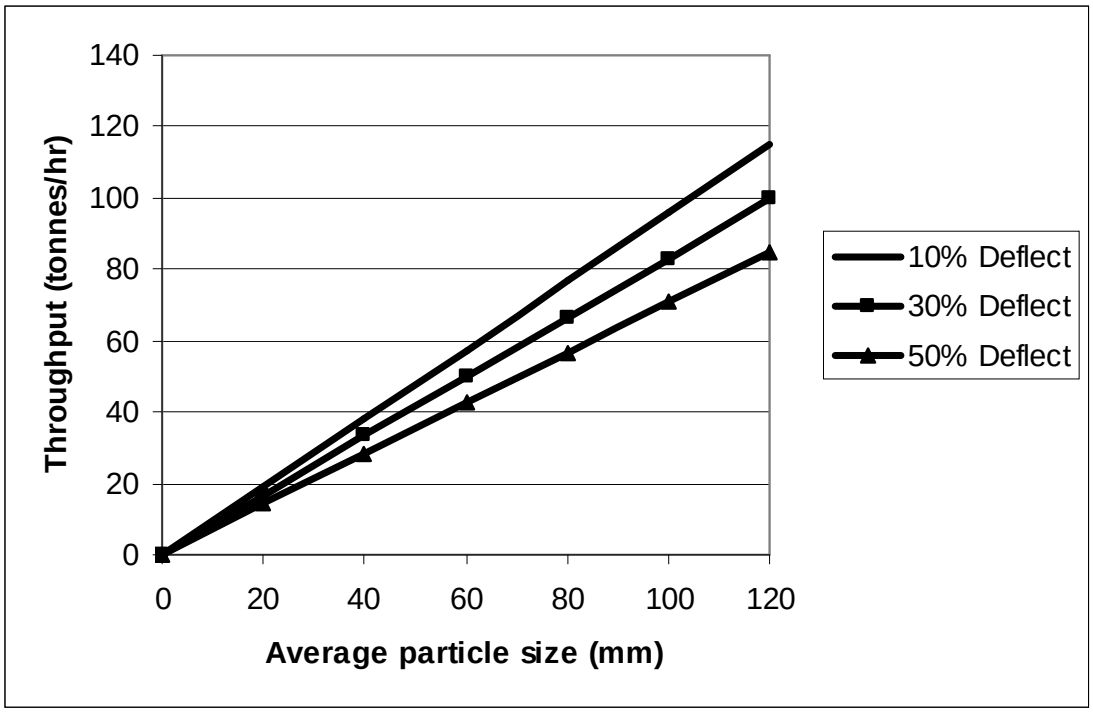

Figure 2.18: Sorter throughput as a function of particle size and % deflection (after Arvidson, 2002)

2.5 THE KING MODEL FOR SENSOR-BASED SORTING

Prior to the work by King (1978), no mathematical model for prediction of sorter performance had been developed. King (1978) produced a model for the calculation of sorter performance for the separation of gold reef material from waste. King noted that overcoming the problem of uncertainty in ore identification and deflection was crucial to improving automated sorter performance. These problems were accounted for with a probabilistic approach.

The model suggests the identification probabilities of ore lumps of a particular size (l) to be:

$I(o/o,l)$ = Mass fraction of ore lumps of size l that are identified as ore

$I(w/o,l)$ = Mass fraction of ore lumps of size l that are identified as waste

$I(o/w,l)$ = Mass fraction of waste lumps of size l that are identified as ore

$I(w/w,l)$ = Mass fraction of waste lumps of size l that are identified as waste

The identification probabilities could be considered as

$$I(o/o,l) + I(w/o,l) = 1 \tag{2.8}$$

and

$$I(o/w,l) + I(w/w,l) = 1 \tag{2.9}$$

Also deflection probabilities of ore lumps of a particular size (l) to be:

$D(o/o,l)$ = Mass fraction of lumps of size l that are identified as ore that are deflected to the ore bin

$D(w/o,l)$ = Mass fraction of lumps of size l that are identified as ore that are deflected to the waste bin

$D(o/w,l)$ = Mass fraction of lumps of size l that are identified as waste that are deflected to the ore bin

$D(w/w,l)$ = Mass fraction of lumps of size l that are identified as waste that are deflected to the waste bin

The deflection probabilities could also be considered as:

$$D(o/o,l)+D(w/o,l)=1 \tag{2.10}$$

and

$$D(o/w,l)+D(w/w,l)=1 \tag{2.11}$$

Where

$P(o/l)$ = Fraction of particles of size l that are ore

$P(w/l)$ = Fraction of particles of size l that are waste

and

$$P(o/l)+P(w/l)=1 \tag{2.12}$$

The model suggests the fraction of feed of size (l) that is sent to the ore stream E(l) can be given by the mathematical relation:

$$E(l)=D(o/o,l)I(o/o,l)P(o/l)+D(o/o,l)I(o/w,l)P(w/l)+D(o/w,l)I(w/o,l)P(o/l)$$
$$+D(o/w,l)I(w/w,l)P(w/l) \tag{2.13}$$

For the modified model, a single size is considered eliminating the size variable (l). The modified model is discussed further in Chapter 6.

2.6 MONTE CARLO ANALYSIS

A Monte Carlo analysis involves the application of random numbers and probability to solve problems relating to uncertain variables (VERTEX, 2009). It makes use of repeated random sampling. Monte Carlo analysis also involves simulating or mimicking test conditions and is sometimes referred to as Monte Carlo simulation. According to VERTEX (2009), Monte Carlo methods can be applied to define a domain of possible inputs, sum the results of individual computations and generate inputs randomly from a domain also performing a deterministic computation on them.

Morin and Ficarazzo (2006) described Monte Carlo analysis as a simulation method where the simulation results are based on a model where the input values are randomly selected from a representative statistical distribution describing the inputs. Monte Carlo analysis can be applied to several fields of discipline such as finance, science, engineering and mathematics. Monte Carlo analysis is usually undertaken with a computer that runs computational software such as Microsoft *EXCEL*©, ORIGINLAB© data analysis and graphing software and MATLAB© technical computing software.

Soldinger (2002) describes a Monte Carlo based model which makes it possible to predict the transport velocity of a crushed rock material bed along an ordinary screen with a circular stroke. Transport velocity can be predicted with respect to the inclination, stroke and frequency of the screen. When a particle leaves the screen surface the particle can slide along the screen surface. Monte Carlo simulation is used to estimate the influence of the other particles on transport velocity. Thus, random values are used to simulate the collisions between particles. Rock blasting fragmentation characteristics including size distribution, joint rock properties explosive type and drilling patterns were simulated using Monte Carlo analysis based on Kuz-Ram fragmentation model (Morin and Ficarazzo, 2006). The simulation was undertaken using Microsoft's Visual Basic software. The Kuz-Ram model is an empirical blast fragmentation model.

The application of Monte Carlo analysis in this research is discussed further in Chapter 5, sub-section 5.2.5.

2.7 EVALUATING SEPARATION EFFICIENCY

Dodbiba *et al* (2003) measured the Total efficiency (Tot_E) indicated in equation 2.14 of an air table.

$$Tot_E(\%) = \frac{\text{Weight of A}}{\text{Weight of A in feed}} X \frac{\text{Weight of Y}}{\text{Weight of Y in feed}} X 100 \tag{2.14}$$

Where A and Y were the constituents in the feed to be separated.
The equation utilises the mass balance between incoming and existing fractions.

Kolacz and Chmelar (2002) measure separation efficiency for a SINTEF sensor-based sorter to be

$$\text{Efficiency of separation}(\%) = 100 \times \frac{\text{Weight of rejected material}}{\text{Total weight of particles in feed to be rejected}} \tag{2.15}$$

In this thesis, a modified formula for the total efficiency, based on Equation 2.14, similar to that suggested by Schulz (1970) was utilised to enable analysis with the available data. This is referred to as the Separation efficiency (S.E.) defined in Equation 2.16:

$$S.E(\%) = 100 \frac{\text{Weight of A}}{\text{Weight of A in feed}} - 100 \frac{\text{Weight of misplaced Y in A}}{\text{Weight of Y in feed}} \tag{2.16}$$

Where A and Y are the constituents in the feed that are to be separated, with A being identified for deflection and Y identified as accept (no deflection).

This formula can be simplified to

$$S.E\ (\%) = R_A - R_C \tag{2.17}$$

Where

R_A = Recovery of feed A, (%)

R_C = Recovery of co-deflected feed Y, (%) {co-deflected into the A bin}

CHAPTER 3

EXPERIMENTAL EQUIPMENT

This Chapter describes the automated sensor-based sorter and the vibratory feeder to the automated sorter. The vibratory feeder was manufactured by Eriez Magnetics. The sensor-based sorter was manufactured by CommoDas GmbH, based in Wedel, Germany. CommoDas has since become part of the TiTech group (Norway), which is a subsidiary of the Tomra group, a leading manufacturer of recycling and industrial processing automated sensor-based sorting equipments (TOMRA, 2009).

3.0 THE VIBRATORY FEEDER

The Eriez Magnetics HI-VI vibratory feeder is fitted with a trapezoidal shaped metallic storage bin which discharges into a chute. The storage bin has a capacity of approximately 30kg of feed particles. Both the storage bin and chute are subjected to vibration. The electrically powered vibratory mechanism of the storage bin and chute are respectively fitted with two frequency controllers which could be regulated to give a desired throughput by adjusting the frequency of vibration. The frequency controllers' range could be set between one and ten. The feeder chute is 13cm in width and 65cm in length, while the depth of the chute ranges between 6cm at the tip of the chute and 9.5cm at the deeper end of the chute.

When conducting an automated sorting test, the storage bin was first fed with particles and the frequency controller switched on. Increasing the frequency of vibration (from 1 towards 10) increased the quantity of particles coming onto the conveyor belt via the chute. For test purposes the vibration control of the storage bin was left at the maximum (10) while the frequency of the chute controller was varied to produce the desired throughput. The maximum vibration eliminated blockage of the discharge gate with particles. Figure 3.1 shows a schematic diagram of the feeding system.

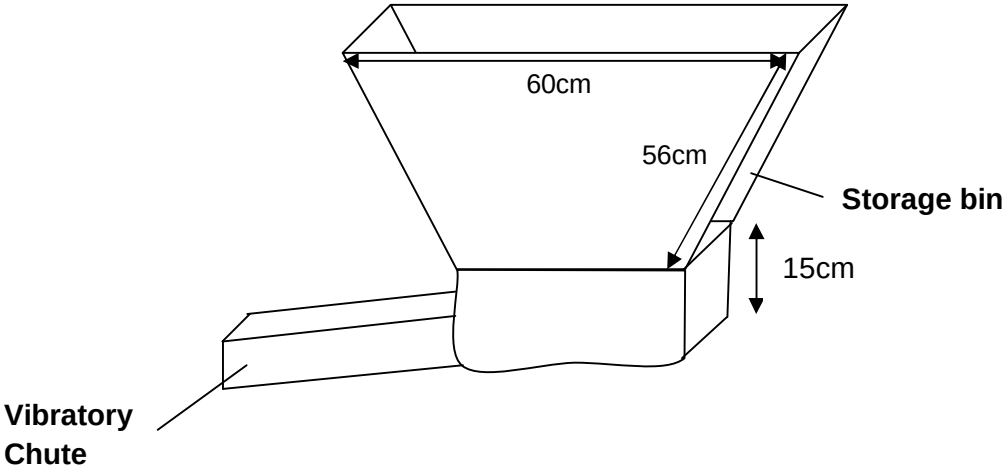

Figure 3.1: A diagram of the feeding system

The feeding system presents particles to the conveyor belt via the chute close to the speed of the conveyor belt. Figure 3.2 indicates the path travelled by a particle from the vibratory chute to the conveyor belt.

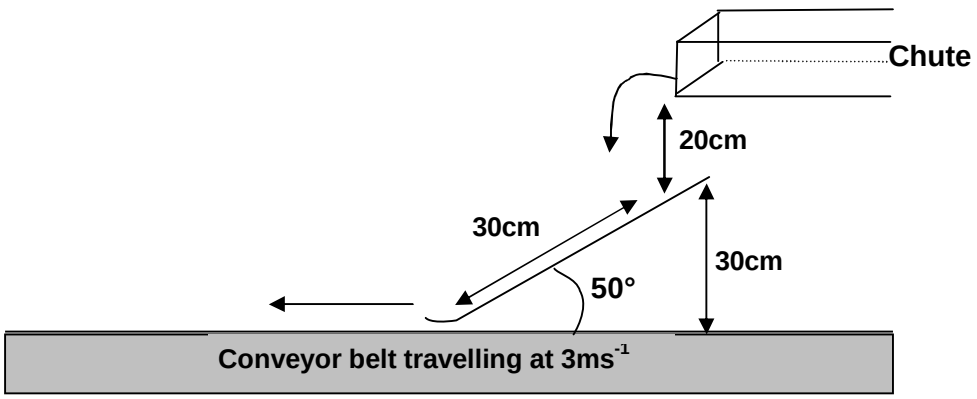

Figure 3.2: Path of a particle from the chute to the conveyor belt

The vibrating chute allows particles to accelerate before dropping in free fall approximately 20cm to the inclined iron plate fitted on the sorter. The plate is inclined at 50° to the horizontal conveyor belt. The plate is curved at the tip to allow the particles to impact the belt smoothly thereby reducing tumbling. The design is in agreement with recommendations by Stuart-Dick and Royal (1992) who discussed the designs and calculation of drop angle for particles onto a moving conveyor belt. Ideally the chute should introduce the particles onto the conveyor belt singly. Investigations however indicated that the materials may touch each other and form groups at high vibration frequency.

3.1 THE TITECH AUTOMATED SENSOR-BASED SORTER

The sensor-based sorter used to undertake all separation efficiency tests was a TiTech Combisense© sorter model BSM 063. This automated sorter was originally designed for the sorting of plastics, metals and glass as a part of a recycling system. The automated sorter is fitted with two sensors: a charge-coupled device (CCD) colour line scan camera and a conductivity (metal) sensor which was not used in this research. Descriptions with regards to the automated sorter which are described following are sub-divided into the operational sequences and the major components of the sorter.

3.1.1 The operational sequence

The operational sequence of the automated sorter can be divided into the following steps (see Figure 3.3):

The feed particles (1) are spread evenly on the conveyor belt (2), by means of a feeder chute. The conveyor belt accelerates the particles to $3ms^{-1}$ before the particle crosses the metal sensor (3). As the accelerated particle leaves the belt it is scanned by the colour line scan camera (4), and its properties such as colour, length and width in pixels including the particle position are recorded. Information obtained from the camera is sent to the control/feedback unit (5) and within a few milliseconds either allows the particle to pass to the 'accepts' collector bin (7) or activates one or more of the air ejector valves (6). This activation is based on the reject rule setting programmed by the operator. The reject rule setting controls valve activation either allowing one valve or several to be activated at a time to deflect the particles. The valves which are situated over the particle travel trajectory blow the particles into the 'rejects' collector bin (8). The bins are separated by an adjustable metal splitter. The control unit is also supported by a computer (9) running the operational software which is discussed later in this Chapter.

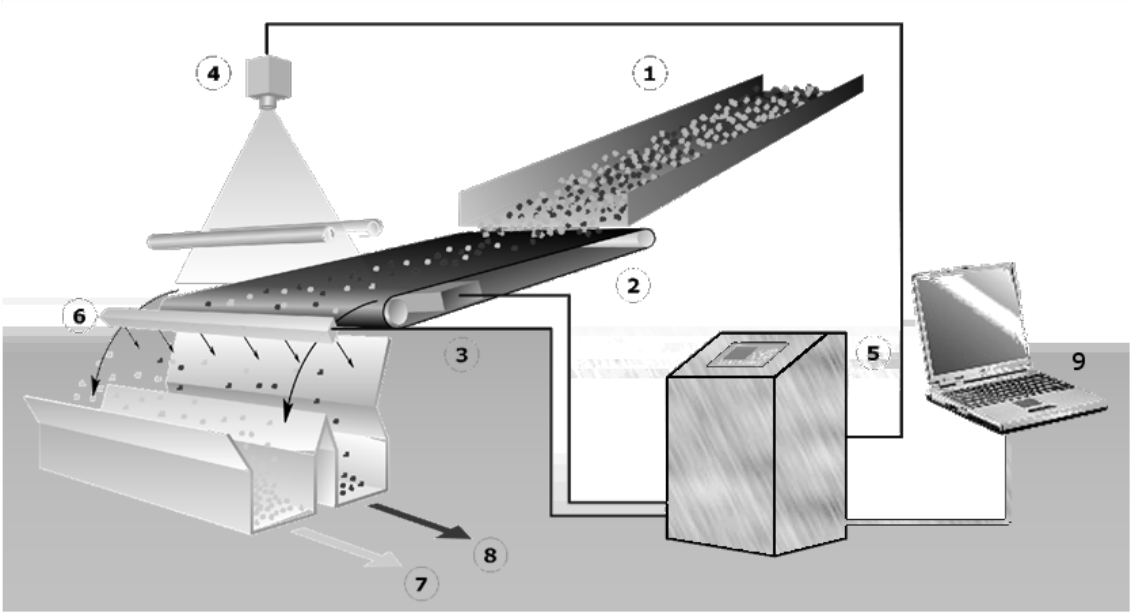

Figure 3.3: The TiTech automated sorter, indicating the operational sequence in numbers (after CommoDas 2006)

The TiTech automated sorter has major components which can be sub-divided into:

- The conveyor belt
- The sensors (including the illuminating components)
- The separation components and the control system

Each of these components is now discussed further.

3.1.2 The conveyor system

Feed particles are transported from the vibratory feeder to the sensors via the conveyor belt. The conveyor belt is designed to accelerate the particles to ensure stability and to help singularize the particles for easy identification, by the sensor(s).

The automated sorter is fitted with a 0.66 metre wide vulcanized rubber belt (with an effective width of 0.55 metres) with belt velocity configured to $3ms^{-1}$ for this research. The total length of the belt is 2m with an effective length of 1.8m as the inclined plate occupies some of the belt space. Plate 3.1 shows a picture of the automated sensor-based sorter indicating the camera, collector bins and conveyor belt. The compressed air blast manifold and lighting (including the background illuminating light) is concealed in the blue painted housing to the left of the picture.

Plate 3.1: A picture of the sensor-based sorter in the laboratory

3.1.3 The sensor

From the conveyor belt the particles are transported to the sensor(s) for identification and characterization. The line scan camera is fitted overlooking the belt. The camera scans particles approximately 12cm from the discharge point off the conveyor belt. Illumination is required to capture the images from the camera. The automated sorter is fitted with fluorescent lights which are placed underneath and overlooking the particle trajectory as indicated in Figure 3.4.

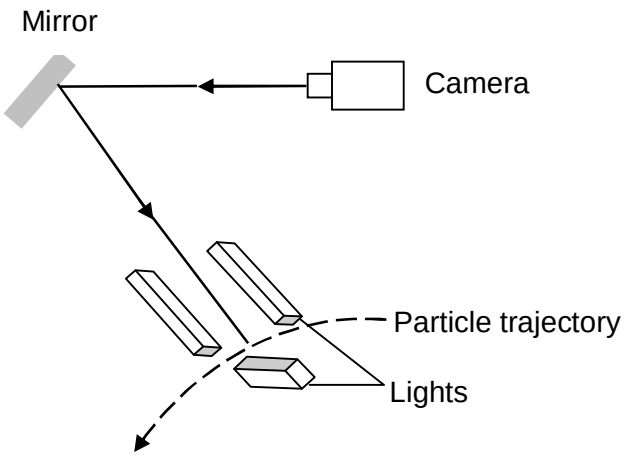

Figure 3.4: Positioning of lighting of the TiTech automated sorter

The camera measures reflected and transmitted light. For transmitted light the fluorescent light situated underneath the trajectory of the samples is utilised. This light also controls the background lighting. The other lights serve to produce reflected light from the particle.

The colour sensor: The camera fitted on the automated sorter is a Pri-colour TVI 2048R, 2048-bit line scan camera. The camera is fitted as indicated in Figure 3.5. The camera image is reflected using a mirror. The focal length of the camera is 50mm (CommoDas, 2006).

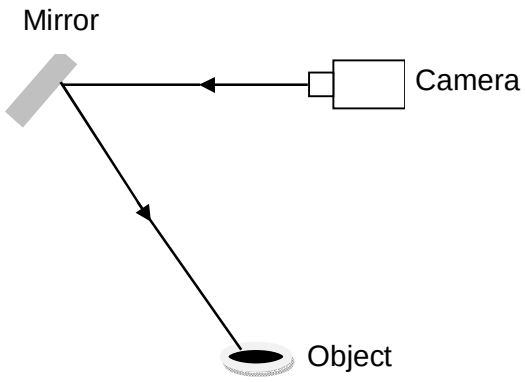

Figure 3.5: Positioning of the camera indicating the line of sight angle

An image is captured when the camera shutter opens capturing photons of light either reflected from or transmitted through the particles. The image is formed using three separate charge-coupled devices. Utilising a trichroic prismatic beam splitter, the colour image captured by the camera is split into Red-Green-Blue (RGB) components measured in picture elements (see

Figure 3.6). Each picture element is defined by combining data acquired from all three charge-coupled device's (Kwok *et al*, 2000).

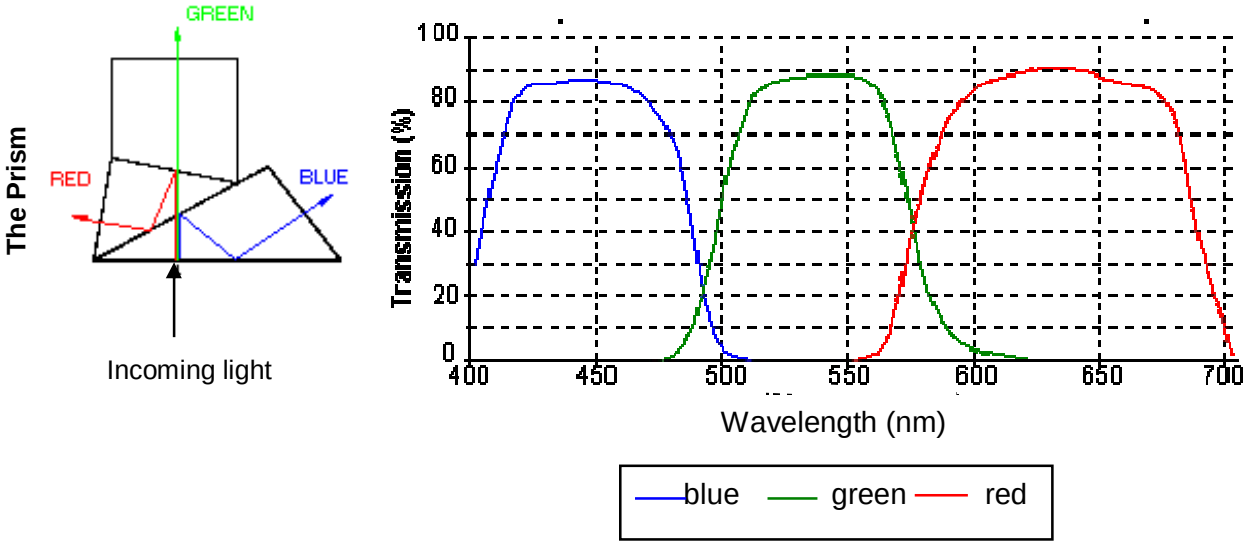

Figure 3.6: Trichroic prism splitting light into RGB components (after TVI, 2010)

The photons of light that strikes the charge-coupled device capacitors are converted to electron charges. As the shutter closes the electron charges are converted to a voltage which is measured by the electronic control installed on the automated sorter. This control interprets the information as picture elements (pixels). As the camera is stationary, to obtain a two-dimensional (2D) image the identified particle must travel perpendicular to the alignment of the line scan camera. The camera scans a different area of the particle as the particle travels (see Figure 3.7). Each image will be approximately 2048 pixels across with an equal length to the number of scans completed depending on the particle speed.

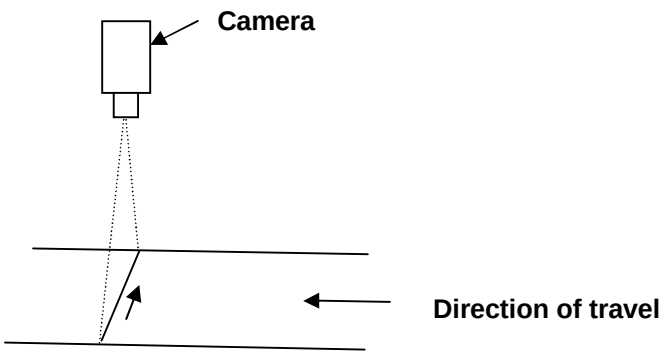

Figure 3.7: How a 2D image is obtained from a line scan camera

To obtain the dimensions of each pixel involves measuring the width of the area covered by the camera, the number of capacitors within each line, the time it takes for the camera to scan a line and the velocity of travel of the particle. The experimental scan time was set at 150μs, the velocity of the belt is $3ms^{-1}$ hence the length of each pixel is 0.45mm.

Distance = Velocity x Time

Distance = $3ms^{-1}$ x 150 x 10^{-6} m

Distance = 0.45mm

The width of each pixel is 0.27mm per pixel shown below

$$\text{Width of pixel} = \frac{\text{Distance to be covered}}{\text{number of pixels}}$$

$$\text{Width of pixel} = \frac{550mm}{2048\ \text{pixels}}$$

Width of pixel = 0.27mm/pixel

Owing to the camera positioning, the surface area of images captured is slightly larger as indicated in Figure 3.8. This is because the sides of the image are also captured increasing the surface area more than would be obtained if the image were captured from a perpendicular angle. Hence surface area measurements represent increased material pixel dimensions.

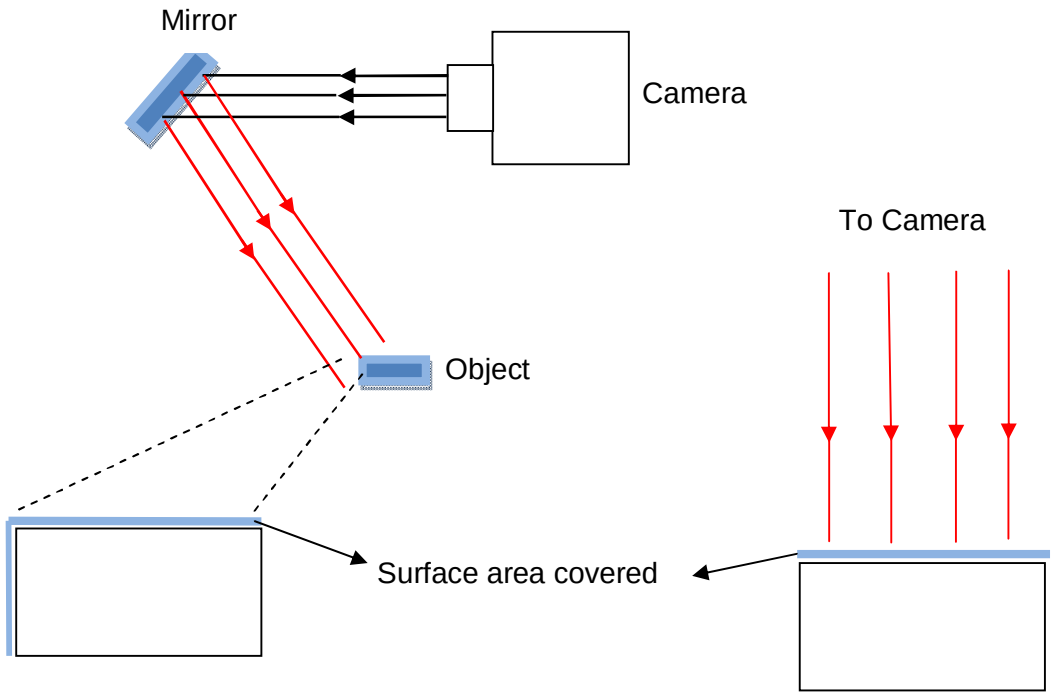

Figure 3.8: Surface area of material captured by the automated sorter camera varying with incident angle of light (after Fitzpatrick, 2008).

Colour space conversions: According to Jack (2005), a colour space is a mathematical representation of a set of colours which could be divided into three colour space scale/models: the RGB (Red-Green-Blue), YUV [Y (luma/luminance/brightness) UV (chroma) colour scale] and CYMK (Cyan-Yellow-Magenta-blacK). These colours may be acquired from a source such as a camera. In the operating software of the automated sorter utilising the pixel intensity of particle acquired by the camera, the colour class of the identified particle can be delineated. The automated sorter uses a YUV colour scale, which is a conversion of the Red-Green-Blue (RGB) colour model to the YUV scale.

The conversion can be computed using the relationships discussed next (Jack, 2005). The component video signals are generated by separating a luminance component and two chrominance components from RGB signals with the following formulae:

$Y = 0.299R + 0.587G + 0.114B$ Luminance component

$R-Y = R - (0.299R + 0.587G + 0.114B)$

$= 0.701R - 0.587G - 0.114B$ Chrominance component (Red)

G-Y = G - (0.299R + 0.587G + 0.114B)

= - 0.299R + 0.413G - 0.144 Chrominance component (Green)

B-Y = B - (0.299R + 0.587G + 0.114B)

= - 0.299R - 0.587G + 0.886B Chrominance component (Blue)

The contents of component video signal are these three signals (Y, R-Y and B-Y). To restore the RGB signal, the Y and two chrominance components is sufficient. The G-Y component contains the least chrominance in the three chrominance components hence while calculating the RGB conversions the G-Y term is omitted to minimize conversion error (Jack, 2005). When converting back to RGB signals from component signals the following formulae are applied:

R = Y + (R-Y)

G = Y - 0.51(R-Y) - 0.186(B-Y)

B = Y + (B-Y)

From RGB to YUV

Y = 0.299R + 0.587G + 0.114B

U = 0.492 (B-Y)

V = 0.877 (R-Y)

An advantage of the YUV scale is that the colour (UV) scale can be ignored and separation made based on the brightness (Y) components only. This ability according to Jack (2005) facilitates faster image processing leading to faster processing times enabling the processing of materials at higher throughputs than was previously possible.

3.1.4 The separation components

The particles were separated by means of 128 compressed air valves which are housed in a blast manifold. The manifold is fitted with nozzles with a diameter of 2.1mm and 2.4mm spacing between each nozzle (CommoDas, 2006). The air jets deflect identified particles as they come off the belt into the appropriate collector bins. The blast manifold is placed overlooking the

flight trajectory of the particle. Depending on the programmed operational conditions, the particles are either allowed to continue over the collector bin splitter into the 'accept' bin or are deflected using the air jets, as shown in Figure 3.9, into the 'reject' bin. The collector bins are separated using an adjustable metal plate/splitter which is tapered at the tip ensuring easy passage of particles.

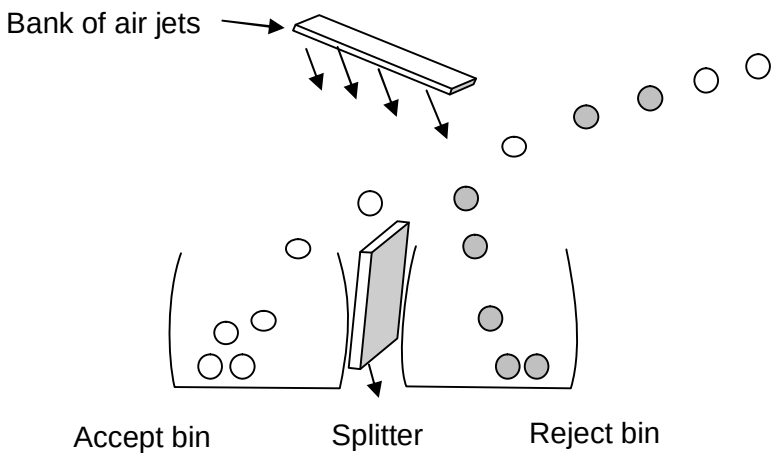

Figure 3.9: A diagram indicating the deflection of materials into the 'accept' bin by air jets.

The valves are MAC poppet solenoid valves with short stroke but high flow. The MAC valve indicating the poppets, valve spring and coil have been previously discussed (see Figure 2.15).

3.1.5 The control components

These components include the computer and control/feedback electronics which control the operation of the automated sorter. The control/feedback component installed is a MicroSort© PACT sorting control system (SCS), referred to as *PACT* in this thesis. This software enables the operator to control the sorter undertaking operations such as adjusting exposure and compressed air timing, valve testing and calibration. The software also allows image analysis of the particle which requires sorting to store particle characteristics and positions, as well as simulate separation models. A general overview of *PACT* is described in section 3.1.5.1 together with the set-up procedures applied for the tests.

3.1.5.1 An introduction to the *PACT* software

The *PACT* software installed is version 1.18.406. It can be installed on any computer operating system. "The computer connected via a fibre optic cable to the sorter operates this software utilising a Microsoft XP (home edition) operating system. *PACT* is designed to link signals from various camera types, conductivity sensors, infrared and X-ray sensors which may be installed. This software offers fast processing, recording and analysis of particle, particle dependent rejection, real image display and some tools for image analysis (CommoDas, 2006)." A schematic of the *PACT* controlling system concept is shown in Figure 3.10.

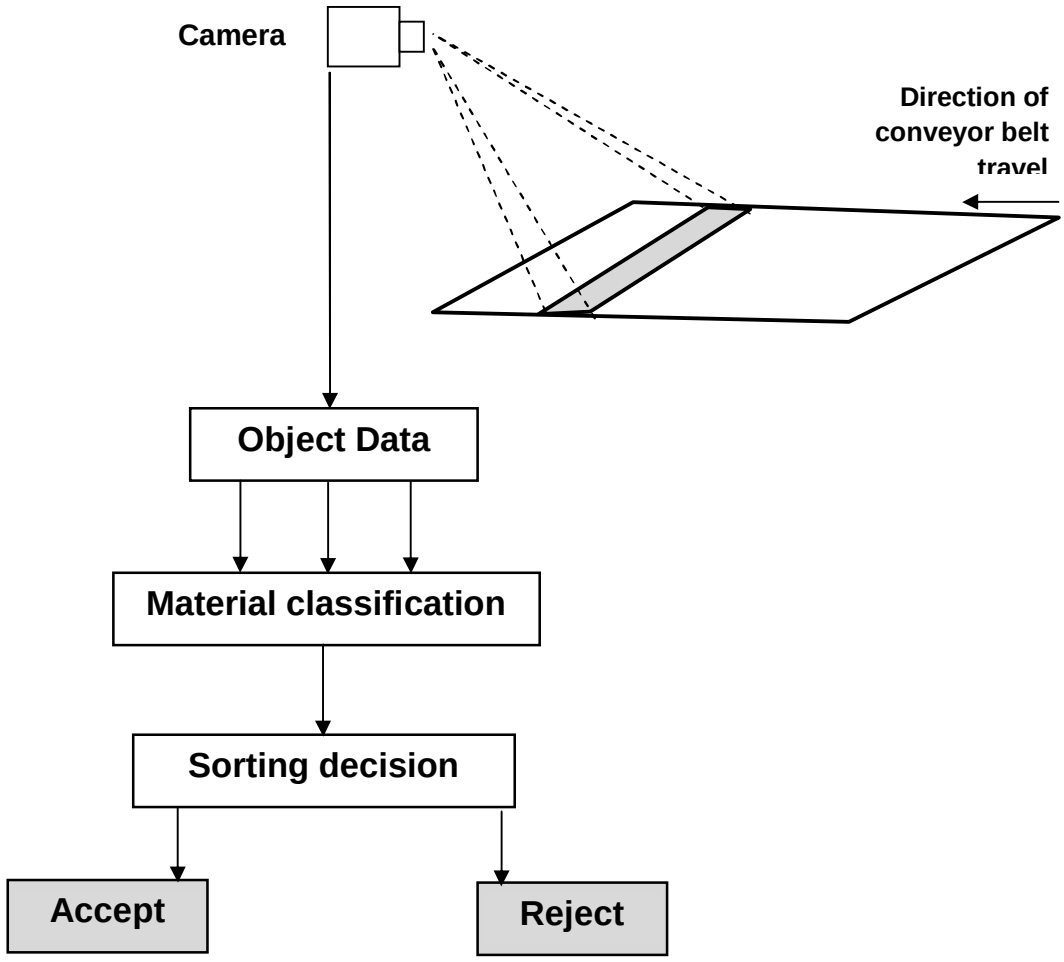

Figure 3.10: The *PACT* controlling system concept (after CommoDas, 2006)

The object recognition is based on colour characteristics hence individual particles must be distinguishable from the background. The background ideally should contrast the particles to aid identification. To acquire an image a portion of the belt is scanned (the shaded portion of the belt in

Figure 3.10). The acquired image undergoes image processing procedures such as image segmentation and filtering. Image segmentation involves determining the edges of the observed image utilising an algorithm that identifies sharp changes in colour or grey levels of neighbouring pixels using this information to segment the image (Singh and Rao, 2006; Mora et al, 1998). Image filtering involves smoothening edges of the image after segmentation utilising algorithms. During image filtering the pixel classes can be accentuated or attenuated (Gonzalez and Woods, 1992).

Consider for instance a line scan camera as the sensor, the image of the composite object (Figure 3.11A) is captured by the camera. To undertake the image analysis the object area is divided into a grid of picture elements (pixels). The object colour can be obtained utilising these pixel intensities (Figure 3.11B). The size of each pixel is dependent on the resolution of the camera. The dimensions of the object can be determined from the 'bounding box' (Figure 3.11C). The bounding box represents the area which pixel intensities indicate a difference between the image and the background colours. From this classification the object can be identified and separated (Suzaimah *et al*, 2008; CommoDas, 2006; Singh and Rao, 2006; Kattentidt *et al*, 2003). It should be noted that the bounding box doesn't conform to the image dimensions but forms a box around the object.

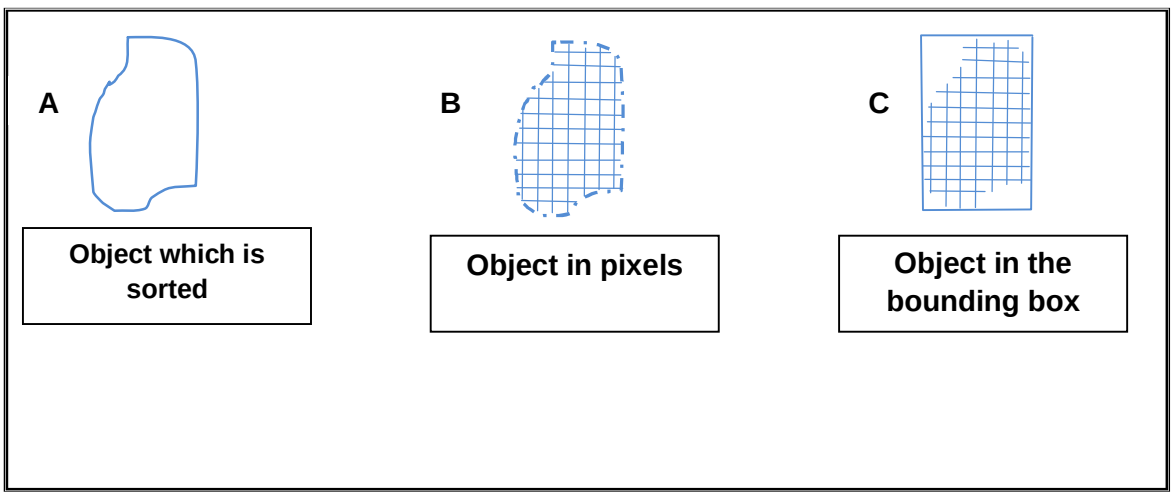

Figure 3.11: A simplistic image processing procedure

The characterized particle information is utilised to create the separation rules in the material classification section of the software. The sorting decision is made at the material level.

Detailed descriptions of the major tabs of the *PACT* software including how they are utilised are described in Appendix A. The TiTech automated sorter can produce 16 million pixel colours, the line scan camera scans up to 5000 lines per second. There is a rejection rate of over 2000 parts per second, with a particle size range of 2 to 30mm (De Jong and Harbeck, 2005; Anselmi and Harbeck, 2000; CommoDas, 2006).

3.1.5.2 The automated sorter starting procedures

Figure 3.12 shows a schematic for the setting up of the automated sorter for colour separation purposes and the section following describes each individual setting(s) for sorting purposes during the course of the investigations.

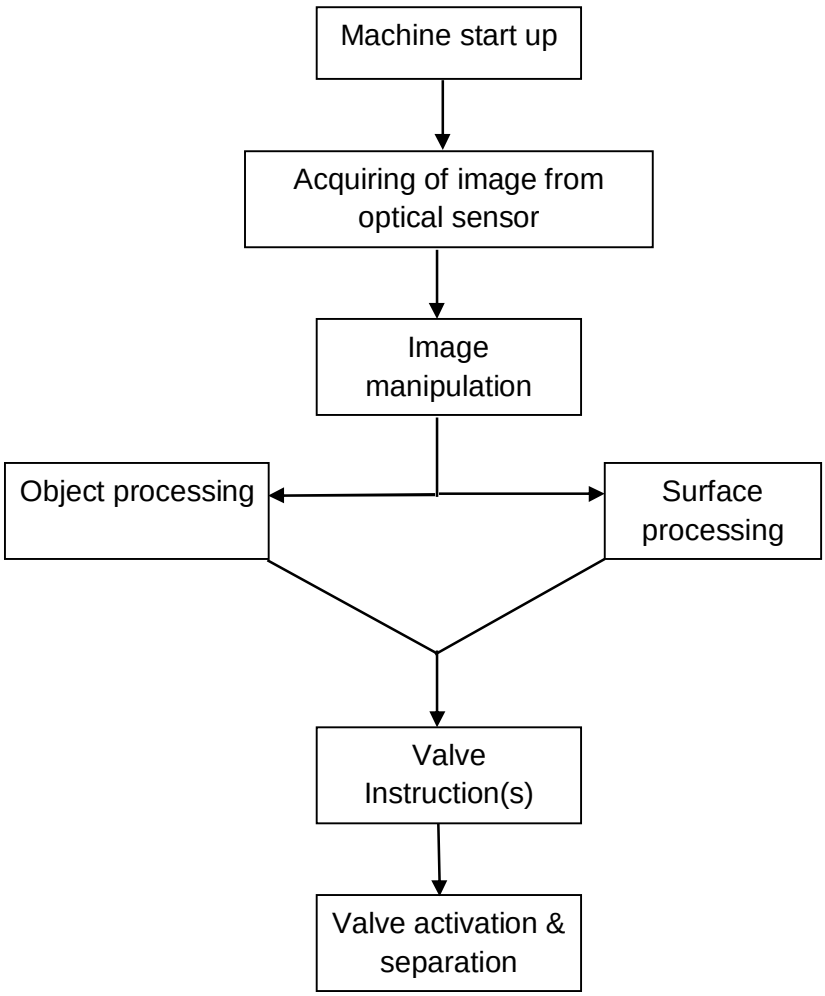

Figure 3.12: Flowchart of set up of the TiTech automated sorter for colour separation purposes

First the automated sorter electronics and the computer, which operates the *PACT* operating software are switched on. A sorting task profile is created in the *PACT* software and starting-up settings are initiated. The starting-up settings include calibration of the camera involving procedures such as undertaking a white and black calibration balance. This is essential for the YUV colour space calibration and classification. The white balance involves placing the provided white balance bar (an aluminium bar coated with white material) in the scanning line of the camera. The sorter is instructed using the computer to capture this image which is then utilised to calibrate the white balance. The black balance is set by the same means but using a black balance bar.

Other calibration settings include exposure time, line time and sensor code (See Appendix A). The *exposure time* in microseconds is the time for which

the shutter of the camera is opened when capturing objects. The effect of an increase or decrease (from 100µs ideal setting) is observed by the image of the object captured being brighter or darker respectively, when viewed using the analysis tool. The analysis tool is a viewing and analysing provision of the *PACT* software which will be discussed later in this section. The exposure time also can be set to enhance identification of objects judged by the detail of the object observed using the analysis tool. The *line time* is the time which the camera scans a line in microseconds. The shorter the line time the less time spent acquiring image information. A setting of 150µs was found through experimentation to be appropriate for the investigations. The *sensor code* controls the setting of the camera and *PACT* software to either acquire only Y (a black and white image) or UV images.

Another setting is the delay time (time between identification and air ejection) set in milliseconds. An incorrect delay time may lead to incorrect deflection of the feed particles by the air ejectors. The valve setting tab is utilised to choose the valve type and adjust the length of time the valves stay open. The effects of delay time and how the optimal delay time was determined for the samples utilised in the research are discussed in Chapter 4, sub-section 4.2.2.

After deciding these settings the sorter is ready to acquire images. Pictures of particles that require separation are first taken using the line scan camera. In the analysis tool of *PACT* the image colours are converted automatically by the machine from RGB to YUV colour classification. Figure 3.13 shows a picture of the analysis tool tab for blue painted and non-painted granite (see sub-section 4.2.1 for details). Image manipulation is undertaken using this tab.

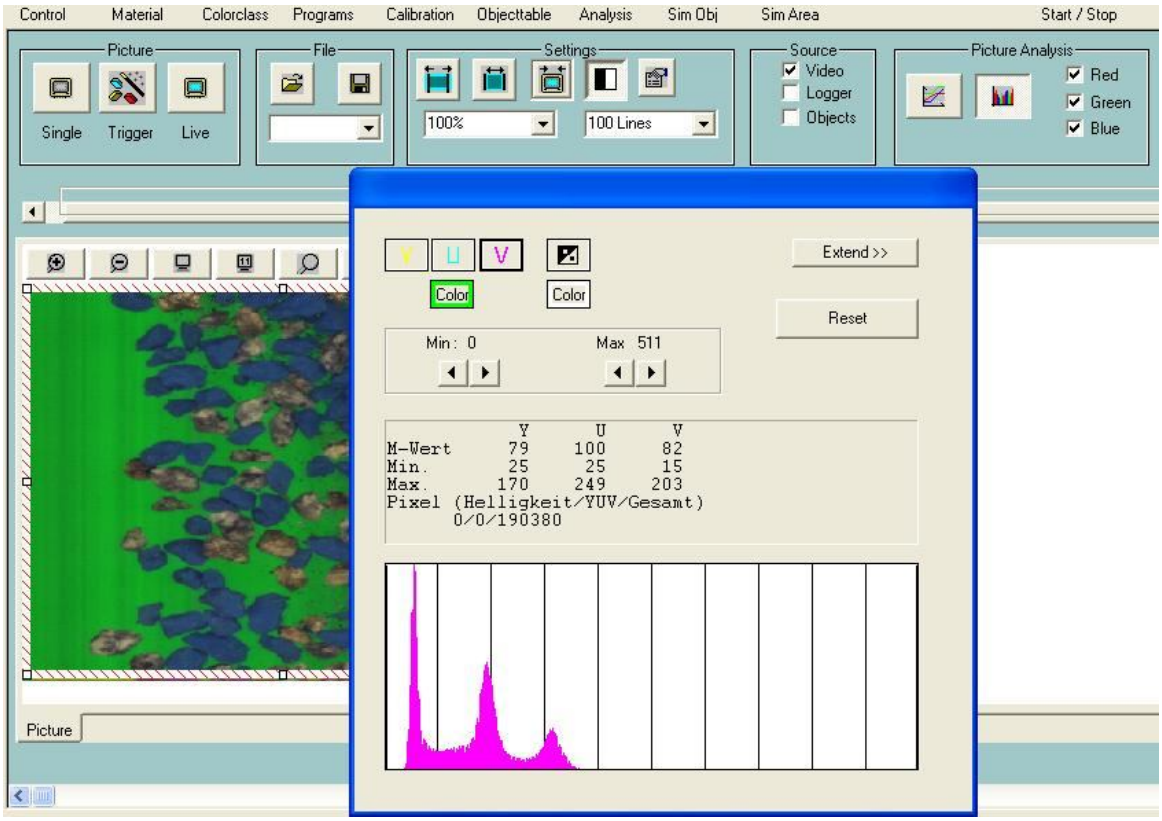

Figure 3.13: A typical YUV analysis tab with the background colour also included (the picture captured which is being analysed is to the left)

After the colours are adjusted to account for the background, the colour classification obtained for each of the materials is transferred to the 'colour class' section of the software (see Figure 3.14). The colour class section of the sorter is a colour model setting from which the material rules for separation are set. The process involves inputting the YUV values of the analysis tool tab in the colour class table. This process is repeated for each particle depending on how many material classes are required for identification of the sorted particle. In this research case there were four classes: the blue painted granite, non-painted granite, any other non classified material and the background.

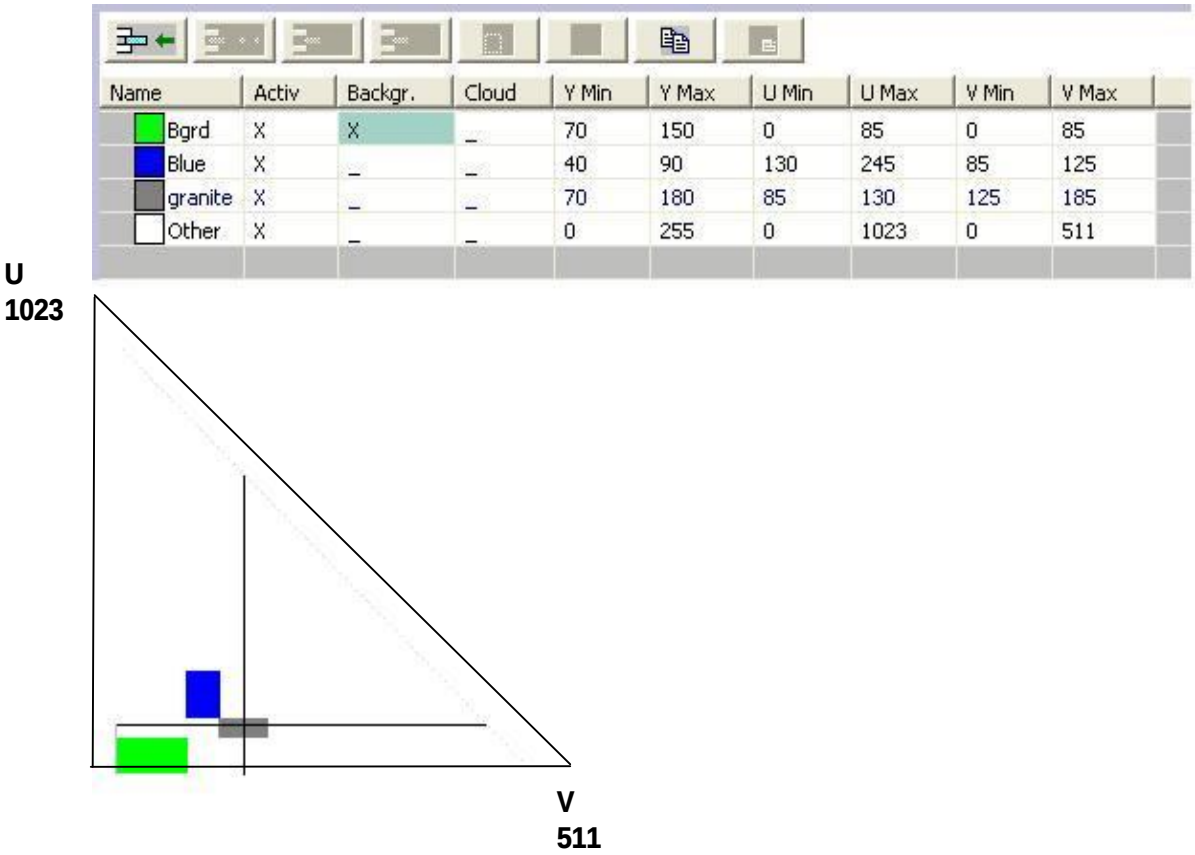

Figure 3.14: An example of colour class utilised to define material rules

After the colour class was determined, the material rules are set. This was after image manipulation other than colour classification had been undertaken on the object. Image manipulation includes image processing techniques such as filtering. 'Colour' material setting which utilises the colour obtained from the colour classes identified was used.

The next setting is the valve control or rejection rule. This is different from the valve control previously discussed. The reject rule setting determines how the air valves are activated, while the valve setting determines which of the valves would be used and for how long the valves are set to stay open. Two reject rules were used which were:

Rule one: Activation of all valves within the width of the bounding box with one valve centred around the middle of the bounding box.

Rule three: Activation of one valve at the horizontal position of the centre of gravity.

Rejection rule one and three (see Figures 3.15 and 3.16) are the most selective and compressed air efficient methods for separation at the sample sizes utilised for the tests. Experimental investigations indicate that reject

rule one produced better separation when compared to reject rule three. Also there was insufficient compressed air to deflect the larger sizes when utilising reject rule three. More detail of these investigations is discussed in Chapter four.

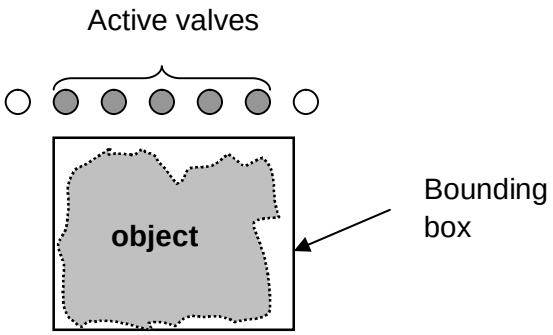

Figure 3.15: The valve configuration for a deflected particle based on "reject rule 1" (after CommoDas, 2006)

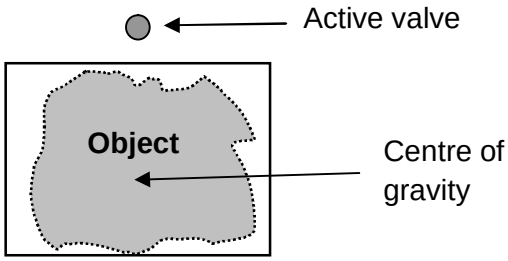

Figure 3.16: The valve configuration for a deflected particle based on "reject rule 3" (after CommoDas, 2006)

With the material rules set, the conveyor belt of the sorter can then be switched on and particles fed onto the belt for sorting. After separation particle information could also be acquired. How this was done and the method used to calculate properties from the extracted data are discussed in section 3.1.6.

3.1.6 Obtaining data from the automated sorter

Fitted on the sorter is an image processing analyser which is a material characterization and counter device which acquires image characteristics extracted using image processing. This information is obtained from the 'objecttable' tab of the *PACT* software. About 23 characteristics are

recorded for up to 2000 particles per test batch including the object number, the time the particle crosses the line of sight of the camera, particle dimensions (Xmin, Xmax, Ymin and Ymax), which are used to determine the width and length of the particle. Other characteristics include Xcentre of gravity, Ycentre of gravity, shape factor, surface area and colour classifications characterized by the operator. Particle components not required in the research include homogeneity, metal content and pixel filter. The complete list of components that can be recorded are given in Appendix A. Figure 3.17 shows a screen shot of some of the data that may be obtained. The shaded rows represent the particles that were deflected while the others were allowed to pass to the accept collector bin.

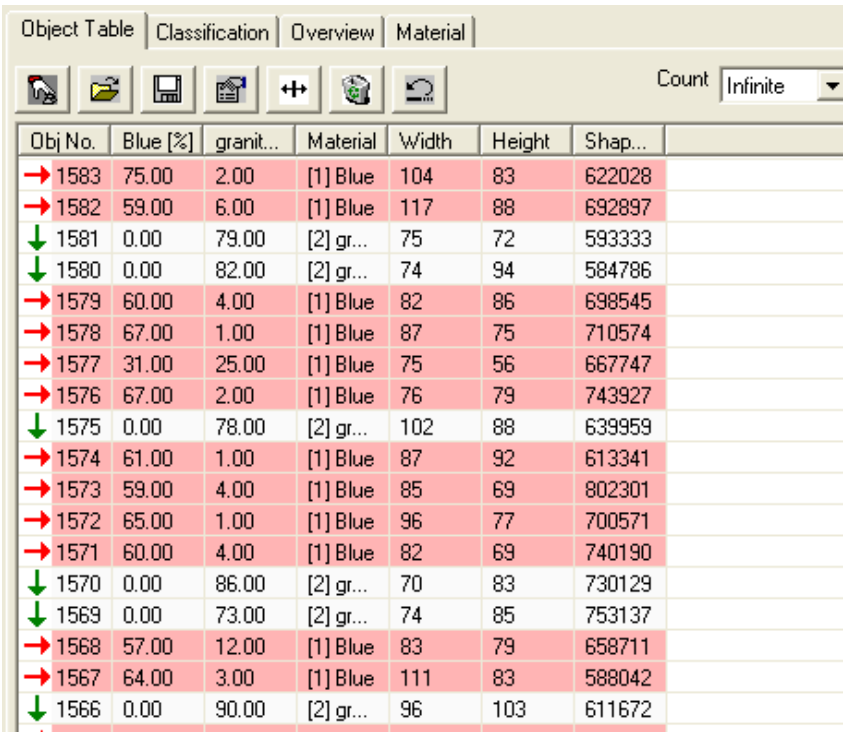

Obj No.	Blue [%]	granit...	Material	Width	Height	Shap...
1583	75.00	2.00	[1] Blue	104	83	622028
1582	59.00	6.00	[1] Blue	117	88	692897
1581	0.00	79.00	[2] gr...	75	72	593333
1580	0.00	82.00	[2] gr...	74	94	584786
1579	60.00	4.00	[1] Blue	82	86	698545
1578	67.00	1.00	[1] Blue	87	75	710574
1577	31.00	25.00	[1] Blue	75	56	667747
1576	67.00	2.00	[1] Blue	76	79	743927
1575	0.00	78.00	[2] gr...	102	88	639959
1574	61.00	1.00	[1] Blue	87	92	613341
1573	59.00	4.00	[1] Blue	85	69	802301
1572	65.00	1.00	[1] Blue	96	77	700571
1571	60.00	4.00	[1] Blue	82	69	740190
1570	0.00	86.00	[2] gr...	70	83	730129
1569	0.00	73.00	[2] gr...	74	85	753137
1568	57.00	12.00	[1] Blue	83	79	658711
1567	64.00	3.00	[1] Blue	111	83	588042
1566	0.00	90.00	[2] gr...	96	103	611672

Figure 3.17: A screen shot of selected data obtained from the image processing analyser of the *PACT* software

Where:

Obj No: is the object number (the automated sorter can capture up to 2000 particle positions at a time and records on a continuous basis, meaning the next set of recordings would start from object number 1584).

Blue (%): is the percentage of the particle characterised as blue computed by the automated sorter.

Granite (%): is the percentage of the particle characterised as grey granite computed by the automated sorter.
Material: is the material class characterised based on the material rules defined by the operator.
Width: is an estimate of the width of the particle in pixels based on the bounding box created around the particle.
Height: is an estimate of the length of the particle in pixels based on the bounding box created around the particle.
Shape factor: defines the geometry of the particle in pixels.

Using *Excel*© Microsoft software, data such as indicated in Figure 3.17 are converted to a similar spectrum of components. Figure 3.18 shows the calibrations of the conveyor belt.

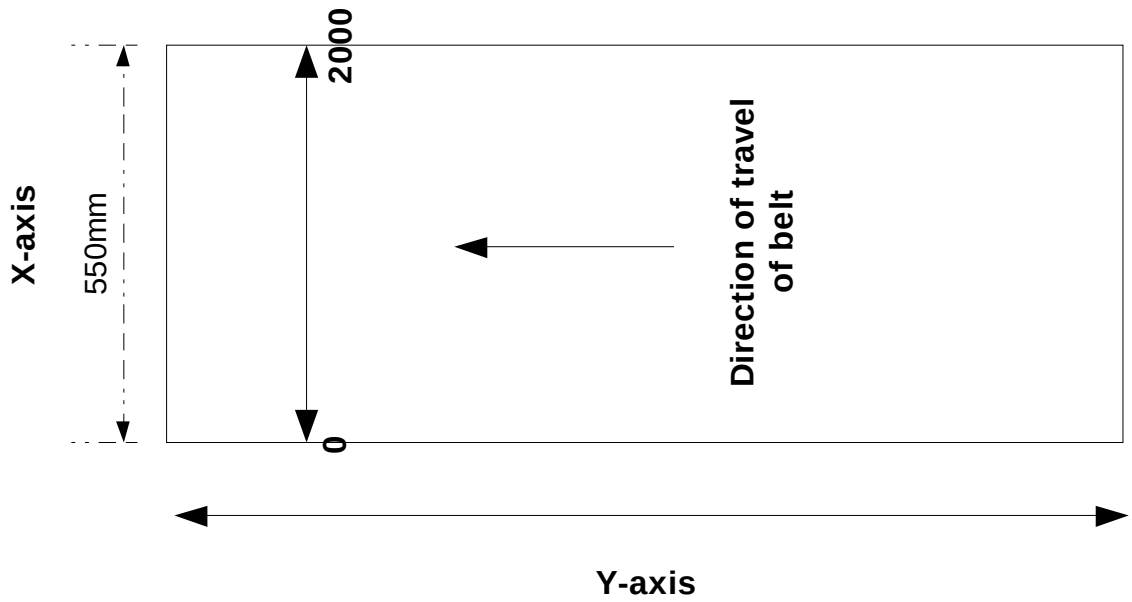

Figure 3.18: A diagram indicating the calibration of the automated sorter for the purposes of data capture

Excel© software was used because of its capability for undertaking calculations. Thus this data could then be applied to calculate any desired particle property such as particle area using the length and width data and the conversion of data from pixels to any other unit required.

CHAPTER 4

SAMPLE PREPARATION AND SEPARATION EFFICIENCY TEST PROCEDURES

To determine the efficiency of separation of the automated sorter, measurements were undertaken at various conditions which are discussed in this Chapter. The efficiency of separation of one sample fraction from another was calculated using the separation efficiency equation 2.16 discussed in Chapter 2. As separation efficiency depends on machine properties, feed presentation and material properties, investigations were undertaken along these lines.

Sample fractions were first prepared into various sizes and shapes then the sample density was determined. The automated sorter was set-up for colour sorting such that there was clear identification of the blue painted granite which was to be deflected. This colour was chosen to ensure easy identification by the automated sorter making it easier to investigate factors contributing to deflection inefficiencies. The effects of sample size, shape, fraction to be deflected and throughput on separation efficiency were investigated. The effects of machine properties including air pressure and valve deflection on separation efficiency were also investigated. To investigate the precision of the air valves, tests were undertaken to determine the zone of influence of a valve on particles.

Previous research indicated that particle size and the fraction to be deflected affect automated sorter separation. Of interest in this research were the other factors that may affect separation efficiency. Preliminary test observations indicated that the precision of the ejection system and the 'touching' of sample particles played an important part in determining separation efficiency.

The investigations sought to answer the following questions:

- Does particle shape affect performance, if so to what degree?
- Assuming clear identification what could cause reduced separation efficiency?
- To what degree does valve precision affect separation?

The results were utilised to develop a model that could be applied to predict automated sorter performance. To ensure repeatability, each separation efficiency test was repeated four times. This Chapter is subdivided into three sub-sections: sample preparation, machine preparation and efficiency test procedures.

4.0 SAMPLE PREPARATION

Approximately one tonne of both -20+10 and -10+2mm sized aggregates were collected from the Carnsew aggregate quarry at Penryn, Cornwall, United Kingdom. Granite was chosen because of its resistance to breakage and availability. The samples were then washed and screened into -20+15, -15+10 and -10+6mm fractions with 20, 15, 10 and 6mm sieves using British aggregates sizing standards (BS 1997). The screening was undertaken wet (cleaning the samples at the same time) using a Russell model 17300 vibrating sieve shaker.

After sizing, the -20+15 and -15+10mm fractions were separated with flaky sieves into flaky and cubical shaped products. The -10+6mm size was not classified into shape fractions because shape classification tests revealed the particles to be predominantly cubical. A flaky sieve has elongated openings between each separation aperture which allow only elongated (flaky) materials through it. Plate 4.1 shows a picture of a flaky sieve.

Plate 4.1: A picture of a flaky sieve

The sieve used for the -20+15mm sized particles had elongated bars of 60mm length with 12mm width between the bars, while the sieve used for the -15+10mm sized particles had elongated bars of 60mm length and 8mm width between the bars. According to Pike (1990) a particle is

considered to be flaky if the thickness (width) of the particle is less than 60% of the mean sieve size. Therefore for a -15+10mm size,

$$\text{Mean size} = \frac{15+10}{2} = 12.5\text{mm}$$

Flaky thickness = 0.6 x 12.5 = 7.5mm. This approximates to 8mm.

One of the objectives of this research was to investigate the effect of shape on separation efficiency of the automated sorter. To this end, the prepared samples were classified into various aggregate shape fractions utilising the Lees (1964) classification method. Other methods such as the use of digital image processing to measure aggregate size and shape have been proposed (Fernlund, 2005; Mora *et al*, 1998). The Lees method was preferred due to availability of equipment to measure aggregate dimensions.

Lees 1964 classification: Figure 4.1 shows the Lees calibration chart for classification. The 'cuboidal' portion of the chart is referred to as cubical in this research.

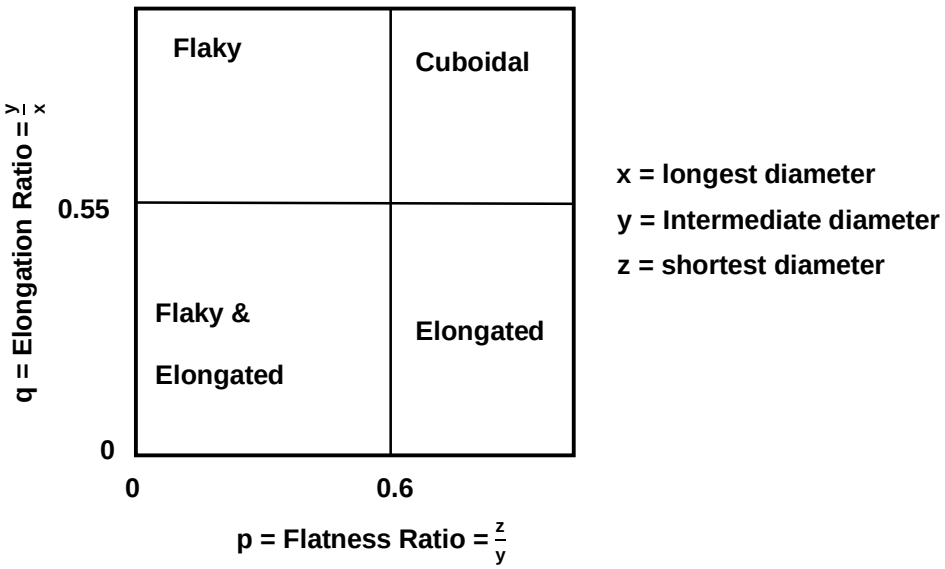

Figure 4.1: Lees (1964) classification chart of aggregates (after Smith and Collis, 1993)

Methodology: One hundred particles of each size fraction were collected and the longest diameter (x), intermediate diameter (y) and shortest diameter (z) were measured using a Mitutoyo vernier calliper. These diameters were then used to calculate the elongation and flatness ratios and the results were plotted on the Lees chart. Figures 4.2 and 4.3 indicate the classification for flaky and cubical shaped -15+10 and -20+15mm sample fractions respectively.

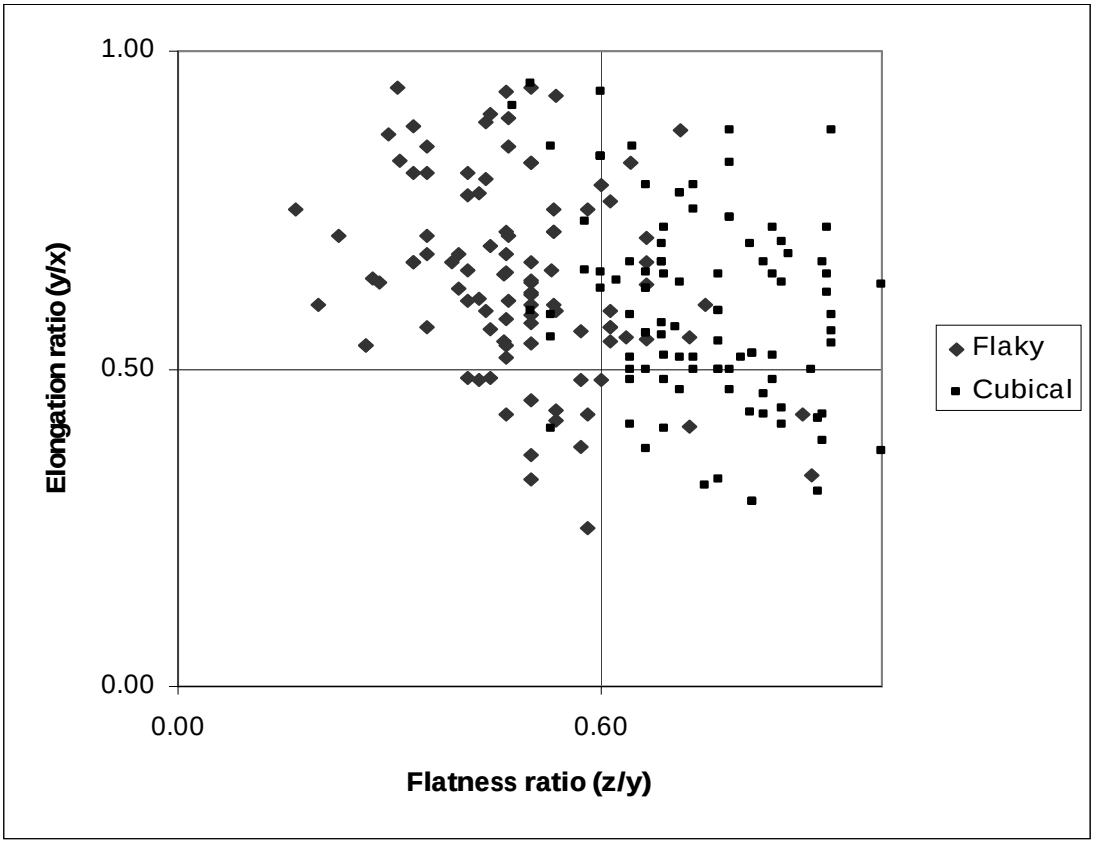

Figure 4.2: -15+10mm fraction, calibrated using the British standard classification

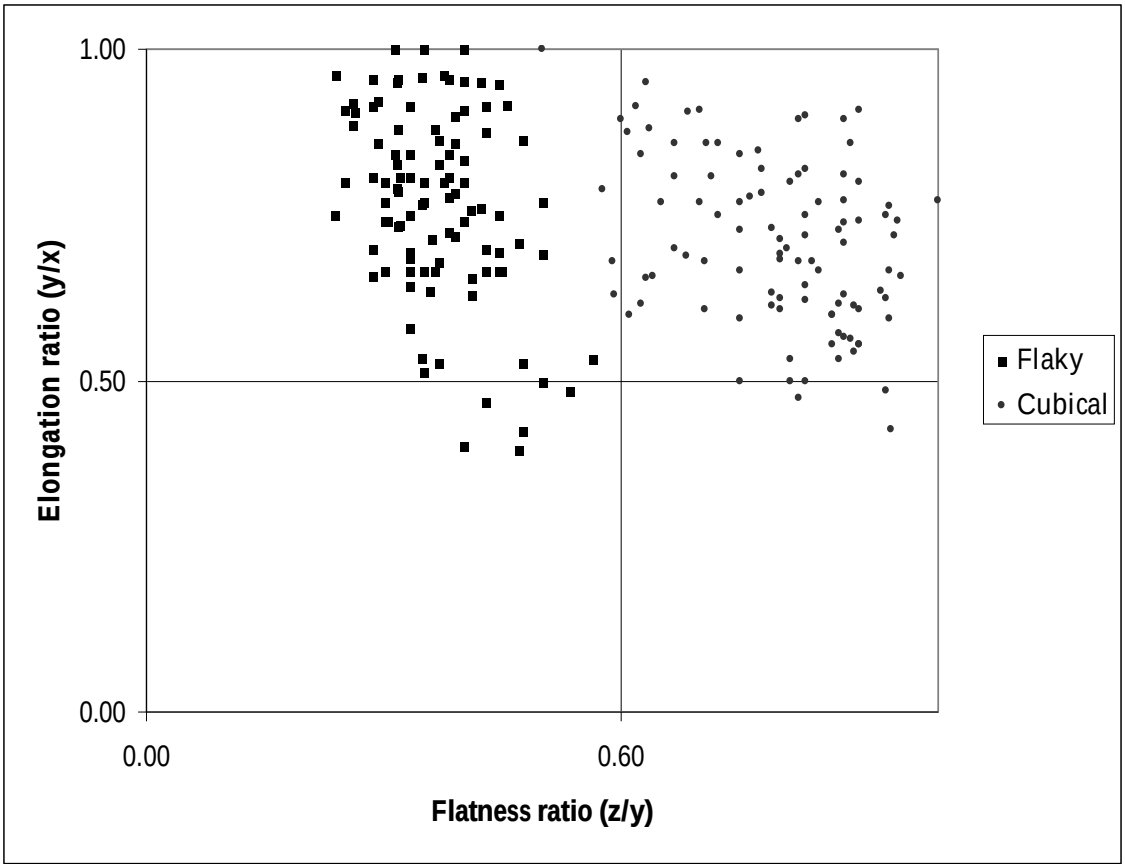

Figure 4.3: -20+15mm fraction, calibrated using the British standard classification

Figure 4.2 and 4.3 indicate that the flaky sieves have removed a 'flaky' product although the cubical shaped fraction still contained a proportion of 'flaky' particles. Some of the samples are also classified as elongated and flaky-elongated. The cubical shaped particles for the -20+15mm fraction had a flatness ratio (z/y) greater than 0.45 and an elongation ratio (y/x) ranging between 0.43 and 1. The flaky shaped -20+15mm fraction had a flatness ratio greater than 0.2 and an elongation ratio ranging between 0.4 and 1. For the cubical shaped -15+10mm fraction, the flatness ratio was greater than 0.45; and the elongation ratio ranging between 0.29 and 1. The flaky shaped -15+10mm fraction had flatness ratio greater than 0.15; and an elongation ratio ranging between 0.3 and 1. The complete data for all the classes can be found in Appendix B.

Preparation of coloured granites: The samples were first split into two groups using cone and split quartering. Cone and split quartering involves dividing a batch of samples. First the samples are spread on a surface in

the form of a cone. The batch 'cone' is then split into 4 quarters and samples taken from each quarter to form the groups required.

In this research two groups were obtained from the splitting. One half was then painted to achieve a separate colour for test purposes. The samples were painted with blue coloured proprietary water based emulsion paint. The reason for the choice of blue colour was to ensure clear identification explained further in sub-section 4.2.1.

Methodology: Approximately ten kilograms of the split sample groups was manually tumbled in a bucket of paint until all the surfaces were coated. The samples were then air dried for two days. This process was repeated once to ensure good coating before use. Any particles that lost a significant part of the coating during tests were removed.

Sample density determination: A Micrometrics AccuPyc 1330 helium pycnometer was used for density determination. Seventy five granite particles selected at random from each size and shape fraction were washed then dried in an oven overnight at 80°C. The dried samples were then cooled in a dessicator. After cooling, the weight of the samples was determined using a Sartorius weighing scale accurate to 0.01 grams.

To determine the density, the gas chamber of the pycnometer was first calibrated. Calibration involved inserting the calibration ball provided into the measuring cup and undertaking a calibration test. After calibration of the measuring cup, the samples of known weight were added and the density of the samples was determined. The average density over three tests of the granite samples determined was 2650kgm^{-3}.

4.1 MACHINE PREPARATION

To prepare the automated sorter for sorting purposes a general maintenance check of the compressed air valves, belt surface and belt speed were undertaken. The deflection system is essential for efficient operation of the sorter hence it was necessary to test the functionality of the valves especially as the error detectors of the automated sorter can detect other defects when the sorter is in operation but can't detect this defect. The air valve defects therefore had to be tested manually. A visual inspection of the conveyor belt was undertaken to check wear and tear. The belt speed was also determined with a tachometer. The test for background colour made use of the YUV colour space model where the least overlapping colour with the other particle colours was identified.

4.1.1 Valve tests

Installed in the *PACT* software is a material valve test trigger programme which was used in these tests. The procedure involved turning on the automated sorter and testing each of the one hundred and twenty-eight valves by releasing short bursts of air (in milliseconds) through the various valves. A faulty valve would not release air. These tests were repeated three times in the course of the research, six months apart. A faulty valve was discovered and changed prior to the start of the investigations.

4.1.2 Belt speed

A Smiths Industrial tachometer was utilised to measure the belt speed when in operation. The tachometer has a circular ring used to measure speeds in revolutions per minute. The speed of the belt was measured by placing the tachometer's circular ring on the belt and measuring the belt speed by the number of revolutions per minute the belt causes the tachometer ring to rotate. An average of three readings produced a belt speed of $3.02 ms^{-1}$.

4.1.3 Background colour determination

The automated sorter scans particles as they come off the conveyor belt with a fluorescent light illuminating underneath the particles. This light creates a background which is utilised for sample identification. The background colour affects material colour identification as it either enhances or swarms light reflection intensities. The aim of the test was to create a

background colour class in the YUV colour space which did not overlap with granite (painted and unpainted).

Methodology: A study of the YUV colour space indicates that the green colour does not overlap with the greyish (whitish) or reddish colour of granite. The fluorescent light casing underneath the line of sight of the camera was covered with a green coloured plastic strip to produce the desired background colour. This background colour was confirmed by analysing with the *PACT* analysis tool fitted on the automated sorter.

Preliminary tests showed no overlap between the background and granite samples in the U and V (which represent the chroma) portion of the YUV colour scale (more discussed in sub-section 4.2). With these differences the green coloured background was taken to be ideal for separation.

4.2 TEST PROCEDURES

Test procedures discussed in this section include colour classification tests aimed at determining the ideal paint colour that the test samples are to be painted. This paint colour should not overlap with the background colour. This is to ensure that the probability of identifying the painted particle is approximately 1. The optimal conditions required for operation of the automated sorter were investigated. Separation efficiency was afterwards investigated at these optimal conditions. The results of separation efficiency tests indicated >99% recovery of blue particles but also observed was a lowering of separation efficiency at higher throughputs due to misplaced particles thought to be as a result of particle 'touching'. Particle proximity tests were undertaken to investigate the effects of particles occurring in close proximity studying these effects on separation efficiency of the automated sorter. Tests were also undertaken to investigate the valve precision.

4.2.1 Colour classification tests

Tests aimed at creating mutually exclusive painted and non-painted granite colour classes in the YUV colour space were carried out. Two tests with red painted granite and blue painted granite were undertaken.

Methodology: A small quantity of the -20+15mm fraction was painted with red and blue proprietary emulsion paint. These samples were then put across the sorter and pictures captured. A captured picture of each sample group (see Figure 3.13) was converted by the automated sorter from the RGB to the YUV colour configuration. The non-painted granite samples showed no overlap with blue painted granites in the U and V colour space, unlike the red painted granite which overlapped with the background in the UV colour space. Table 4.1 indicates the YUV values of blue and red painted -20+15mm fraction.

Table 4.1: YUV values of blue and red painted particles (-20+15mm fraction)

Classification	Y Min	Y Max	U Min	U Max	V Min	V Max
Background	70	150	0	85	0	85
Blue	40	90	130	245	85	125
Red	30	90	80	120	175	255
Granite	70	180	85	130	125	185

The red painted granite also overlapped with the non-painted granite in the U colour space. These results led to the choice of blue colour to paint the granite samples as the blue-painted granite did not overlap in the U and V colour space (see Figure 4.4).

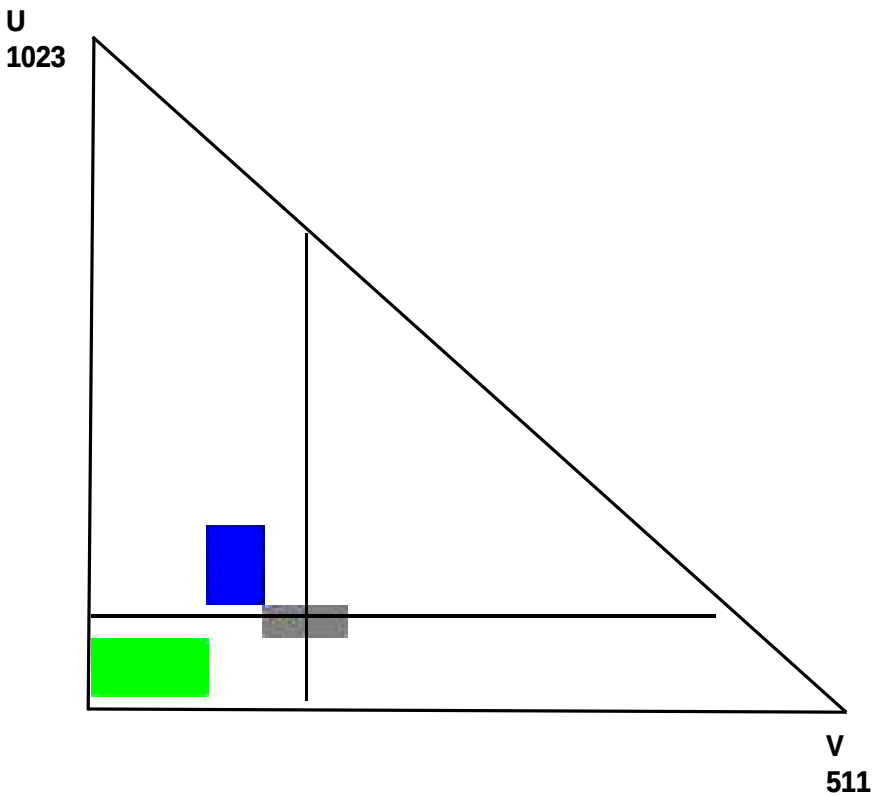

Figure 4.4: UV colour space classification of the blue painted granite, granite and the background

4.2.2 Optimisation tests

After the appropriate paint colour was determined, it was necessary to set the automated sorter to its optimal conditions suitable for the granite

particles before carrying out the efficiency tests. To achieve these optimal conditions, tests were undertaken to investigate the positioning of the splitter which separates the collector bins, the air pressure, settings for rejection of particles (rejection rule) and throughput.

Throughput determination: To calculate throughput, each sample fraction was passed through the feeder. The quantity of particles collected after ten seconds was weighed. From the results, the throughput was calculated using the relationship

Mass collected in 10 s = X(kgs^{-1})

Throughput = 0.36 * X (*tonnes/hr*)

For example, if eight kilograms of cubic shaped -20+15mm particles was collected in 10 seconds, the throughput was calculated to be 2.88tonnes/hr. Each test was repeated three times, with the average value taken to represent the throughput.

The cubical shaped fraction produced a higher throughput than flaky shaped fraction because these particles have greater unit weight. The throughput calibration for the -10+6mm, the cubic shaped -20+15 and -15+10mm fraction is shown in Figure 4.5.

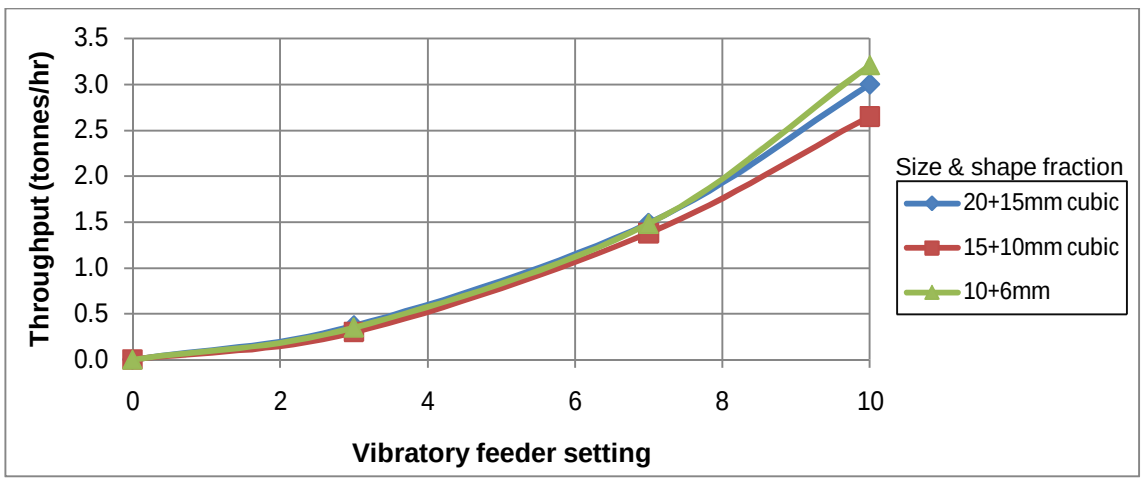

Figure 4.5: Throughput calibration of some of the sample fractions

Delay time and compressed air pressure tests: The automated sorter is equipped with a delay time factor. This is a machine processing time factor relating to the distance between the scanning line of the line scan camera and the bank of compressed air nozzles. Incorrect delay time may lead to poor deflection of particles.

Methodology: At a throughput of approximately 2.5tonnes/hr, five kilograms each of the -20+15 and -10+6mm fraction representing the coarser and finer size fractions were passed over the sorter. The sorter was set to deflect all the particles. First the compressed air pressure was set to a lower setting of 50kNm^{-2}, the delay times were varied between 20 and 30ms (beyond this range, the air jets misfired) and the efficiency of ejection was recorded. The efficiency of ejection was determined by weighing the amount of particles in the accept bin, dividing that by the total weight of particles passed over the sorter. The compressed air pressure was recorded from the air pressure gauge fitted on the sorter, which can be varied using an adjustable knob, up to the upper limit of 550kNm^{-2}. Replicate tests were performed at pressure increments in 100kNm^{-2} multiples. The results for the -10+6 and -20+15mm fractions are shown in Figures 4.6 to 4.8.

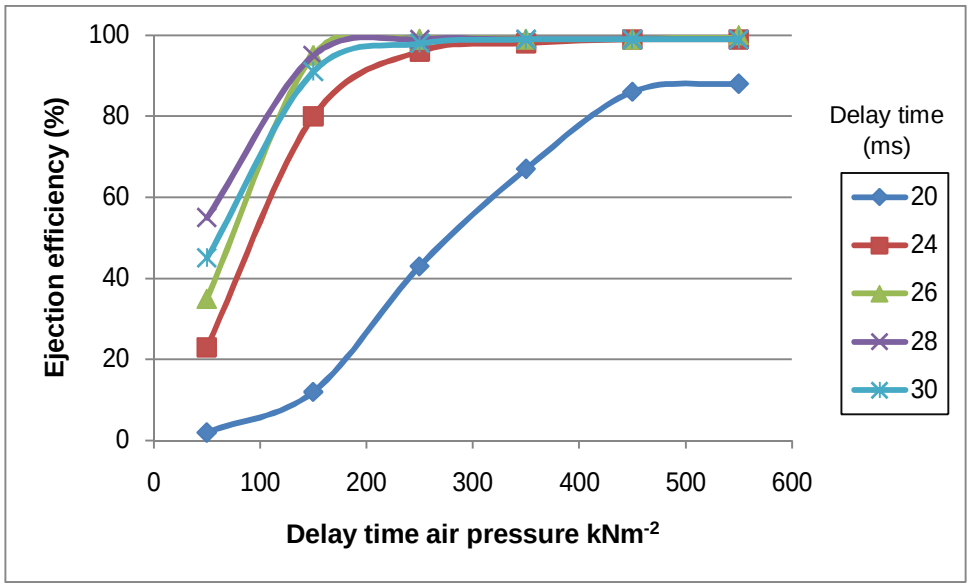

Figure 4.6: Delay time test results for -10+6mm fraction

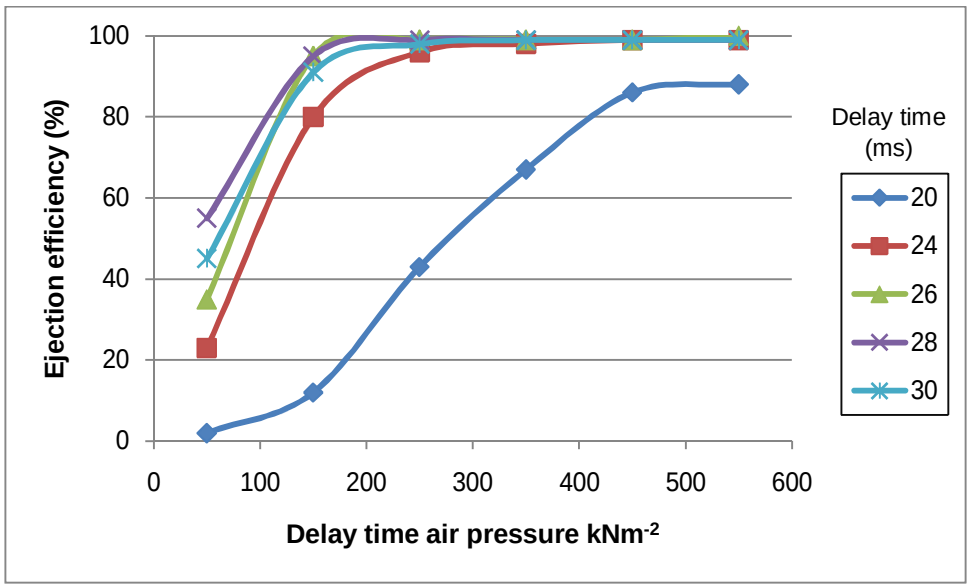

Figure 4.7: Delay time test results for cubic shaped -20+15mm fraction

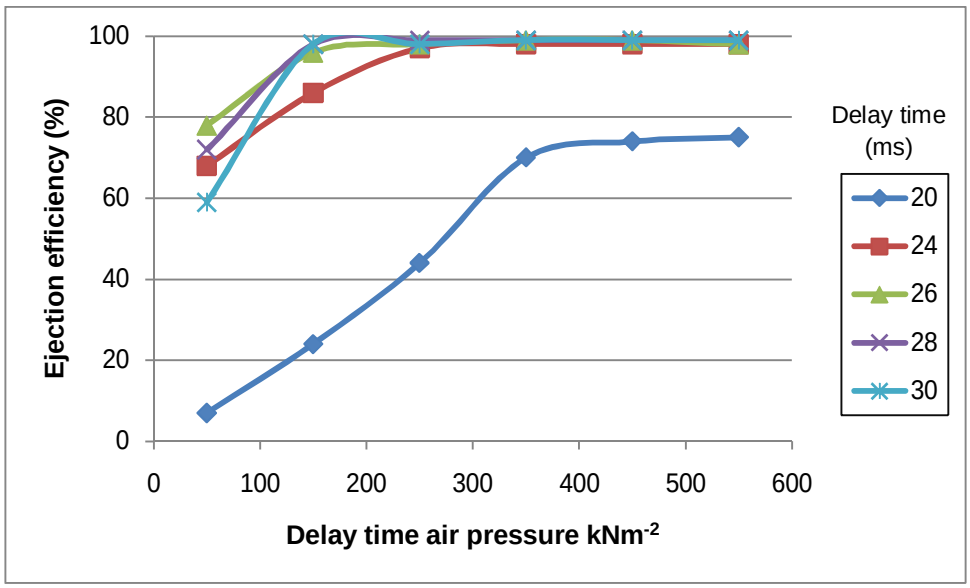

Figure 4.8: Delay time test results for flaky shaped -20+15mm fraction

The tests indicated that at 20ms, the ejection efficiency was not maximised and is lower than for the 24 to 30ms range. At 24ms the ejection efficiency only improved with an increase in air pressure. The delay time of 26ms was chosen as the ejection efficiency is maximized at this delay timing.

Splitter positioning: The position of the splitter influences the separation of the feed materials into either accept or the deflect collector bins. Figure 4.9 shows the positioning of the splitter plate with respect to the edge of the conveyor belt, the positioning of the valve nozzles are also indicated.

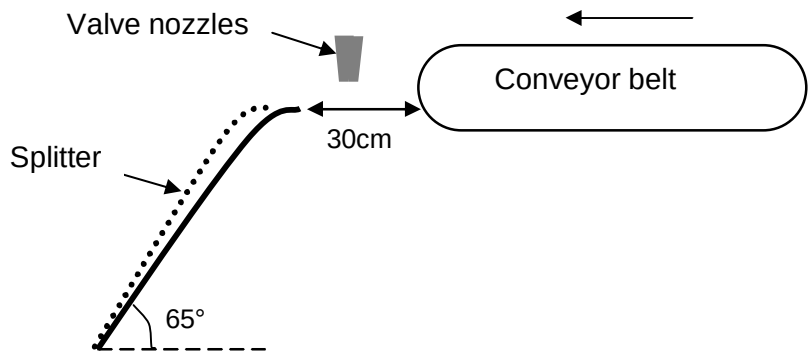

Figure 4.9: Positioning of the splitter with respect to the edge of the conveyor belt

Methodology: Approximately fifty granite particles for each of the size fractions were first passed over the automated sorter, with the splitter inclined at 62° from the horizontal (about 27cm from the tip of the conveyor belt to the tip of the splitter plate), at 65° (30cm), 68° (33cm) and 75° (37cm). The splitter plate was adjusted accordingly until there was no interference between the splitter and the particles. Each angle of inclination was measured utilising a Moore and Wright clinometer. The ideal inclination angle was determined to be 68° for the -20+15 and -15+10mm fraction and 65° for the -10+6mm fraction.

As a validation test 10kg of the cubical shaped -20+15mm fraction was passed over the belt at throughput of 3tonnes/hr utilising the 68° position of the splitter. Any incorrect deflections were noted and Table 4.2 indicates the incorrect deflections over five tests.

Table 4.2: Splitter deflection test results

Test No.	Number of incorrect deflections	Total number of particles recorded**
1	0	1565
2	3	1607
3	3	1589
4	2	1593
5	0	1655
Total	8 (0.09%)	8009 (99.9%)

**** The total number of particle was determined utilising the image processing analyser of the automated sorter**

Optimal air pressure: Insufficient air pressure also affects separation efficiency. To obtain the optimal air pressure for each size fraction, the combination of optimised splitter positioning and the delay time previously discussed were utilised. Optimal air pressure tests differ from the delay time tests because the delay time is fixed. The objective was to produce full deflection of the required particles with the minimum air pressure.

Methodology: With a setting to deflect all the granite at a fixed delay time of 26ms the efficiency of separation was used to determine the air pressure. At increments in 100kNm^{-2} multiples, tests were undertaken at air pressures ranging between 50 and 550kNm^{-2}. For each test run, approximately ten kilograms of non-painted granite was passed over the sorter. The mass balance of deflection was utilised in calculating the separation.

$$\text{Separation (\%)} = \frac{\text{Weight of deflected material}}{\text{Total weight of material passed over the sorter}} \times 100$$

The optimal air pressures utilised for the various material groups are shown in Table 4.3.

Table 4.3: Optimal air pressures for the various size fractions and shapes

Size fraction (mm) and shape	Optimal air pressure (kNm^{-2})
-20+15, flaky	500
-20+15, cubical	550
-15+10, flaky	400
-15+10, cubical	450
-10+6	350

The chosen air pressures are the point from which the air pressure indicates consistent separation up to $550kNm^{-2}$ for all the other size fractions with exception of the cubic -20+15mm fraction where the maximum compressed air available ($550kNm^{-2}$) was required.

Reject rule tests: Reject rules are separation rules programmed into the automated sorter. The rules control the number of valves that would be activated to deflect particles. Reject rule tests were undertaken to identify the reject rule for the automated sorter that would yield the highest separation between rejection rules 1 and 3. Reject rule 1 activates all valves within the width of the bounding box with one valve centred around the middle of the bounding box created around the particle. Reject rule 3 activates one valve at the horizontal position of the centre of gravity of the bounding box.

Methodology: At the throughputs of 0.5 and 2.5tonnes/hr and air pressures of 400 and $550kNm^{-2}$, approximately ten kilograms of painted (blue) and non-painted (granite) -10+6mm fraction were passed over the sorter. The finer size fraction was used for the tests as there was insufficient compressed air to deflect the coarser sizes at rejection rule 3. The mixture of the blue to granite was 10% blue and 90% granite. The tests were set to deflect all the blue. The number of misplaced blue (I_b) representing blue particles that are found in the accept collector bin, and co-deflected granite (I_g) representing granite particles deflected together with the blue particles, were hand-sorted weighed and the results are shown in Table 4.4. The

percentage of co-deflected and misplaced particles was used to determine which rejection rule was most effective.

Table 4.4: Misplaced and co-deflected particles at reject rule 1 and 3 for -10+6mm fraction

	Reject rule 1 at 400 kNm^{-2}		Reject rule 3 at 400 kNm^{-2}	
Throughput (Tonnes/hr)	I_b(%)	I_g(%)	I_b(%)	I_g(%)
0.5 2.5	0.4 0.3	1.3 9.5	0.2 3	2.2 13
	Reject rule 1 at 550 kNm^{-2}		Reject rule 3 at 550 kNm^{-2}	
Throughput (Tonnes/hr)	I_b(%)	I_g(%)	I_b(%)	I_g(%)
0.5 2.5	0.3 4	1.7 11	0.9 4	1.5 10

Insufficient deflection explains the poor blue separation in reject rule 3 when compared to reject rule 1. It was observed that for a reject rule 1 scenario, if several valves deflect the particles it is likely that the 'G' representing the granite particle would be co-deflected as shown in Figure 4.10(a) even though the 'B' representing the blue particle is the particle required to be deflected. However considering a reject rule 3 scenario (Figure 4.10(b)) for the same particle, the 'G' particle may not be deflected. Investigations suggest that the 'B' particle may not be deflected especially when the air pressure is not sufficient for deflection.

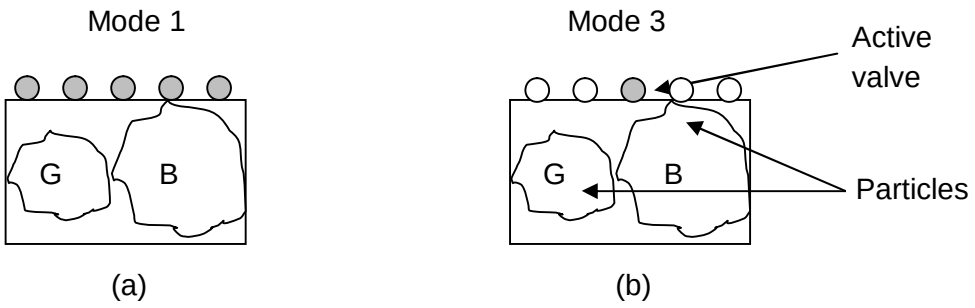

Figure 4.10: Deflection scenarios for reject rules 1 and 3

Material rule colour setting tests: In Chapter 3 the material rule settings (Geometry, Colour and Metal) were discussed. These are cut off settings utilised to control the deflection of particles from the sorter. These settings also form a part of the decision making criteria used to instruct the activation of valves. The settings range between zero and one hundred. For the 'colour' material rule setting for instance, a 20% cut off indicates that any particle with blue pixel intensity of 20% or more is considered as a particle requiring deflection. Tests were undertaken to compare the effects of different cut off settings on separation efficiency.

Methodology: At 0.5tonnes/hr throughput, 10% blue particles required to be deflected and 500kNm^{-2} deflection air pressure, a total of approximately 4500 blue and granite flaky shaped -20+15mm particles were passed over the sorter in three batches. The image processing analyser was used to collect data and analyse the average range for blue particle intensities. Ten percent blue deflection and low throughput were chosen as test observations indicated that there was a lower probability of touching particles affecting the collected data especially at the lower throughputs. The results obtained are stated in Table 4.5. From these results the 20 and 50% cut off were selected for further investigation.

Table 4.5: Cut off value test results

Cut off value (%)	Percentage of total blue particles (n = 803)
20	99
30	97
50	87
>70	63

Results for the investigations are discussed in section 4.2.3.

4.2.3 Separation efficiency tests

Separation efficiency tests were used to measure sorting efficiency, undertaken at the previously determined optimal sorter settings, at varying throughput, air pressure, sizes and shapes.

Methodology: Ten kilograms of the samples were weighed out to give the desired percentage of blue from 10 to 50%. The blue and grey granite were thoroughly mixed before being fed to the sorter. To confirm that the particle distribution from the chute was random the particle positioning data from the image processing analyser was used. The percent blue influences the probability of blue and granite samples occurring in close proximity warranting investigations to ascertain their effects on separation efficiency. The separation was undertaken using the YUV colour classification shown previously in Figure 4.4, with a preset material setting to reject the blue particles of greater than 20% blue pixels intensity. All tests were undertaken using reject rule 1. The tests were carried out at throughputs ranging between 0.5 and 2.5tonnes/hr for all the samples. In all cases, blue particles were deflected. To determine the repeatability of the tests, all tests were repeated four times at 10, 30 and 50% of blue particles requiring deflection.

After sorting the separated particles were collected in the two bins under the sorter. The separated products were then hand sorted into the two colour categories and the products weighed using a Sartorius MC 1 LP34000P weighing scale, accurate to 0.1 grams to produce a mass balance.

At 500kNm^{-2} deflection air pressure for 10, 30 and 50% blue particles requiring deflection, and a throughput of 1.5 tonnes/hr separation efficiency tests were undertaken to compare the effects of the two cut off settings. The separation efficiency results are shown in table in Table 4.6.

Table 4.6: Comparison between 20% and 50% cut off values based on separation efficiency for flaky shaped -20+15mm fraction (at a 50% deflection)

Cut off value (%)	Separation efficiency (%)	Incorrect deflections (%)	
		I_b	I_g
20	90.7	0.3	9.0
50	89.6	6.0	4.4

I_b = Incorrect blue painted granite, I_g = Incorrect granite

As was expected the 20% cut off meant that all the blue particles would be deflected although with granite. The 50% cut off yielded lesser co-deflection of grey granite. For the purpose of these investigations the 20% cut off setting was chosen for all the separation efficiency tests to ensure highest recovery of blue granite. The results demonstrate the compromise that has to be made between recovery and product concentration.

The separation efficiency results are discussed in Chapter 5, sub-section 5.1.

4.2.4 Particle proximity tests

According to De Jong *et al* (2005) and Arvidson (2002), singularisation of the particles is an important efficiency factor of the automated sorter as 'touching' particles may lead to co-deflections.

An estimate of the particle proximity can be determined using data obtained from the image processing analyser fitted on the automated sorter. The image processing analyser can record up to 2000 particle positions and dimensions when the particles cross the scanning line of the camera. These data were used to obtain particle proximity information and analyse valve and deflection relationships.

Methodology: For each size and shape fraction approximately 1000 particles were passed singly over the automated sorter. The particles were passed singly to ensure that no particles were touching each other. The information gathered could be used to study particle surface area (in pixels) for each size and shape fraction. The image processing analyser recorded the particle characteristics. This data was then transferred into *Excel* Microsoft software to convert the particle proximity data (converting from pixels to mm) to facilitate calculations.

The mean, standard deviation and the variance of the surface area data for a particle were determined. The next step was to determine the points (s or d in Figure 4.11) which would be recognised as the boundary between

the surface areas for single or double particles. Particles indicating greater than a single surface area were referred to as composites.

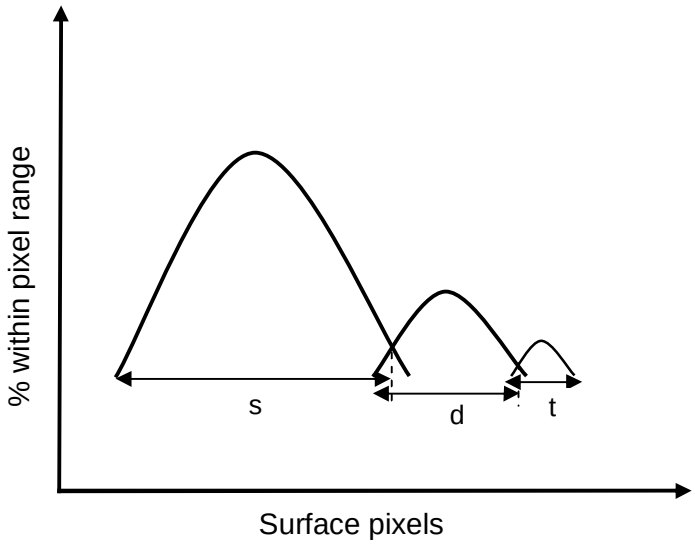

Figure 4.11: A diagram indicating the points where composite boundaries were delineated

The value representing **s**ingle, **d**ouble, **t**riple up to six composites was calculated using the 'solver' of the *Excel* Microsoft software. The calculations assume that the distribution of the particles on the conveyor belt is normal. This assumption was confirmed by plotting the distribution of surface area (see Figure 4.12) obtained from the data collected from the approximately 1000 particles for each size fraction.

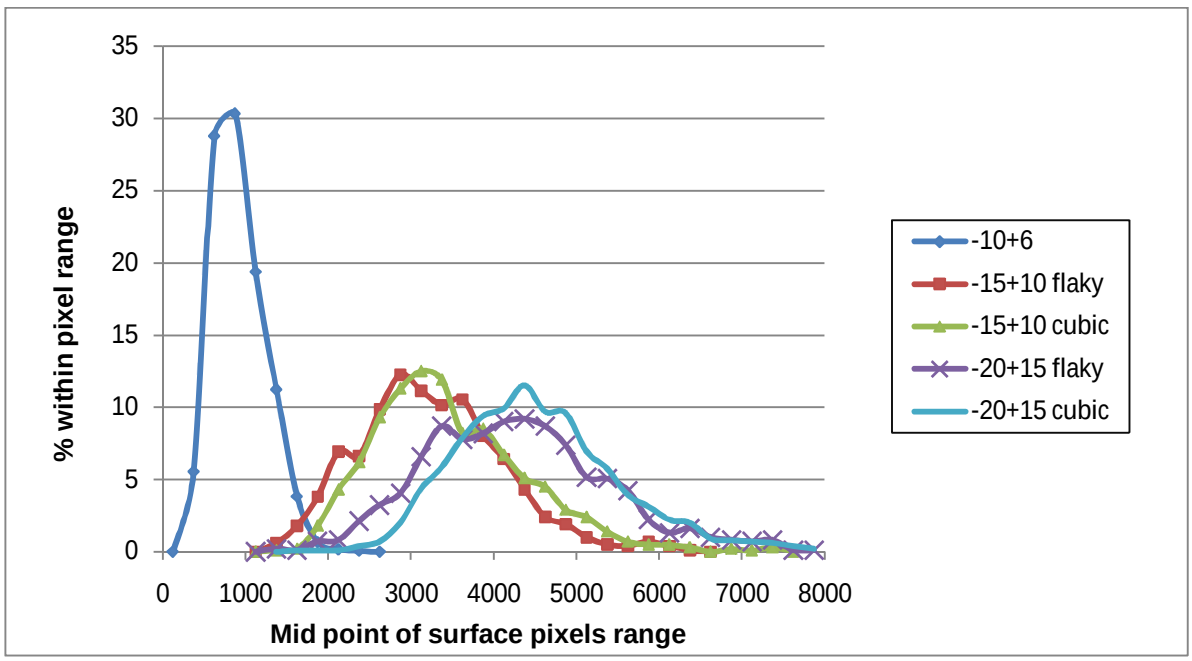

Figure 4.12: Distribution of particle surface pixels for all size fractions

Figure 4.12 indicates that for each size and shape fraction the particles vary in surface area. The -10+6mm fraction however shows the least variation in average surface area. It can also be seen that the particle surface pixels generally have a normal distribution, with the cubic shaped size fractions producing smoother curves.

Further calculations involved the use of the mean and standard deviation of the surface area data collected. For a single particle the mean surface area and standard deviation are utilised in calculations. For a double composite twice the mean and the square root of twice the variance is used to determine the standard deviation. For a triple composite thrice the mean and the square root of three times the variance is used. This process is repeated for up to six composites.

Next the cut points delineating single, double and so on particle surface areas are determined. For a specific throughput and particle size fraction, the image processing data collected was analysed. To calculate the composite cut points a value 'x' (which could represent s, d or t) ranging between 0.85 and 0.99 is selected. This value would prove true that the mean and standard deviation obtained for the surface areas is a normal distribution. This is calculated using the 'solver' in *Excel* Microsoft software. The obtained 'x' values are then used to calculate the number of single, double and so on composites obtained for each dataset. Table 4.7 shows an example of data obtained for the -10+6mm fraction.

Table 4.7: Example of cut point values determined for -10+6mm fraction ('x' set to 0.95)

Number of composites	Mean	Standard deviation	Cut point surface area value	Normal
1	839	313.03	1354	0.9500
2	1678	442.70	2406	0.9499
3	2517	542.19	3409	0.9500
4	3356	626.07	4386	0.9500
5	4195	699.97	5346	0.9499
6	5034	766.77	6295	0.9499

Mean = 839, standard deviation = 313.03, variance = 97987.78

For this example, any particle with surface area >1354 but < 2406 was considered a double.

The next procedure was to determine the approximate 'x' value ideal for each size and shape fraction. As the mean surface area is known for each test situation, the composites data is then used to calculate the mean surface area. The calculated mean surface area is then compared with the actual mean surface area previously obtained when the particles were studied singly.

Assuming 5000 particle surface areas are obtained from the image processing analyser with a mean surface area of 1200. A cut point value of 0.90 for the 5000 recorded particles positions yields results showing that 84% are single 5% double and 2% triple, this information is then used to calculate the mean surface pixel area thus:

First the number of particles is determined to be
Single = 4200 particles (84% of 5000)
Double = 250 particles (5% of 5000)
Triple = 100 particles (2% of 5000)

As the mean pixel value is 1200, therefore the mean pixel area of the above example would be

$$\frac{4200*1200+(2*250*1200)+(3*100*1200)}{4200+250+100} = 1318.68$$

If the values are close then the cut point is taken otherwise the process is repeated by decreasing or increasing the 'x' value until a value close to the known mean pixel area value is obtained. For the example above the obtained value (1318.68) is greater than the mean pixel area value (1200). Hence the 'x' value is changed to say 0.93 and the process repeated until the value obtained is close to the mean pixel area value.

Assuming that the repeat of the process at an 'x' value of 0.93 yields 89% single 4% double and 1% triple. Calculating the number of particles

Single = 4450 particles (89% of 5000)
Double = 125 particles (4% of 5000)
Triple = 50 particles (1% of 5000)

As the mean pixel value is 1200, therefore the mean pixel area of the above example would be

$$\frac{4450*1200+(2*125*1200)+(3*50*1200)}{4450+125+50} = 1258.38$$

With this value closer to the known mean surface area of 1200 then the 'x' value of 0.93 is used as the cut of point value.

This process is then repeated for the various throughputs, sample fractions and repeats carried out to determine separation efficiency. These results are presented in Chapter 5, sub-section 5.2.3.

4.2.5 Video observations

Apart from recordings of particle proximity, the Sony© HDR-SR5E camcorder was utilised for the video observations of the particles as they travel on the conveyor belt. The Sony HDR-SR5E is a conventional high definition video camera, with the facility to record 3-second batches at higher frame capture rates of up to a 100 frames/sec. Information on the distribution of particles across the belt width including interactions between the grey and blue granite particles was collected using this method.

Methodology: The granite particles were passed onto the belt at the desired throughput and video clips were taken by placing the camera overlooking the belt and recording the display/distribution of the particles on the belt (see Figure 4.13).

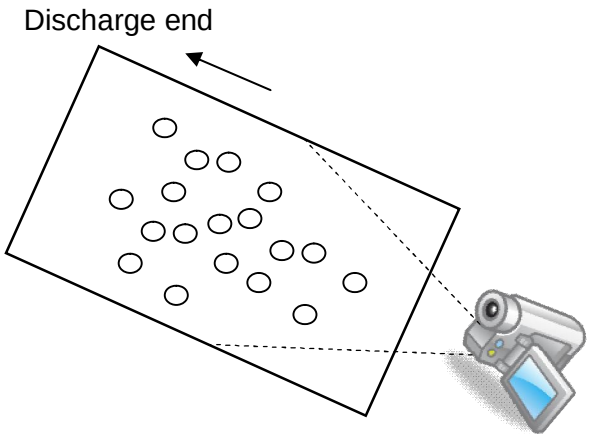

Figure 4.13: Schematic showing the position of the video camera with respect to the conveyor belt and particles

The various frames taken were then studied using the *Picture motion browser* of the Sony© HDR-SR5E software, which allows a frame-by-frame study of the video recording. Plate 4.2 is a picture of a typical frame.

Plate 4.2: Picture of a frame of cubic shaped -20+15mm samples

The frame-by-frame video observations were analysed to determine particle distribution on the belt, results are indicated in Figure 4.14. The results were comparable to what was obtained using the image processing analyser of the automated sorter (see sub-section 4.3.3). Investigations indicate that approximately 75 to 83% of the particles discharge in the middle 30cm portion of the belt this is because the discharge trough has a width of 13cm relative to the belt width of 55cm.

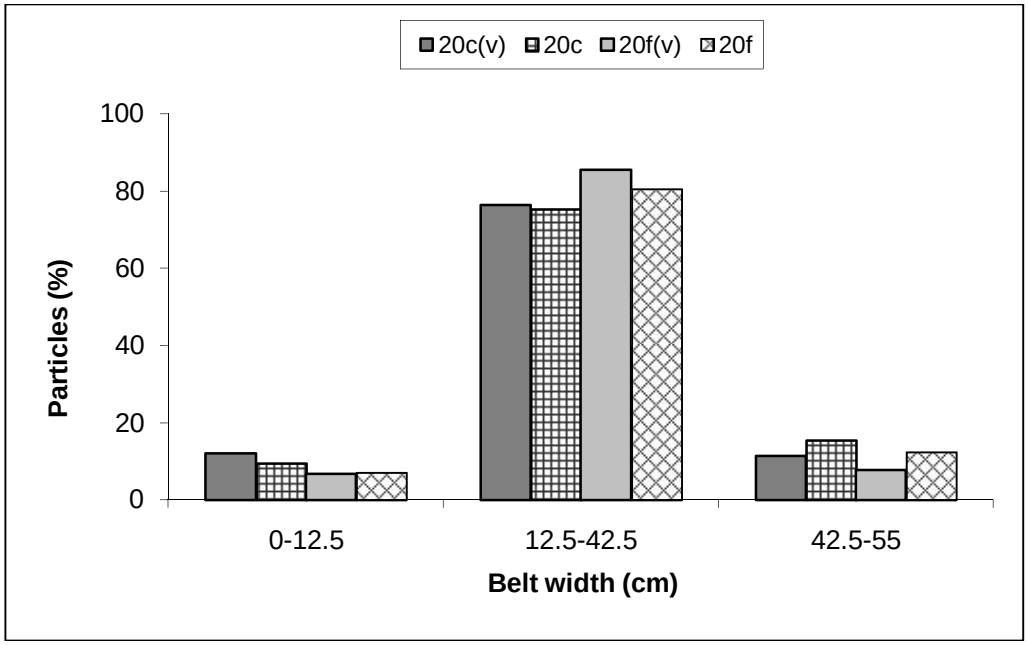

Figure 4.14: Belt distribution of -20+15mm sized particles

Where:

20c = -20+15mm cubical shaped samples

20c(v) = -20+15mm cubical shaped samples from video observation

20f = -20+15mm flaky shaped samples

20f(v) = -20+15mm flaky shaped samples from video observation

4.2.6 Valve precision tests

To determine valve precision a means to measure the zone of influence of each valve was designed. From this information the probability of a particle being co-deflected could be determined, together with information on the effects of the compressed air jets on the particle deflection.

Methodology: Particles of the coarser (flaky shaped -20+15), intermediate (cubic shaped -15+10mm) and finer (-10+6mm) fractions were placed on the sorter at predetermined positions represented in Figure 4.15a.

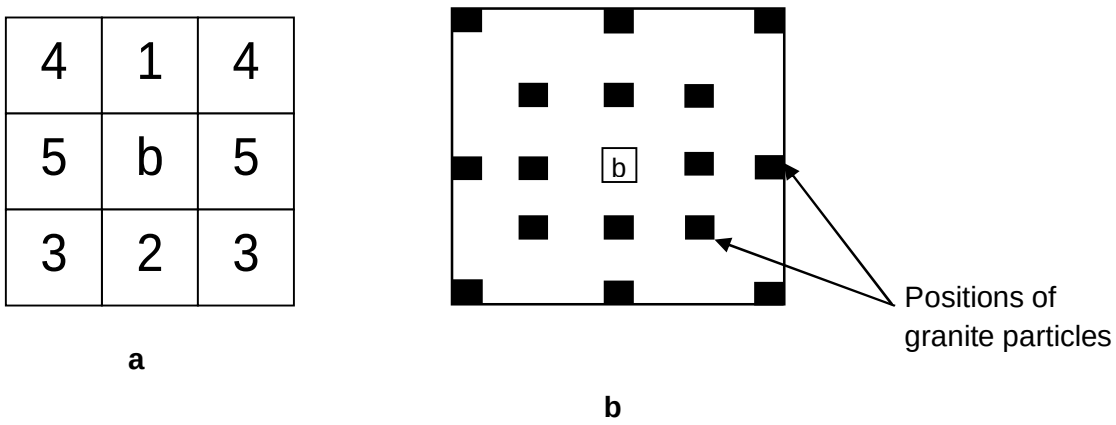

Figure 4.15: A diagram indicating positions of the blue (b) and granite particles utilised to determine zone of influence of sample composites

The granite particles were placed with reference to the blue particle (b) adjacent, beside on the top or below. Ten pairs of blue and granite particles were placed together on a stationary belt before the belt was switched on passing the particles over the sorter. Subsequent tests were at measured distances in 2mm multiples (representing the approximate distance between each valve nozzle) from the blue particle as shown in Figure 4.15. Figure 4.15a represents the predetermined positions while figure 4.15b shows the predetermined positions for two measured distances. This distance between particles, measured with a Mitutoyo vernier calliper (see plate 4.3), was increased until there were no co-deflections. In all cases the automated sorter was programmed to deflect the blue particle and each position batch was repeated 10 times (approximately 100 particle pairs in total per batch).

Plate 4.3: A picture of coarse particles placed before a test (measured using a mitutoyo vernier calliper)

The effect on each particle was determined by measuring which of the particles were correctly deflected into the collector bins; together with the observations of particle position as recorded by the image processing analyser of the sorter. To ensure that the space between each particle was maintained while travelling on the belt, stable (flat shaped) particles were chosen. Video recordings of tests were recorded for comparison with tests. A 3-second recording of the particles as they leave the belt was captured using a Sony© HDR-SR5E recorder. Five recordings were taken. These recordings indicate that the particles rarely move from their original belt position. Utilising the *Picture motion* Sony software, relevant frames of the video were extracted. Pictures of 4 frames are shown in Plates 4.4 and 4.5, showing the progression of the particles off the belt.

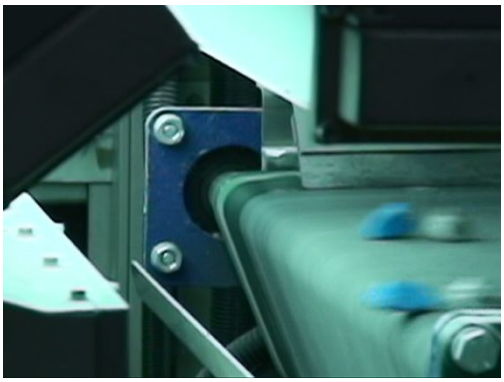

1

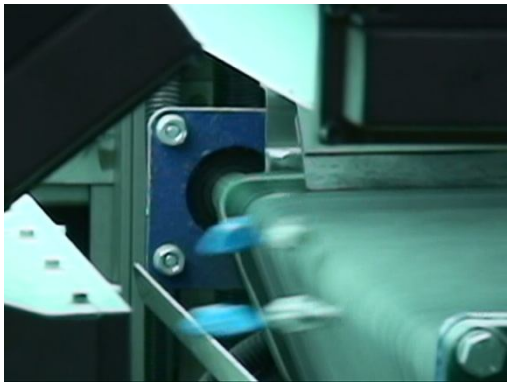

2

Plate 4.4: Progressive video frames (progressing from 1 to 2) 2 frames apart (sample positions in a position 3 configuration from Figure 4.15a)

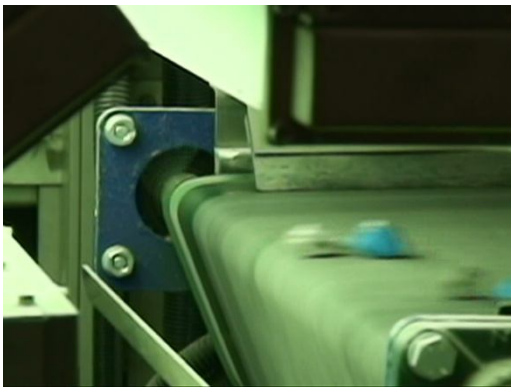

1

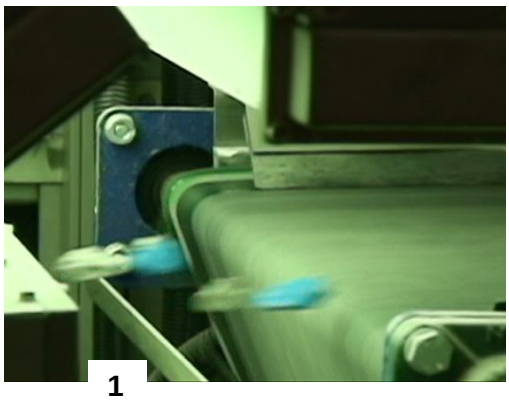

1

Plate 4.5: Progressive frames (progressing from 1 to 2) 2 frames apart (sample positions in a position 4 configuration from figure 4.15a)

4.2.7 Belt loading tests

The area of the belt covered by particles (belt loading) can be utilised to study the effects of throughput and particle interactions on separation efficiency. Investigations into belt coverage per test batch were utilised to compare with the results of separation efficiency obtained from the tests discussed in sub-section 4.2.3.

Methodology: There are two methods used in this research to determine belt loading. The first is based on the image processing analyser data while the other is based on particle dimensions and conveyor belt speed.

*Image processing analyser data method: ba*sed on the assumption that no particle rested on top of another, information on belt loading was obtained

from the image processing analyser recordings of the sorter. The methodology follows the schematic indicated in Figure 4.16, and uses information on acquiring data from the sorter previously discussed in Chapter 3, sub-section 3.1.6.

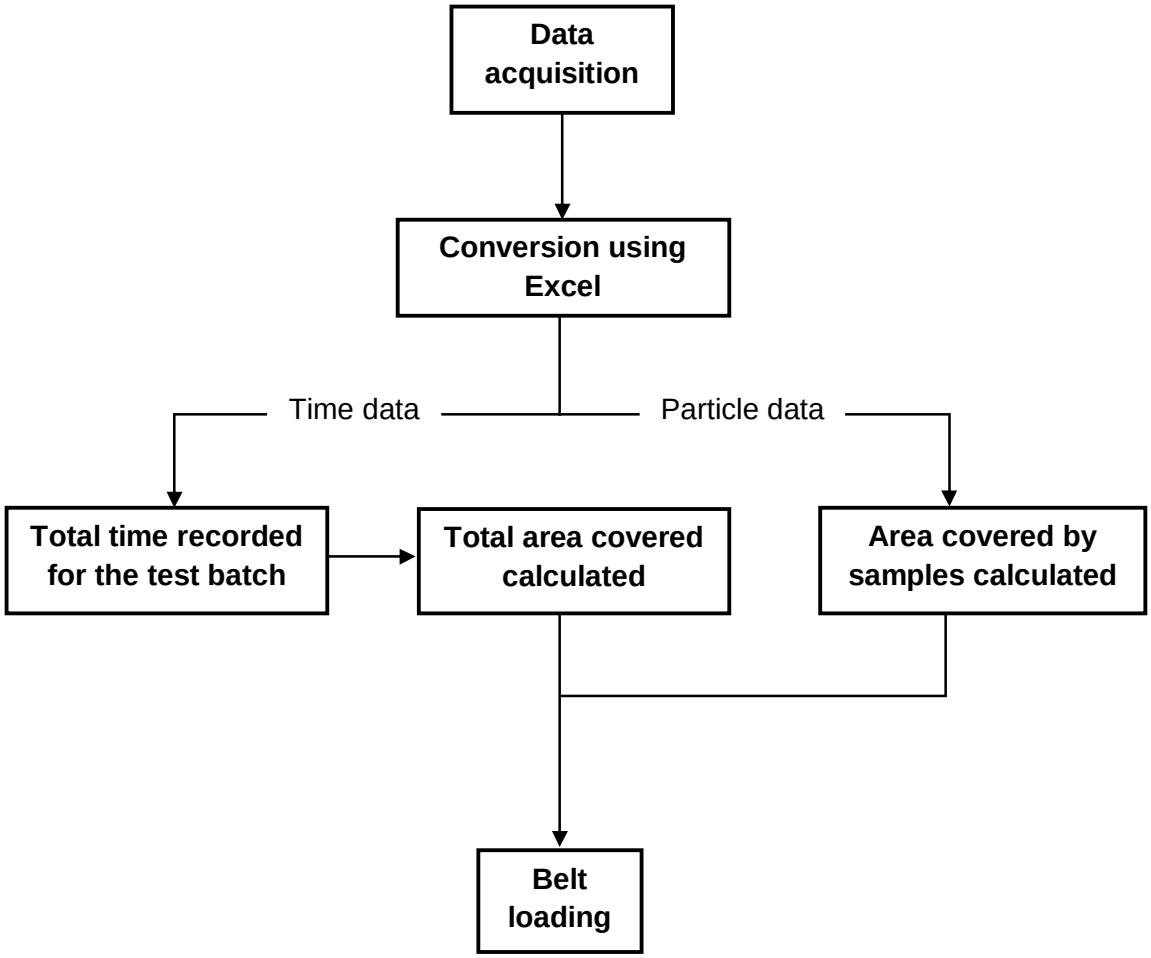

Figure 4.16: Flow chart indicating belt loading determination procedures

Each recorded test batch was converted into *Excel* Microsoft© software, the total time taken to run each batch was calculated excluding the first 200 recordings. This is because the time recordings of the image processing analyser normalize after the first 200 recordings approximately. From the converted length and width of each particle observed (from pixels to mm), the area covered by each particle was calculated. The total area covered by the samples in the time recorded was determined. As the speed of the belt and the width of the belt are known, the total area covered by the belt in the time taken is determined. The belt loading (B_L) is calculated as follows:

$$\text{Belt loading (\%)} = \frac{\text{Total recorded area covered by samples}}{\text{Total area covered in time recorded}} \times 100$$

For data such as shown in Table 4.8, the belt loading was calculated to be 3.07 %.

Table 4.8: Converted data from the image analyser of the TiTech automated sorter for -10+6mm fraction

Obj. No.	Time	XMin	YMin	XMax	YMax	Surface	Width	Height	Blue	Granite	Other
2050	4411262	775	17377801	799	17377824	624	24	23	0	424	200
2051	4411276	1824	17377904	1845	17377916	323	21	12	0	28	294
2052	4411278	1092	17377909	1135	17377930	1051	43	21	840	0	211
2053	4411285	844	17377952	877	17377976	849	33	24	0	665	183
2054	4411305	1184	17378083	1213	17378105	627	29	22	0	421	206
2055	4411322	1031	17378204	1064	17378220	624	33	16	0	471	153
2056	4411352	1361	17378395	1393	17378423	942	32	28	0	606	335
2057	4411356	1427	17378434	1458	17378446	443	31	12	0	256	186
2058	4411363	1453	17378475	1477	17378493	495	24	18	0	278	217
2059	4411390	137	17378659	164	17378675	563	27	16	0	240	323
						Total	**297**	**192**	**297x192 = 57024**		

The time difference is 128 milliseconds,

(4411390 – 4411262) = 128ms

At a belt speed of $3ms^{-1}$ (3mm/ms), it follows that the distance travelled by the belt is 384mm. The area of the belt covered in this time period is $211{,}200mm^2$, a product of the width of the belt and the total distance covered.

Total area = length x width

Total area = 384mm x 550mm = $211{,}200mm^2$

The area of each particle in pixels is calculated to be 57024 square pixels. This is then multiplied by the constant representing the conversion of square pixels to square millimetres (0.12mm) discussed previously in Chapter three to produce a total area of $6843mm^2$.

Belt loading (%) = $\frac{6843}{211200}$ x 100 = 3.07%

Particle data and belt speed method: the particles were assumed to be rectangular with x, y, and z dimensions in millimetres. The screen fraction represented the x and y dimensions for instance 10 and 6mm for the -10+6mm fraction. The 'z' dimension was calculated from the average particle weight of approximately 500 particles (see sub-section 4.3.1) and sample density previously discussed in Chapter 2, sub-section 2.5.

The particle mass was calculated using the density-mass-volume relationship, where density (ρ) is the product of the mass (m) and the volume (V) of a particle making the mass of a particle to be estimated using equation 4.1.

$$m(kg) = \rho \ kgm^{-3} \ X \ V(m^3) \qquad (4.1)$$

Using the density of granite (as 2650kgm^{-3}), for a particle with x, y dimensions 10 and 6mm respectively, the 'z' dimension is calculated to be 4.7mm.

$$0.00075kg = 2650kgm^{-3} \ X \ (0.01*0.006*z) \ m^3$$

$$z(m) = \frac{0.0075kg}{2650kgm^{-3} \ X \ (0.01*0.006)m^3} = 0.047m$$

The unit mass of a -10+6mm particle is 0.00075kg, it follows that a 'z' dimension of 0.047m is the ideal diameter to make the product of the 3 components produce a mass of 0.00075kg. This is assuming that the density of the particle is 2650kgm^{-3}. This would produce a volume of 0.00000282m^3 and a mass of 0.000747kg (0.75 grams).

With the mass determined, the number of particles per second travelling over the belt was calculated with the throughput mass relationship. For a

throughput of 2.5tonnes/hr (0.6944kgs^{-1}), and mass of 0.000747kg, the number of particles is 93 particles per second.

$$\text{Number of particles} = \frac{0.6944\text{kgs}^{-1}}{0.000747\text{kg}} = 93\text{pct/sec}$$

If the x, y and z dimensions of the particles (n) and the number of particles processed per second N (pct/sec) are determined, then for a given throughput and belt width (W) in metres and speed (S) in ms^{-1}, the belt loading B_L can be estimated using equation 4.2.

$$\%\text{Belt loading} = 100 \times \frac{Nxy}{WS} \qquad (4.2)$$

4.3 MATERIAL DESCRIPTIONS

Three material size fractions are used in this research. They include -20+15, -15+10 and -10+6mm. This section describes the particle weight, the average surface area recorded for each size fraction extracted from the image processing analyser.

4.3.1 Particle weight

Approximately 500 particles of each size fraction selected from each quarter of the cone and split quarter were weighed using a Sartorius MC 1 LP34000P weighing scale, accurate to 0.1 grams from which the average particle weight was calculated. Results are shown in Table 4.9.

Table 4.9: Average particle weight data

Size fraction (mm) and shape	Average weight (g)
-20+15, flaky	5.07
-20+15, cubical	9.19
-15+10, flaky	2.68
-15+10, cubical	3.65
-10+6	0.75

4.3.2 Particle surface area

From the image process analyser the average surface area for each size fraction was calculated. The calculation was based on data from approximately 1,000 particles put singly over the automated sorter according to particle shape and size fractions. This data is shown in Table 4.10.

Table 4.10: Average particle surface area data

Size fraction (mm) and shape	Average surface area (pixels)
-20+15, flaky	4263
-20+15, cubical	4560
-15+10, flaky	3242
-15+10, cubical	3476
-10+6	918

4.3.3 Particle belt distribution

From the image process analyser data representing the belt distribution for each size and shape fraction was calculated. For each test the "X centre of gravity" (see Appendix A) value is used to represent the particle position on the belt. For instance and x centre of gravity value of 1000 indicates that the particle travelled past the line-scan camera at about the centre of the conveyor belt. This is because the conveyor belt is calibrated between 0 and 2000 or 0 and 55cm depending of the calibration scale used (see Figure 3.18). An average of all the 4 repeat tests for each fraction (approximately 10,000 particle positions) was used to calculate the belt distribution in a format similar to that shown in Figure 4.14. This data is presented in Table 4.11.

Table 4.11: Average belt distribution data

Size fraction (mm) and shape	Average belt distribution over 3 belt sections (%)		
	0 to 12.5cm	12.5 to 42.5cm	42.5 to 55cm
-20+15, flaky	7.3	79.7	13.0
-20+15, cubical	10.2	73.7	16.1
-15+10, flaky	6.7	81.8	11.5
-15+10, cubical	7.3	78.6	14.1
-10+6	8.0	78.9	13.1

These results indicate that between 74 to 82% of the particles come off the belt in the middle 30cm of the belt. These results are in agreement with those obtained by video observation shown in Figure 4.14.

CHAPTER 5

SEPARATION EFFICIENCY TEST RESULTS AND DISCUSSIONS

Chapter 4 described the procedures undertaken to study the effects of material and machine properties such as size, shape, percentage of blue particles to be deflected (% deflection) and throughput on separation efficiency. The results of the separation efficiency investigations are given in this Chapter. It was observed that an important factor affecting separation efficiency was co-deflected particles as a result of particles touching each other and forming composites.

If in a composite, a particle that was to be deflected was touching a particle that was to be accepted, the 'accept' particle could be co-deflected. The probability to which this may occur increased with a higher % deflection. Monte Carlo analysis was used to simulate the number of single particles that may be obtained during actual investigations and the results are also given in this Chapter. Monte Carlo analysis can predict composite formation assuming perfectly random distribution across the width of the belt. It is likely that non-random distribution will result in a greater likelihood of composite formation. The factors controlling sensor-based sorter efficiency deduced from these investigations are also discussed in this Chapter.

This Chapter is divided into 4 sections a section each discussing recovery of deflected blue particles, separation efficiency and sample proximity test results with the factors controlling automated sorter efficiency discussed last.

5.0 RECOVERY OF BLUE PARTICLES (R_g)

To calculate separation efficiency two variables (see equation 2.17) are required; the recovery of blue particles (R_b) and the recovery of co-deflected granite particles (R_g) into the deflect collector bin. Table 5.1 presents the average results for the separation of blue particles into the deflect bin for all the size fractions considered.

Table 5.1 Measure of efficiency of blue particle ejection

Size fraction (mm) & shape	R_b - Efficiency of blue particle ejection (%), for specified tonnage and % blue deflection									Overall Mean
	0.5 tonnes/hr			1.5 tonnes/hr			2.5 tonnes/hr			
	10 %	*30 %*	*50 %*	*10 %*	*30 %*	*50 %*	*10 %*	*30 %*	*50 %*	
-20+15, cubic	97.8	96.9	96.4	95.5	95.5	97.1	97.8	96.1	94.7	96.3
-20+15, flaky	99.8	99.4	99.5	99.7	99.3	99.7	99.5	99.5	99.4	99.5
-15+10, cubic	99.8	99.1	99.3	99.5	99.0	99.3	99.7	99.2	97.9	99.2
-15+10, flaky	99.8	99.7	99.7	99.5	99.7	99.6	99.2	99.4	98.8	99.5
-10+6	99.6	99.7	99.6	99.6	99.5	98.7	99.7	96.2	89.4	98.0

These results indicate that the average efficiency of blue particle deflection ranges between 96.3% and 99.5%. At the 10% blue deflect, some tests (e.g. -15+10mm at 0.5 tonnes/hr, 10% blue deflect) gave up to 99.8% blue particle deflection. An average of 99.5% efficiency of deflection is obtained for all the size fractions except for the -10+6mm and the cubic shaped -20+15mm fractions. This lowering in efficiency at a high % blue deflect and throughput for the -10+6mm fraction can be attributed to a reduction in compressed air supply when there was a high demand. This was a limitation in the laboratory compressed air supply. This observation was supported by a visual check on the pressure gauge fitted to the air manifold. It can be observed from the results that if the higher (30 and 50%) values of blue deflect are excluded, the average efficiency of deflection of blue particles at the -10+6mm size fraction was 99.6%.

For the cubic shaped -20+15mm particles the efficiency of deflection of the blue particles was found, under all conditions, to be significantly lower than for the other fractions. The most likely explanation is that the compressed air pressure and volume was not quite sufficient to deflect the heaviest particles under test as was indicated in Figure 4.7.

5.1 SEPARATION EFFICIENCY

In this section, results of the various separation efficiency tests are discussed.

5.1.1 Throughput and separation efficiency

Each separation efficiency test was repeated and Table 5.2 shows the summary of standard deviation for the test results indicating the variation between repeats. The complete results for the repeats of all the size fractions are given in Appendix C.

Table 5.2: Standard deviation for separation efficiency tests at varying % blue deflect and throughputs for all the size fractions

Size fraction (mm) and shape	STANDARD DEVIATION OF SEPARATION EFFICIENCY TESTS								
	0.5 tonnes/hr			1.5 tonnes/hr			2.5 tonnes/hr		
	10 %	*30 %*	*50 %*	*10 %*	*30 %*	*50 %*	*10 %*	*30 %*	*50 %*
-20+15, flaky	0.26	0.35	0.57	0.52	0.88	1.58	1.06	1.51	1.64
-20+15, cubic	1.63	1.34	1.59	1.55	1.84	1.13	1.10	1.06	0.96
-15+10, flaky	0.06	0.10	0.63	0.43	0.85	1.92	0.48	0.47	1.86
-15+10, cubic	0.41	0.24	0.35	0.23	0.99	0.96	0.80	0.78	1.36
-10+6	0.17	0.46	1.07	0.88	1.70	2.34	0.66	0.64	-

*** There was no data collected for the -10+6mm fraction at 2.5 tonnes/hr throughput with 50% blue deflection**

The standard deviation ranged between 0.06 and 2.34%. The highest standard deviation (2.34%) was recorded for the -10+6mm fraction. The deviations from the average separation efficiency were below 1.00% at 0.5tonnes/hr but between 1.00 and 2.00% at the higher throughputs indicating an increase in variation with an increase in throughput. These results show that the separation efficiency tests were repeatable.

Throughput and separation efficiency relationships for all the size and shape fractions follow similar trends as shown in Figures 5.1(a) and (b).

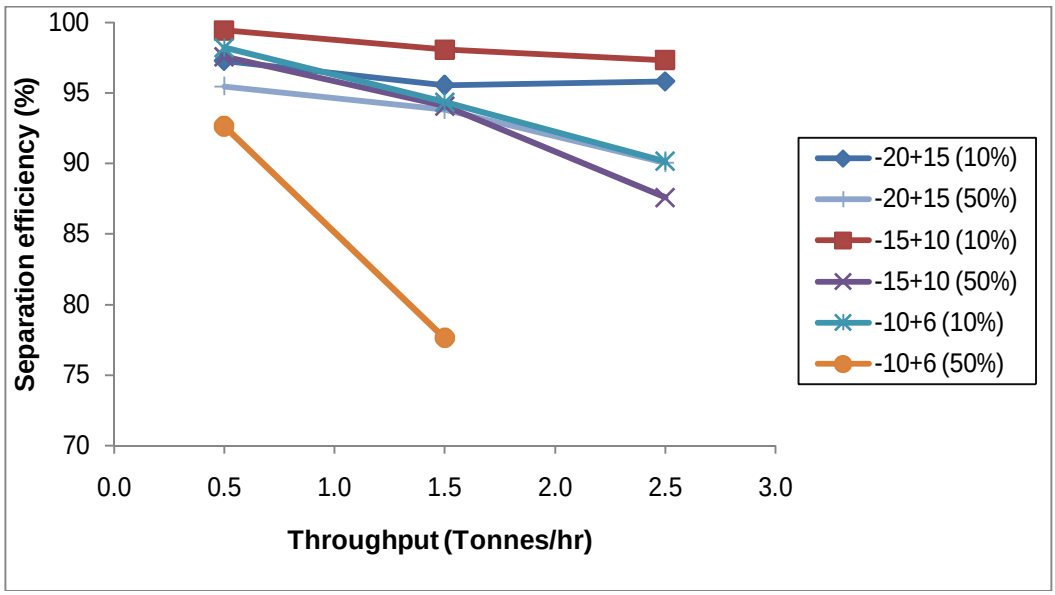

Figure 5.1(a): Throughput and separation efficiency relationships for cubic particles at 10 and 50% blue deflect

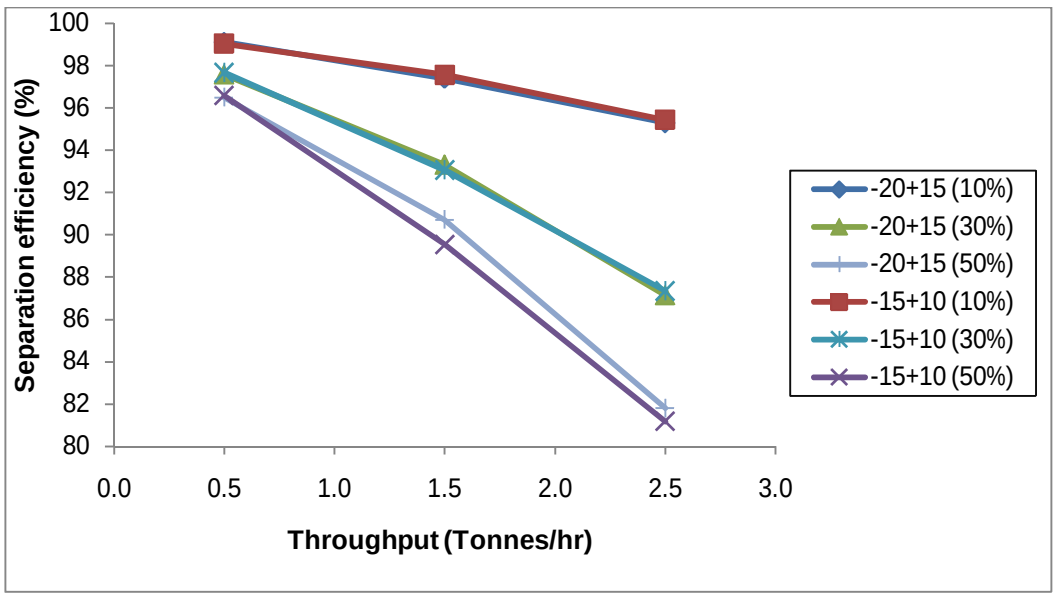

Figure 5.1(b): Throughput and separation efficiency relationships for flaky particles at 10, 30 and 50% blue deflect

These results indicate that separation efficiency generally decreases with an increase in throughput for all the size and shape fractions. Differences are observed between the 10, 30 and 50% blue deflect, with the highest separation efficiency recorded at the 10% blue deflect. A reason for this is the lower probability of having a blue particle occurring with a granite particle which would lead to a granite particle being co-deflected. For the

50% blue deflect the separation efficiency is consistently lower than for the 10% blue deflect. The reason for this (linked to the probability of occurrence of blue particle in close proximity) has been previously stated.

Figure 5.1(b) indicates that both the flaky shaped -20+15 and -15+10mm fractions have similar results at all blue deflects. This is not observed for the cubic shaped particles. This may be due to the stability of flaky shaped particles on the belt.

Apart from the -10+6mm size fraction at a 50% blue deflect, the difference between the maximum and minimum separation efficiencies for the cubic shaped fraction (a difference of 13) is lower than for the flaky shaped fraction (a difference of 19) indicating that the flaky fraction would yield worse separation efficiency at a higher throughput. This could be related to the increased belt area occupied by flaky particles at a specific throughput, where an increased belt area could lead to an increased probability of composite formation.

5.1.2 Percent blue deflect and separation efficiency

It is known that the percentage of particles to be deflected influences separation efficiency. Figures 5.2 (a) to (e) shows the results obtained from the investigations into the effects of varying the % blue deflection on separation efficiency.

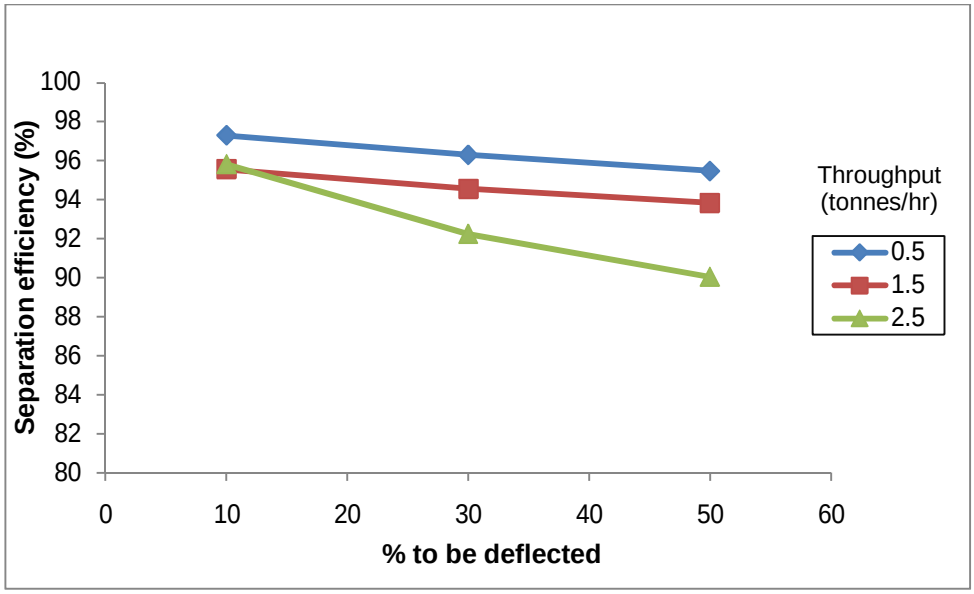

Figure 5.2(a): Relationship between separation efficiency and % blue deflect for cubic shaped -20+15mm fraction at varying throughputs

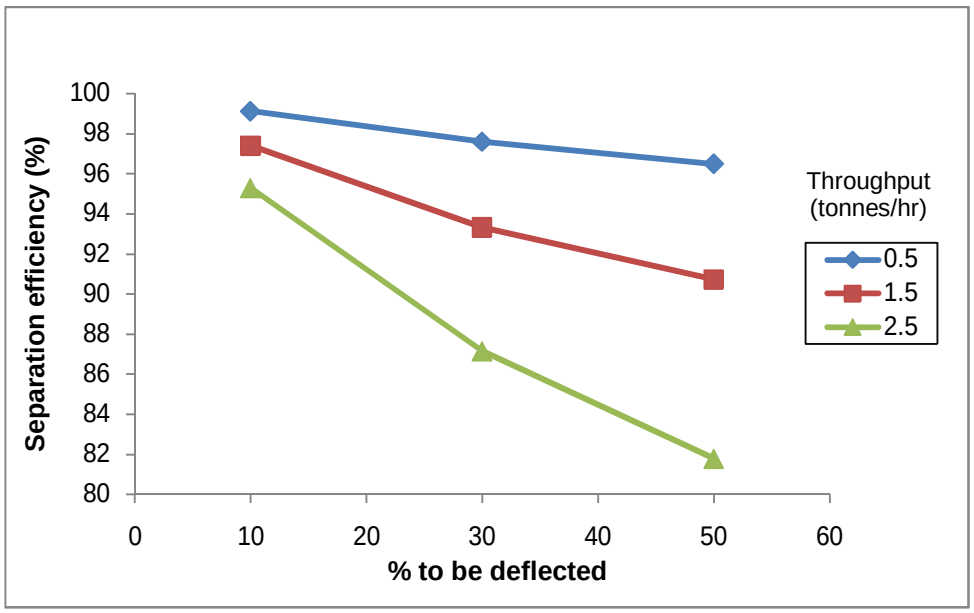

Figure 5.2(b): Relationship between separation efficiency and % blue deflect for flaky shaped -20+15mm fraction at varying throughputs

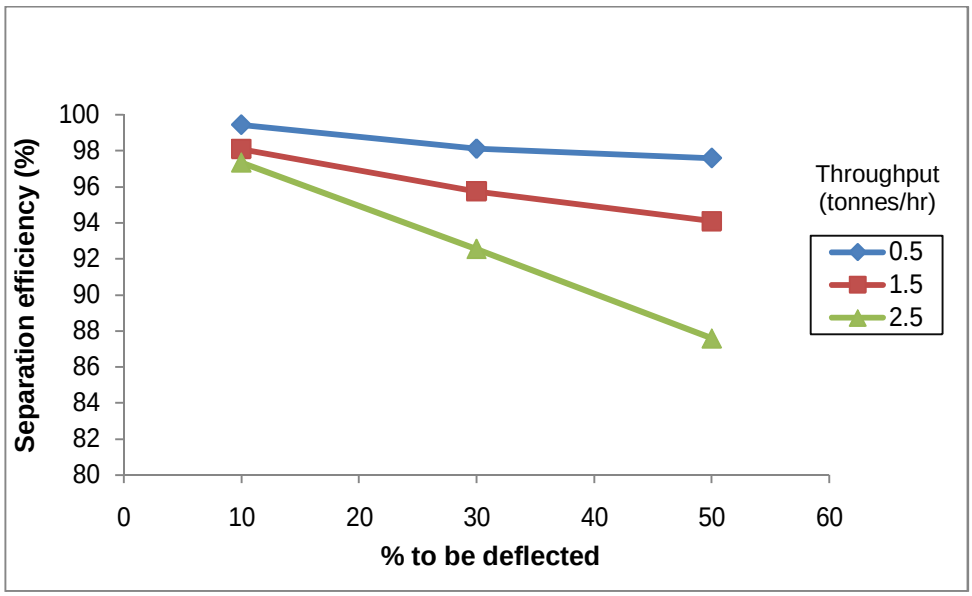

Figure 5.2(c): Relationship between separation efficiency and % blue deflect for cubic shaped -15+10mm fraction at varying throughputs

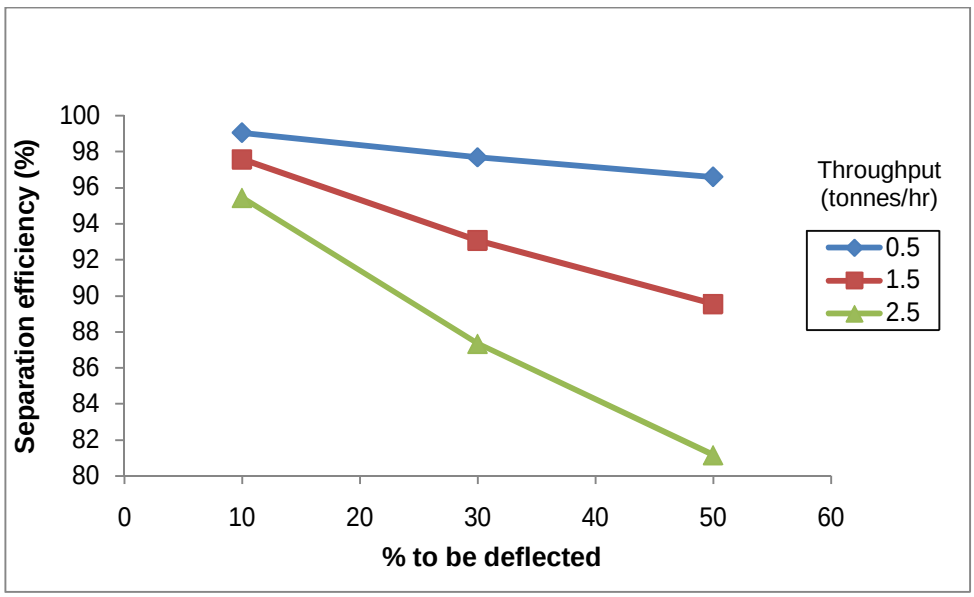

Figure 5.2(d): Relationship between separation efficiency and % blue deflect for flaky shaped -15+10mm fraction at varying throughputs

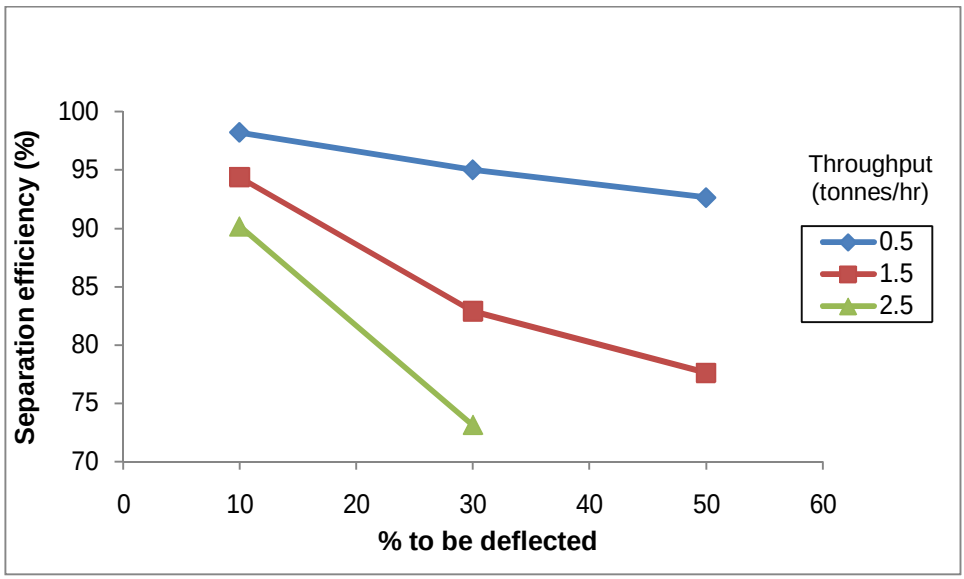

Figure 5.2(e): Relationship between separation efficiency and % blue deflect for -10+6mm fraction at varying throughputs (there was insufficient compressed air to deflect the samples for throughputs up to 2.5tonnes/hr at 50% blue deflect)

Consistently, the separation efficiency lowers with an increase in % blue deflect. There is a significant reduction in separation efficiency at 2.5tonnes/hr when compared to 0.5tonnes/hr. This is because at higher throughputs, there is a higher probability of particle composites containing a blue particle forming due to the higher probability of particles 'touching'. As the automated sorter was programmed to deflect blue particles, the higher the probability of finding a blue particle in a composite, the higher will be the probability of co-deflection.

5.1.3 Co-deflection and throughput

Accept (granite) particles that are inadvertently deflected are referred to as co-deflects. Co-deflection has been one of the reasons suggested for poor separation efficiency. As was shown in sub-section 5.0 when carrying out separation efficiency tests approximately 99.5% of the blue particles were correctly deflected. Figures 5.3(a) to (c) indicate the co-deflection relationships for the granite and the blue granite sample fractions at varying throughput and % blue deflect.

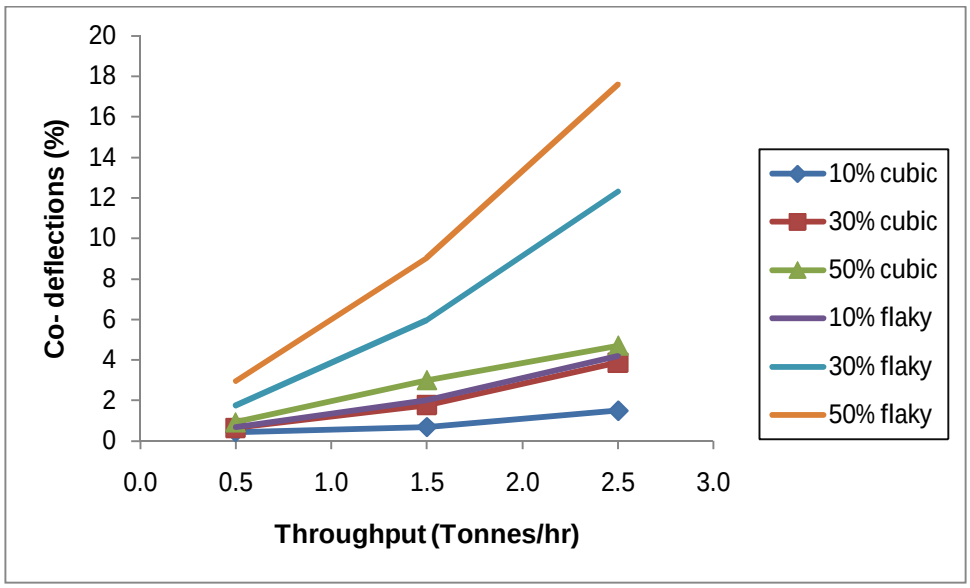

Figure 5.3(a): Co-deflections and throughput relationships for -20+15mm fraction at varying % blue deflect

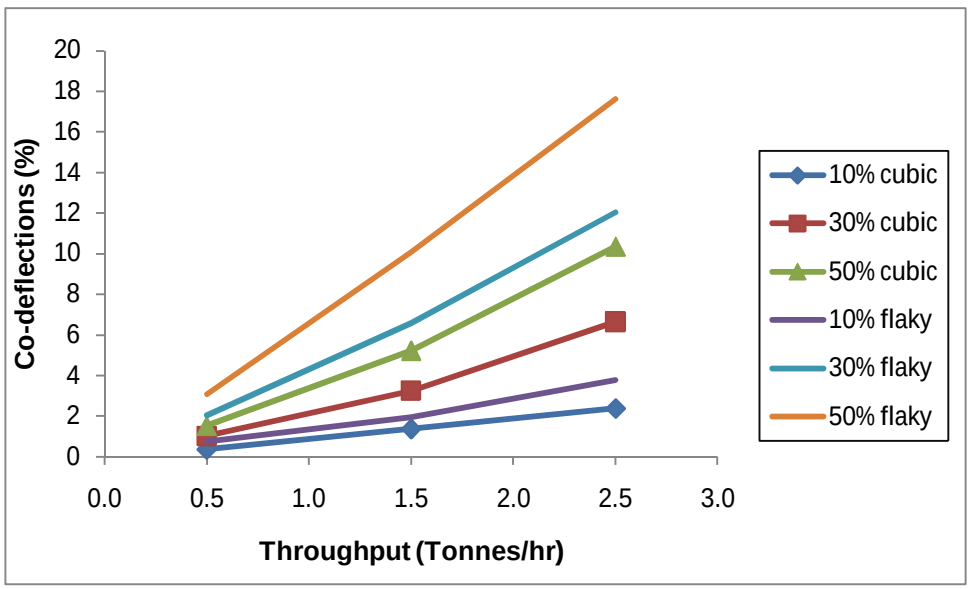

Figure 5.3(b): Co-deflections and throughput relationships for -15+10mm fraction at varying % blue deflect

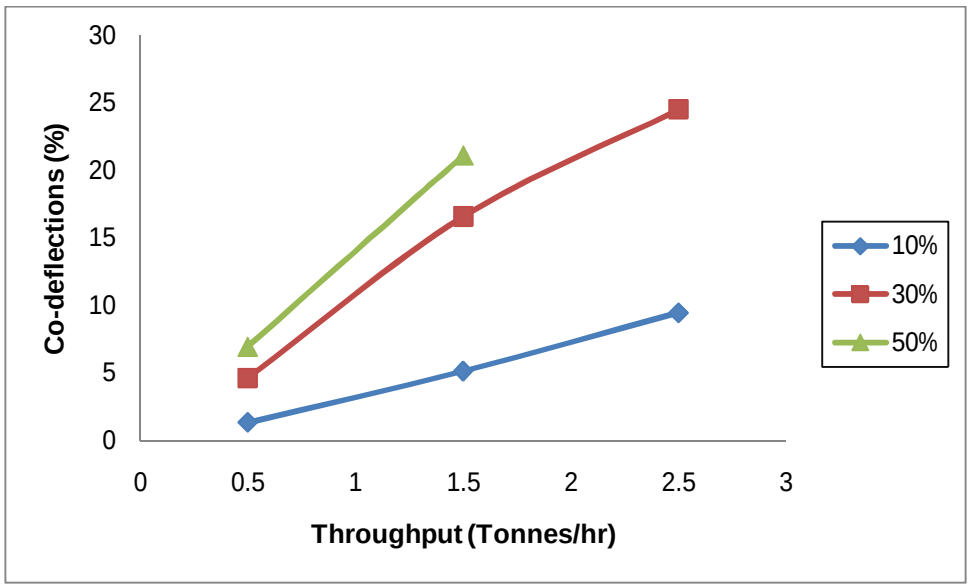

Figure 5.3(c): Co-deflections and throughput relationship for 10+6mm fraction at varying % blue deflect (there was insufficient compressed air to deflect the samples at the 2.5tonnes/hr throughput hence no test results were recorded)

These results indicate that the percentage of co-deflections increases with an increase in throughput and % blue deflect. The graphs presented above generally follow a linear trend through the origin. At the 50% blue deflect there is a greater number of co-deflections than at 10%. The percentage of co-deflections is highest for the -10+6mm size fraction with up to 25% co-deflections at 2.5tonnes/hr (30% deflect). This is because of the larger number of particles on the belt potentially causing more interactions than for the other size fractions.

5.1.4 Shape and co-deflection

One of the research objectives was to study the effect that particle shape had on separation efficiency. To determine the effect of shape the difference in co-deflection obtained for the cubic shaped samples was subtracted from the flaky shaped samples for each sample fraction and at similar throughputs at a 50% blue deflection. The results presented in Figure 5.4 are for the -15+10 and -20+15mm sample fractions as these samples were previously divided into flaky and cubic fractions.

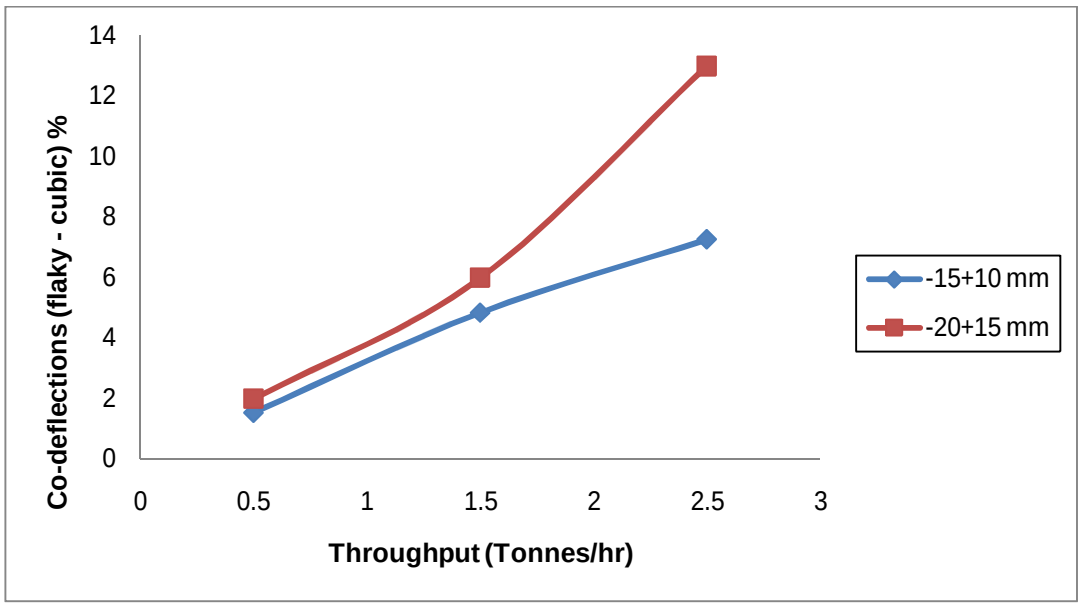

Figure 5.4: Relationship between shapes with throughput for -20+15mm and -15+10mm fraction at 50% blue deflection

These results show that the effect of shape on throughput is more noticeable at higher throughputs especially for the coarse size fraction where the difference is up to 13%. The difference in co-deflections is reduced as the % deflect is reduced although in all cases the co-deflections are higher for the flaky shaped particles.

5.1.5 Summary

For all the sample sizes and shape fractions, the recovery of blue particles averages approximately 99.5% except for those which owing to a lack of sufficient compressed air were lower (as indicated in Table 5.1). These results validate the assumption that identification probabilities approximate to 1. Separation efficiency decreases with an increase in throughput, as indicated in Figures 5.1. The decrease in separation efficiency is exacerbated as the % blue deflection increases to 50%. Thus at a blue deflection of 50% and throughput of 2.5 tonnes/hr, the separation efficiency decreases significantly as shown in Figures 5.2. The finer (-10+6mm) fraction produces a lower separation efficiency when compared to the coarser (-20+15mm) fraction. This could be explained by the probability of particle forming composites which is linked to co-deflections and the number of particle interactions on the belt.

As shown in Figures 5.3, co-deflection increases with an increase in throughput and % blue deflection. The finer sized particles which have a higher number of particles on the belt have a higher probability of composite formation and therefore co-deflection. The difference in co-deflection between flaky and cubic particles is up to 13% for a 50% blue deflection at the coarser size fraction (indicated in Figure 5.4) showing that cubic particles are less affected by co-deflection under similar operating conditions when compared to flaky particles. As separation efficiency is related to co-deflections, if co-deflection is predicted then separation efficiency could be predicted. Results of particle proximity investigations are given in sub-section 5.2.

5.2 SAMPLE PROXIMITY DATA ANALYSIS

The recovery of blue particles was greater than 99% as was shown in section 5.0. Test observations and previous research indicates that the positioning of particles with respect to each other (forming composites) is key to separation efficiency because when particle composites form there is an increased possibility of co-deflection. Co-deflections can be linked to the quantity of particles on the belt (belt loading) as the particles are transported to the identification point. Investigations were undertaken to determine the relationships between composite formation, the belt loading and separation efficiency.

5.2.1 Belt loading and throughput

The calculation for belt loading had been discussed earlier in Chapter 4, sub-section 4.2.7. The results presented use belt loading values calculated with the 'particle size' method. The relationships between belt loading and throughput at various shapes and sizes are indicated in Figures 5.5 (a) and (b).

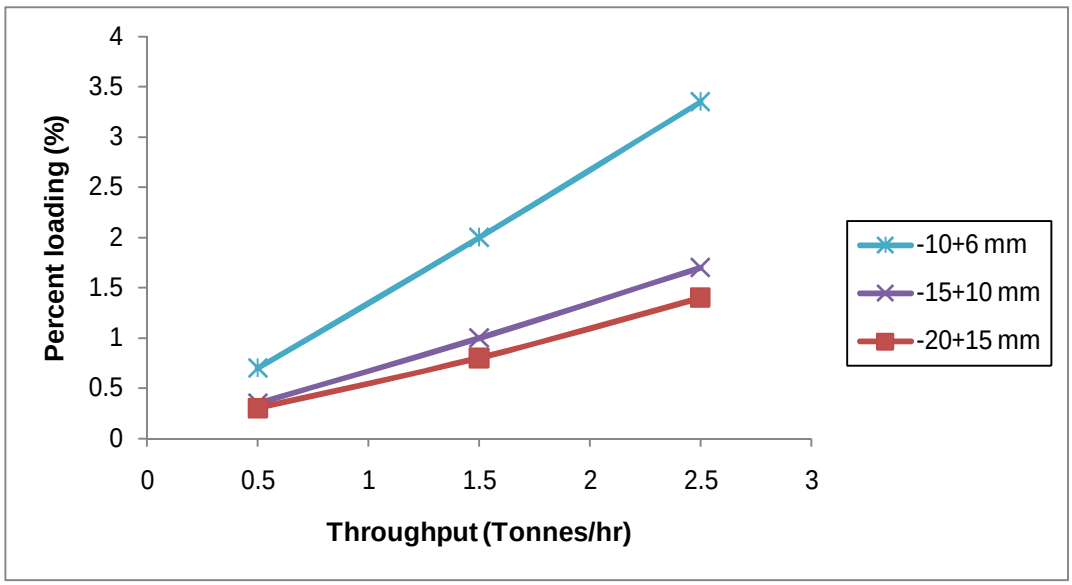

Figure 5.5(a): Throughput and belt loading relationships for the cubic shaped fractions

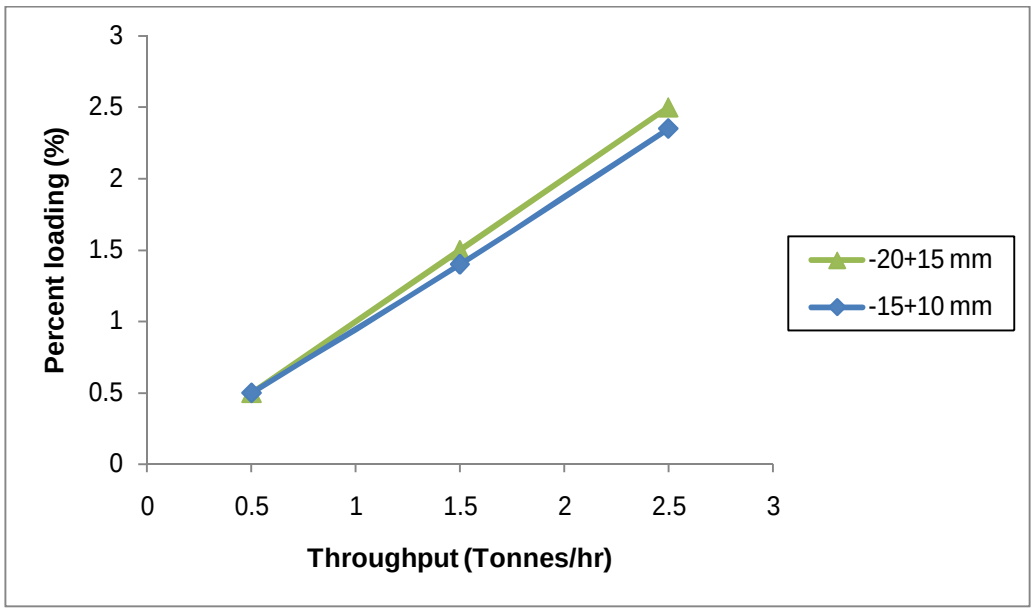

Figure 5.5(b): Throughput and belt loading relationships for the flaky fraction

The results show that belt loading ranged between 0.5 and 3.35%, with the highest belt loading recorded for the -10+6mm fraction. The difference in belt loading between size fractions is larger for the -10+6mm and -15+10mm fraction than between the -15+10 and -20+15mm sizes. A flaky shaped particle occupies a larger surface area due to the reduced particle thickness and is therefore more likely to form composites than a cubic shaped particle at a specific throughput.

5.2.2 Belt loading and co-deflection

Belt loading data previously determined were compared against co-deflections for all the samples. Figure 5.6 indicate the belt loading and co-deflection occurrence relationships.

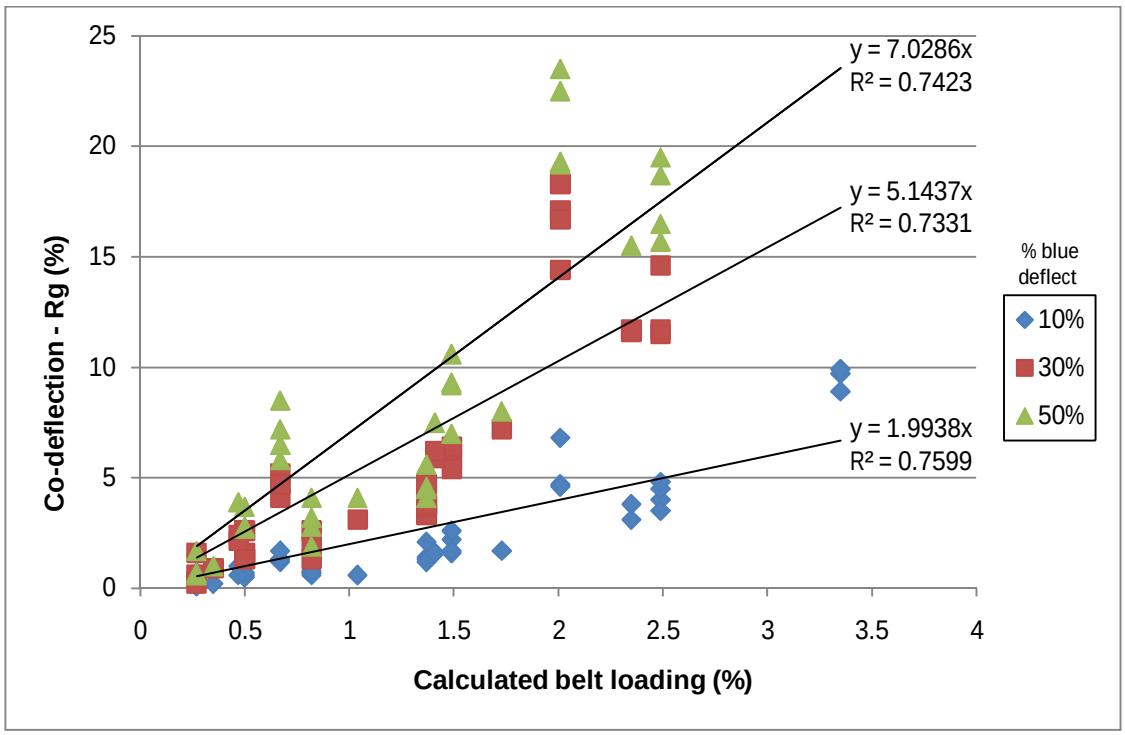

Figure 5.6: Co-deflection and belt loading relationships for all samples at varying % blue deflect

These results indicate that there is a linear relationship between belt loading and co-deflection formation. As belt loading (a function of sample size shape and throughput) increases so does the percentage of co-deflections. At higher % blue deflect there is a higher number of co-deflections.

5.2.3 Composites

Figure 5.7 shows the groupings that are referred to as composites in this study. It is possible that particles in close contact are also possibly seen as a 'composite'.

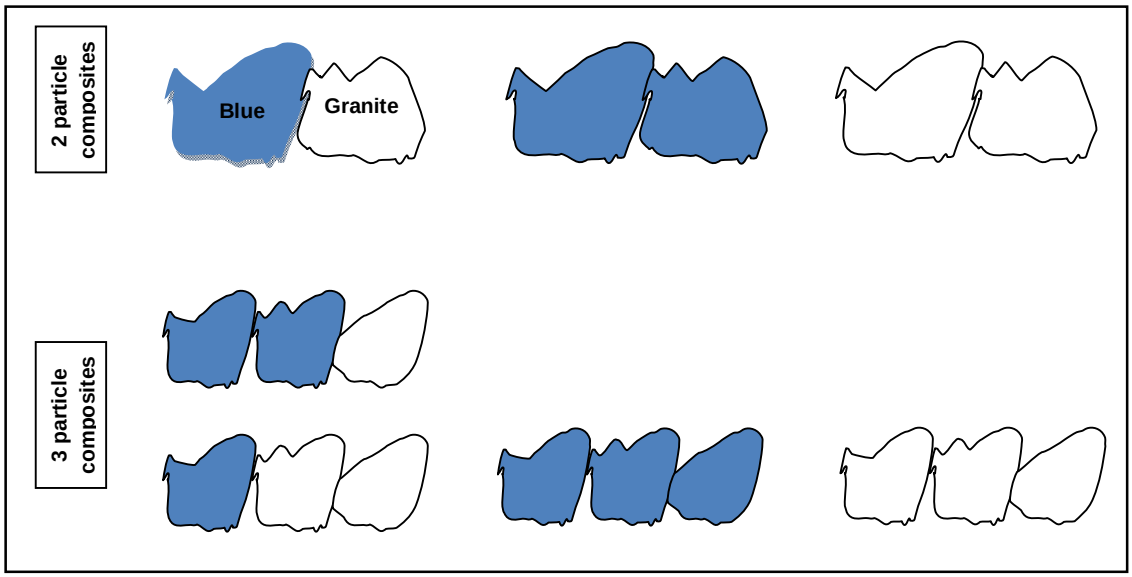

Figure 5.7: Particle groupings referred to as composites (close contact also possibly seen as 'composite')

Figures 5.8(a) to (e) indicates the percent composites calculated for all the sample fractions considered in this research. These were calculated using the methodology previously discussed in Chapter 4, sub-section 4.2.4.

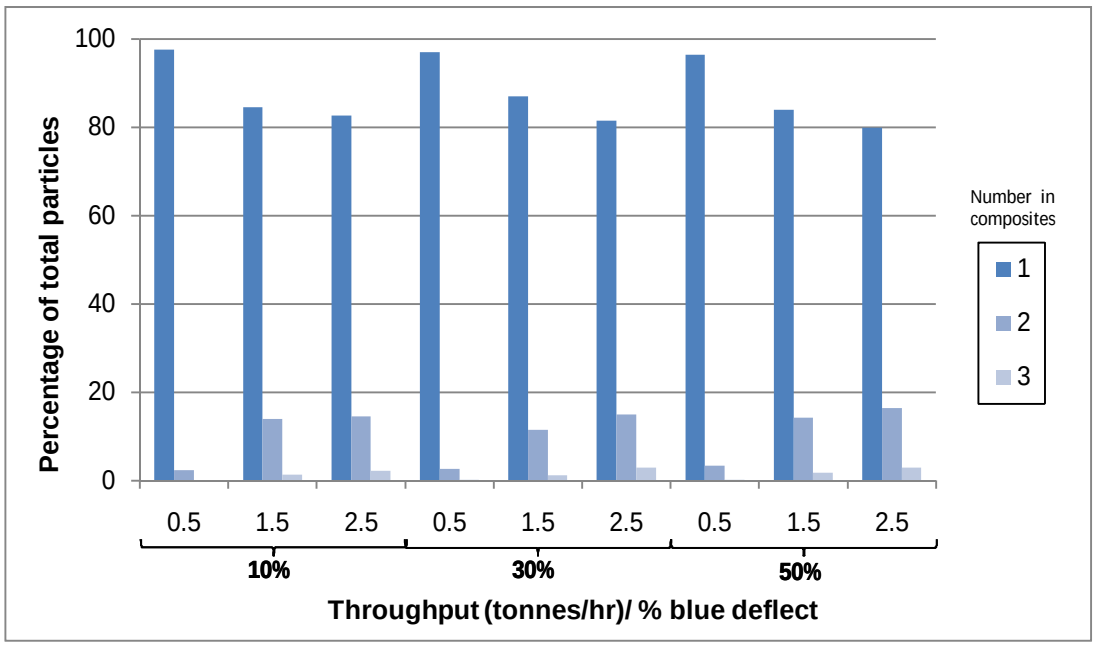

Figure 5.8(a): Calculated particles in composites for flaky shaped -20+15mm fraction

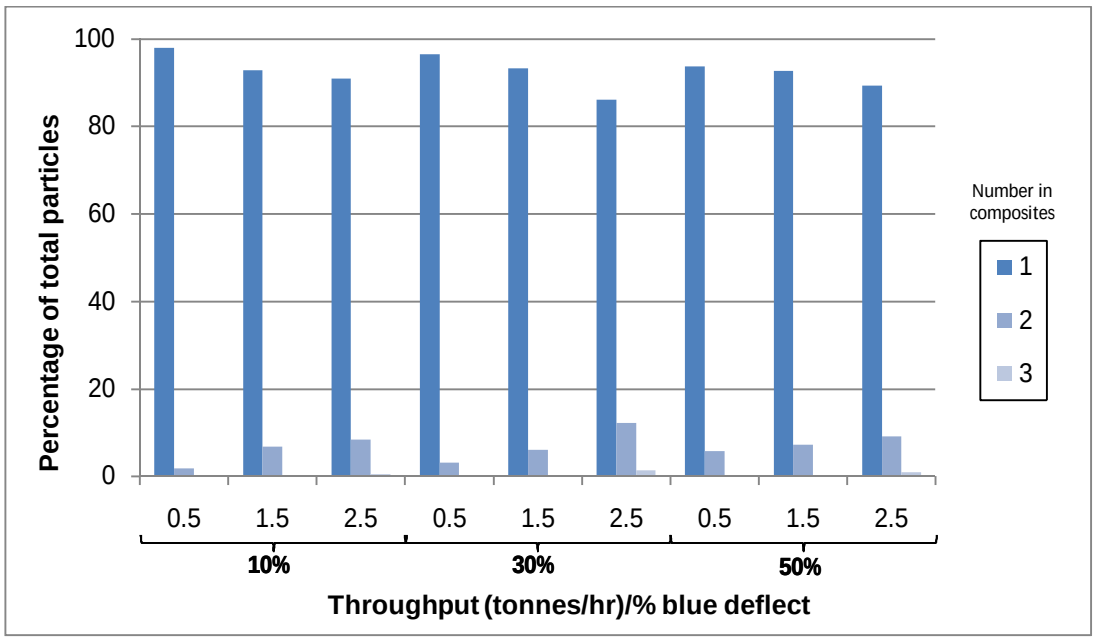

Figure 5.8(b): Calculated particles in composites for cubic shaped -20+15mm fraction

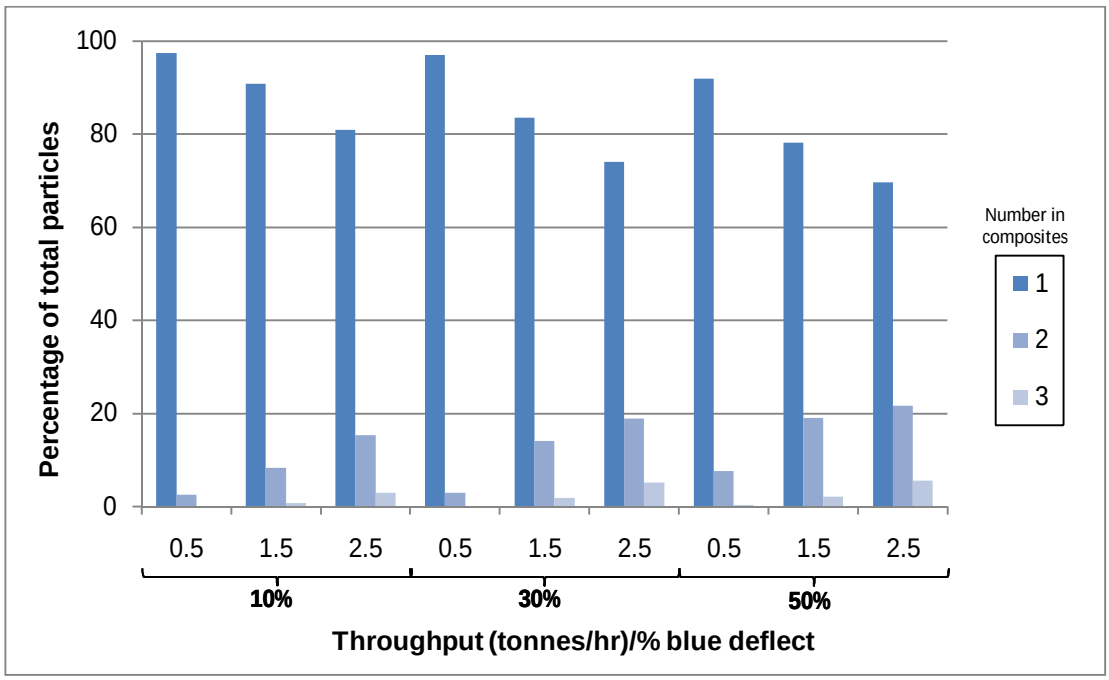

Figure 5.8(c): Calculated particles in composites for flaky shaped -15+10mm fraction

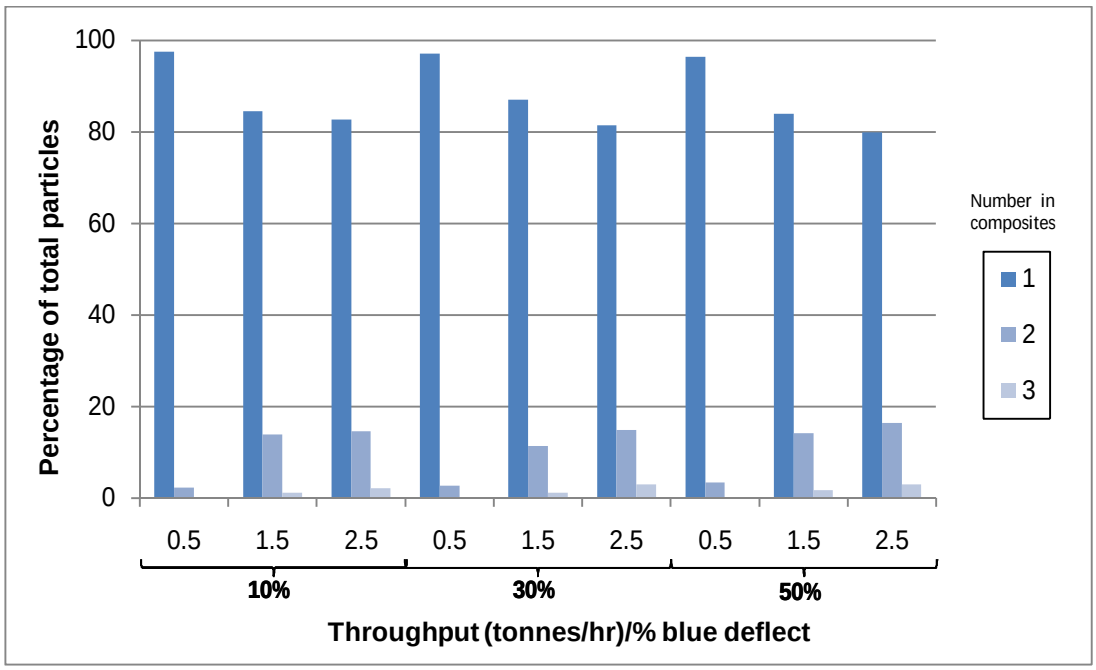

Figure 5.8(d): Calculated particles in composites for cubic shaped -15+10mm fraction

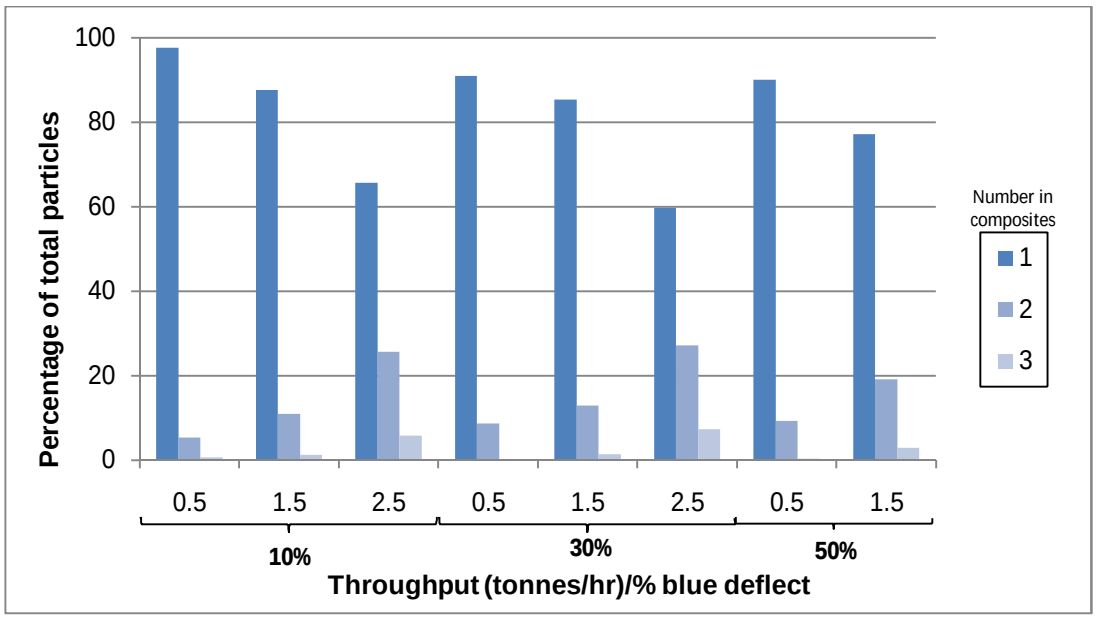

Figure 5.8(e): Calculated particles in composites for -10+6mm fraction

These results indicate, as expected, that more composites form with an increase in throughput. This data is summarised in Table 5.3.

Table 5.3: Calculated composites data for all size fractions

CALCULATED % COMPOSITES (100 - % single particles) at specified Throughput (tonnes/hr)									
Size fraction (mm) and shape	***0.5***	***1.5***	***2.5***	***0.5***	***1.5***	***2.5***	***0.5***	***1.5***	***2.5***
	10% Blue deflect			**30% Blue deflect**			**50% Blue deflect**		
-20+15, cubic	2	7	9	4	7	14	6	7	11
-20+15, flaky	2	15	17	3	13	19	4	16	20
-15+10, cubic	3	9	18	7	13	20	13	17	23
-15+10, flaky	3	9	19	3	16	26	8	22	30
-10+6	2	12	34	9	15	40	10	23	-

There was insufficient compressed air to deflect the samples at the 2.5tonnes/hr throughput 50% blue deflection hence no test results were recorded)

5.2.4 Composites and co-deflection

Using the composite data discussed in sub-section 5.2.3, the correlation between composites formation and the percentage of co-deflected particles recorded were studied. The relationship between composite formation and co-deflection for all the size fractions are shown in Figures 5.9 (a) to (e). The linear best fit graph was forced through zero in all cases.

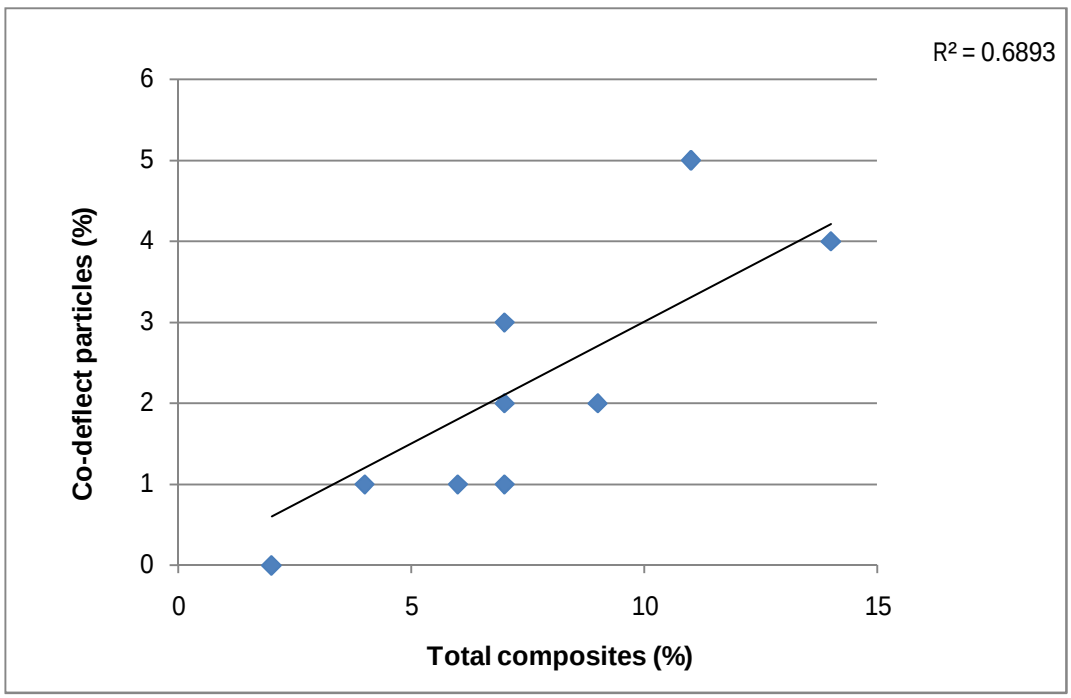

Figure 5.9(a): Composites and co-deflection relationship for cubic shaped -20+15mm fraction

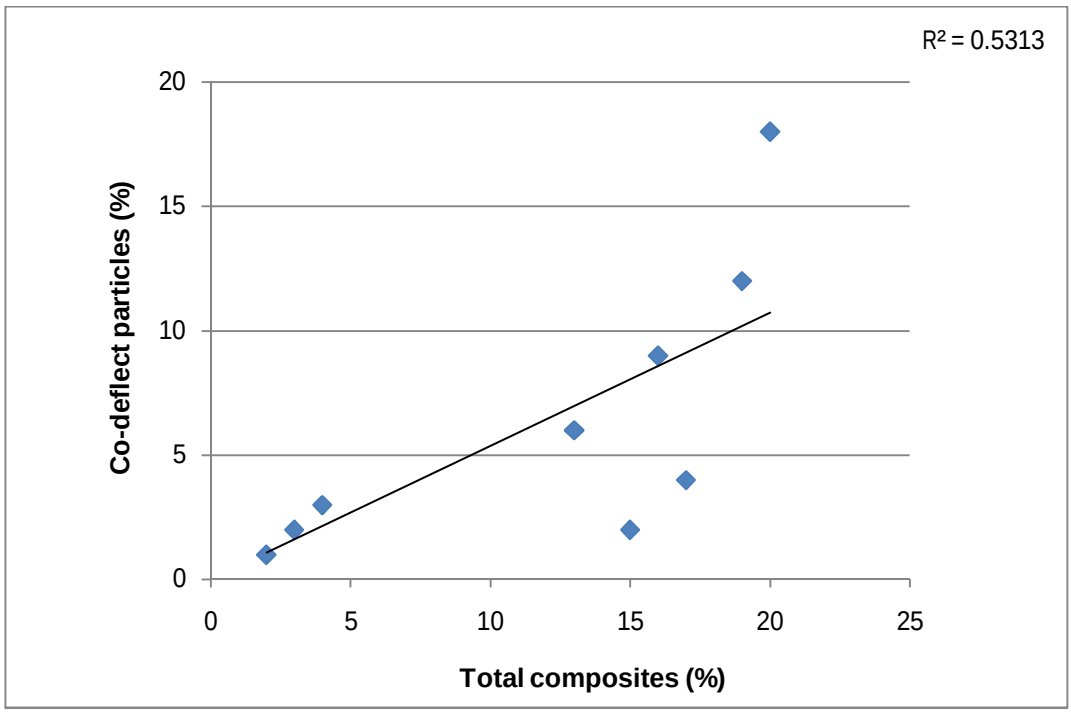

Figure 5.9(b): Composites and co-deflection relationship for flaky shaped -20+15mm fraction

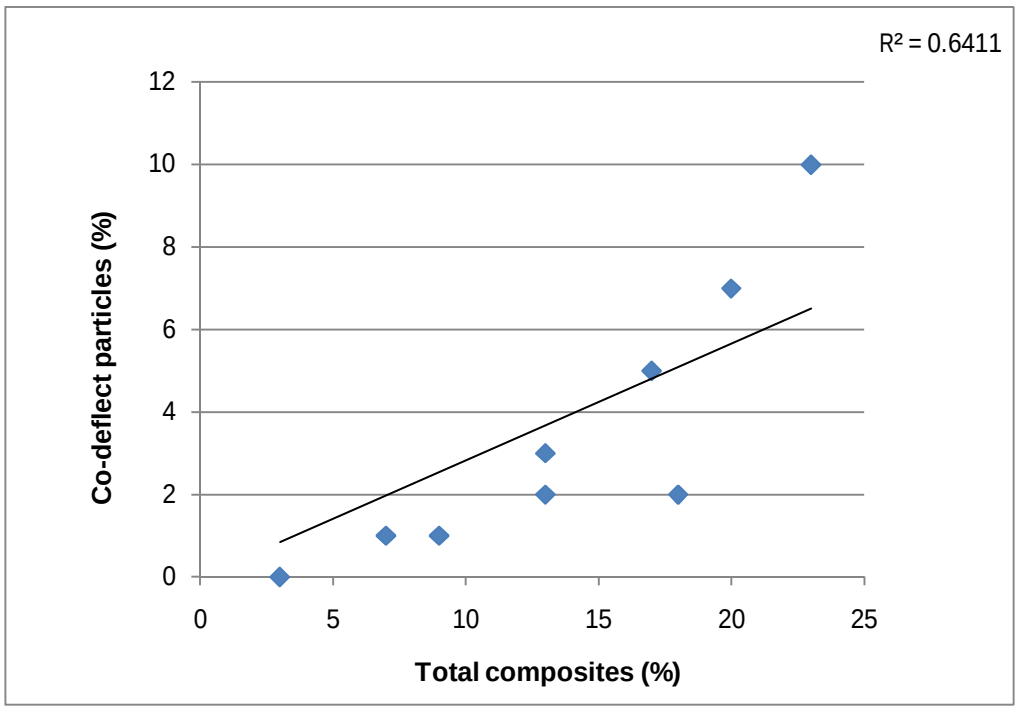

Figure 5.9(c): Composites and co-deflection relationship for cubic shaped -15+10mm fraction

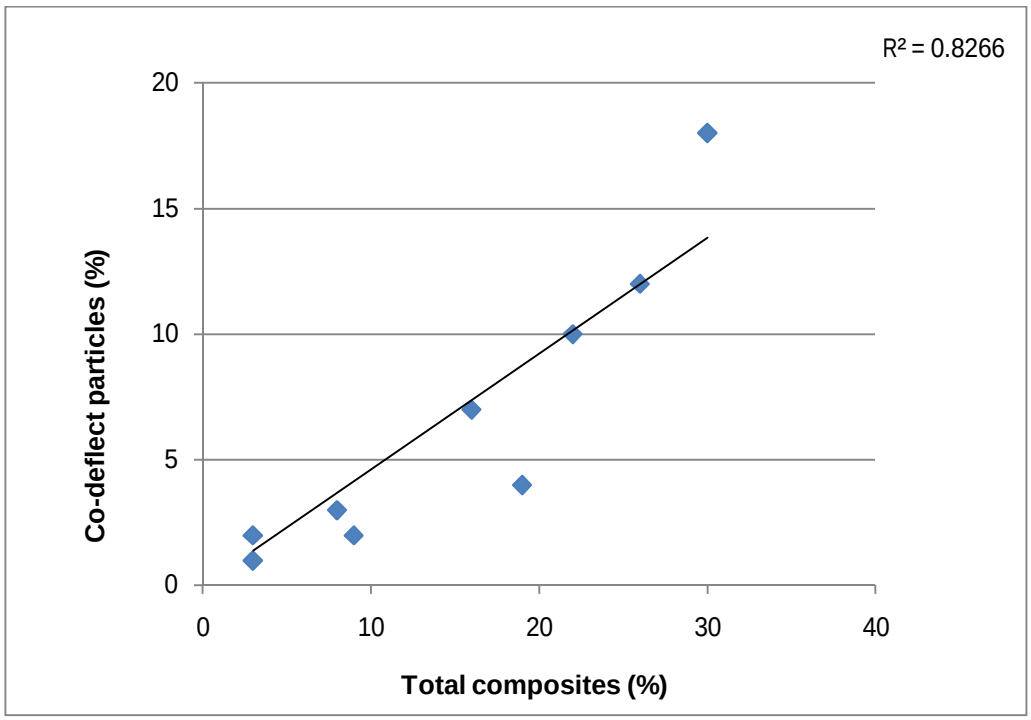

Figure 5.9(d): Composites and co-deflection relationship for flaky shaped -15+10mm fraction

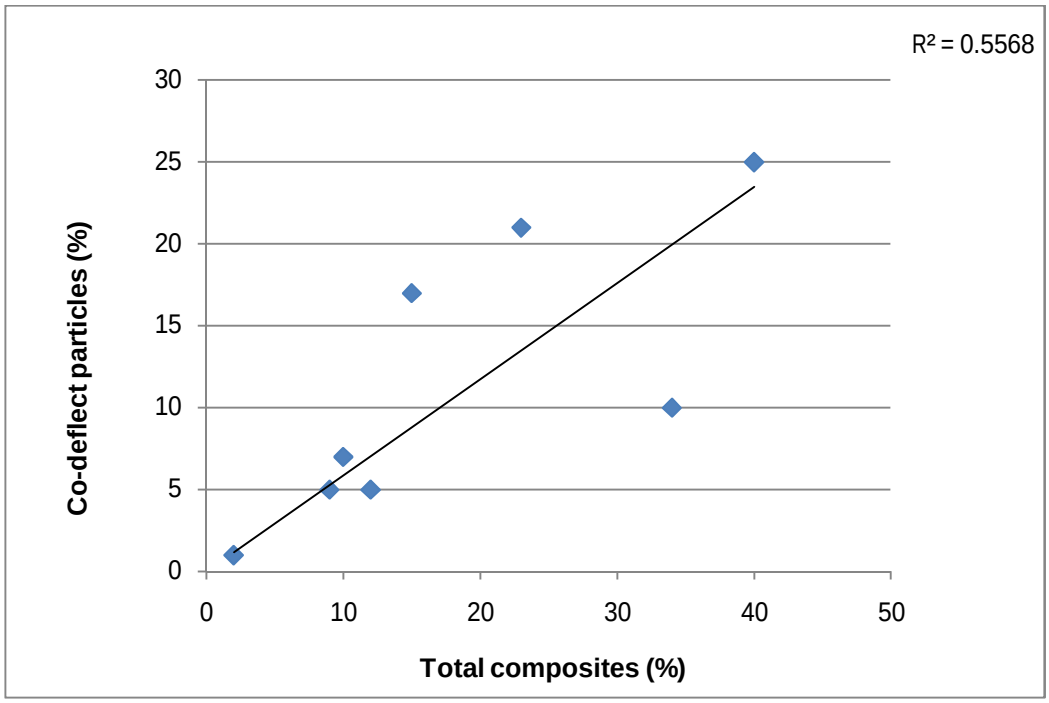

Figure 5.9(e): Composites and co-deflection relationship for -10+6mm fraction

These results indicate that there is a reasonable link between composite formation and co-deflections. The higher the amount of composites formed the higher the co-deflections that occur. Since co-deflections relate to

separation efficiency, it follows that factors that increase composite formation will result in lower separation efficiency.

5.2.5 Monte Carlo analysis of composites

To investigate the number of composites likely to form at varying conditions (sample size, shape, throughput and % blue deflect), Monte Carlo analysis was applied.

Methodology: A means to calculate the area of the (conveyor) belt loading was investigated previously discussed in section 4.2.7. After determining this belt area, Monte Carlo analysis was undertaken using *Excel* Microsoft software to simulate particle distribution over the area of the belt covered by the samples at similar experimental conditions.

For these tests, a column by row area was utilised to represent the investigated area of the belt. The number of columns was determined using the average diameter of the particle dividing this value by the width of the belt. Hence the three size fractions produce 32, 44 and 69 columns, representing the -20+15, -15+10 and -10+6 fraction respectively. The row area represents the typical length of travel of the belt per test batch. A belt travelling at $3ms^{-1}$ will travel approximately 2400 to 3000cm in 8 to 10s which is the typical time taken to run a test batch. Hence the areas considered are 32 columns by 2500 rows, 44 columns by 2500 rows and 69 columns by 2500 rows representing the -20+15, -15+10 and -10+6 fraction respectively.

As was previously shown in Figure 4.14, the belt distribution is such that the middle 30cm of the belt is covered by approximately 75 to 83% of the particles. To replicate this, the belt width was divided into equal zones then each zone was given a weighted probability of particle occurrence within the zone an example of which is shown in Table 5.4.

Table 5.4: Weighted distribution of belt area for cubic shaped -15+10mm fraction at 2.5tonnes/hr, 50% blue deflect

Zone	Sort width	2000 scale	Cum. Dist.	Within zone	Zone (%)	Zone adj. (%)	Fraction Accept	Fraction deflect
1	12.5	45.45455	0.008508	0.008508	0.850796	0.6483603	0.32418013	0.32418
2	25	90.90909	0.011521	0.003013	0.301335	0.2296365	0.11481824	0.114818
3	37.5	136.3636	0.015422	0.0039	0.390025	0.2972235	0.14861176	0.148612
4	50	181.8182	0.020405	0.004983	0.498348	0.3797724	0.18988619	0.189886
5	62.5	227.2727	0.026691	0.006286	0.628594	0.4790286	0.2395143	0.239514
6	75	272.7273	0.034518	0.007827	0.78272	0.596482	0.29824102	0.298241
7	87.5	318.1818	0.04414	0.009621	0.962144	0.7332147	0.36660737	0.366607
8	100	363.6364	0.055815	0.011675	1.16754	0.8897395	0.44486976	0.44487
9	112.5	409.0909	0.069801	0.013986	1.398625	1.0658411	0.53292055	0.532921
10	125	454.5455	0.086341	0.01654	1.653975	1.2604334	0.63021672	0.630217
11	137.5	500	0.10565	0.019309	1.930875	1.4714491	0.73572457	0.735725
12	150	545.4545	0.127902	0.022252	2.225243	1.695776	0.84788799	0.847888
13	162.5	590.9091	0.153218	0.025316	2.53162	1.9292548	0.9646274	0.964627
14	175	636.3636	0.181651	0.028433	2.843266	2.1667489	1.08337445	1.083374
15	187.5	681.8182	0.213175	0.031524	3.15235	2.4022902	1.20114509	1.201145
16	200	727.2727	0.247677	0.034502	3.450239	2.6293006	1.31465029	1.31465
17	212.5	772.7273	0.284956	0.037279	3.727879	2.84088	1.42044002	1.42044
18	225	818.1818	0.324718	0.039762	3.976238	3.0301452	1.51507262	1.515073
19	237.5	863.6364	0.366586	0.041868	4.186787	3.1905965	1.59529824	1.595298
20	250	909.0909	0.410106	0.04352	4.351983	3.3164863	1.65824316	1.658243
21	262.5	954.5455	0.454763	0.044657	4.465719	3.4031605	1.70158024	1.70158
22	275	1000	0.5	0.045237	4.523697	3.4473433	1.72367167	1.723672
23	287.5	1045.455	0.545237	0.045237	4.523697	3.4473433	1.72367167	1.723672
24	300	1090.909	0.589894	0.044657	4.465719	3.4031605	1.70158024	1.70158
25	312.5	1136.364	0.633414	0.04352	4.351983	3.3164863	1.65824316	1.658243
26	325	1181.818	0.675282	0.041868	4.186787	3.1905965	1.59529824	1.595298
27	337.5	1227.273	0.715044	0.039762	3.976238	3.0301452	1.51507262	1.515073
28	350	1272.727	0.752323	0.037279	3.727879	2.84088	1.42044002	1.42044
29	362.5	1318.182	0.786825	0.034502	3.450239	2.6293006	1.31465029	1.31465
30	375	1363.636	0.818349	0.031524	3.15235	2.4022902	1.20114509	1.201145
31	387.5	1409.091	0.846782	0.028433	2.843266	2.1667489	1.08337445	1.083374
32	400	1454.545	0.872098	0.025316	2.53162	1.9292548	0.9646274	0.964627
33	412.5	1500	0.89435	0.022252	2.225243	1.695776	0.84788799	0.847888
34	425	1545.455	0.913659	0.019309	1.930875	1.4714491	0.73572457	0.735725
35	437.5	1590.909	0.930199	0.01654	1.653975	1.2604334	0.63021672	0.630217
36	450	1636.364	0.944185	0.013986	1.398625	1.0658411	0.53292055	0.532921
37	462.5	1681.818	0.95586	0.011675	1.16754	0.8897395	0.44486976	0.44487
38	475	1727.273	0.965482	0.009621	0.962144	0.7332147	0.36660737	0.366607
39	487.5	1772.727	0.973309	0.007827	0.78272	0.596482	0.29824102	0.298241
40	500	1818.182	0.979595	0.006286	0.628594	0.4790286	0.2395143	0.239514
41	512.5	1863.636	0.984578	0.004983	0.498348	0.3797724	0.18988619	0.189886
42	525	1909.091	0.988479	0.0039	0.390025	0.2972235	0.14861176	0.148612
43	537.5	1954.545	0.991492	0.003013	0.301335	0.2296365	0.11481824	0.114818
44	550	2000	0.99379	0.008508	0.850796	0.6483603	0.32418013	0.32418
				Sum	100	76.206327	38.1031636	38.10316

The ‘zone’ represents each equal zone which the belt has been sub-divided into. The ‘sort width’ is the width of each zone, determined by dividing the

belt width by the number of zones calculated. This zone width is then converted from the 550mm width to a '2000 scale' width to correspond to the 2000 pixel width as recorded by the sorter (see Figure 3.18). Assuming a 'normal' belt distribution then the belt width is 2000 pixels, mean is 1000 pixels and standard deviation of 400. Based on these assumptions the cumulative distribution (Cum. Dist.) for each zone is calculated. The number of particles within this zone (within zone) is then calculated and adjusted for (zone adj) by multiplying the product with the calculated belt area (0.76% for this example). The 'zone adj' data is then split into the fractions to be accepted (fraction accept) and fraction to be deflected (fraction deflect) based on the % blue deflect. This process is repeated for each of the zones.

With each zone weighting completed a series of random numbers was generated using the random number generation function of the Microsoft *Excel*. The process for determining 'accept' and 'reject' particles are described in the flowchart shown in Figure 5.10.

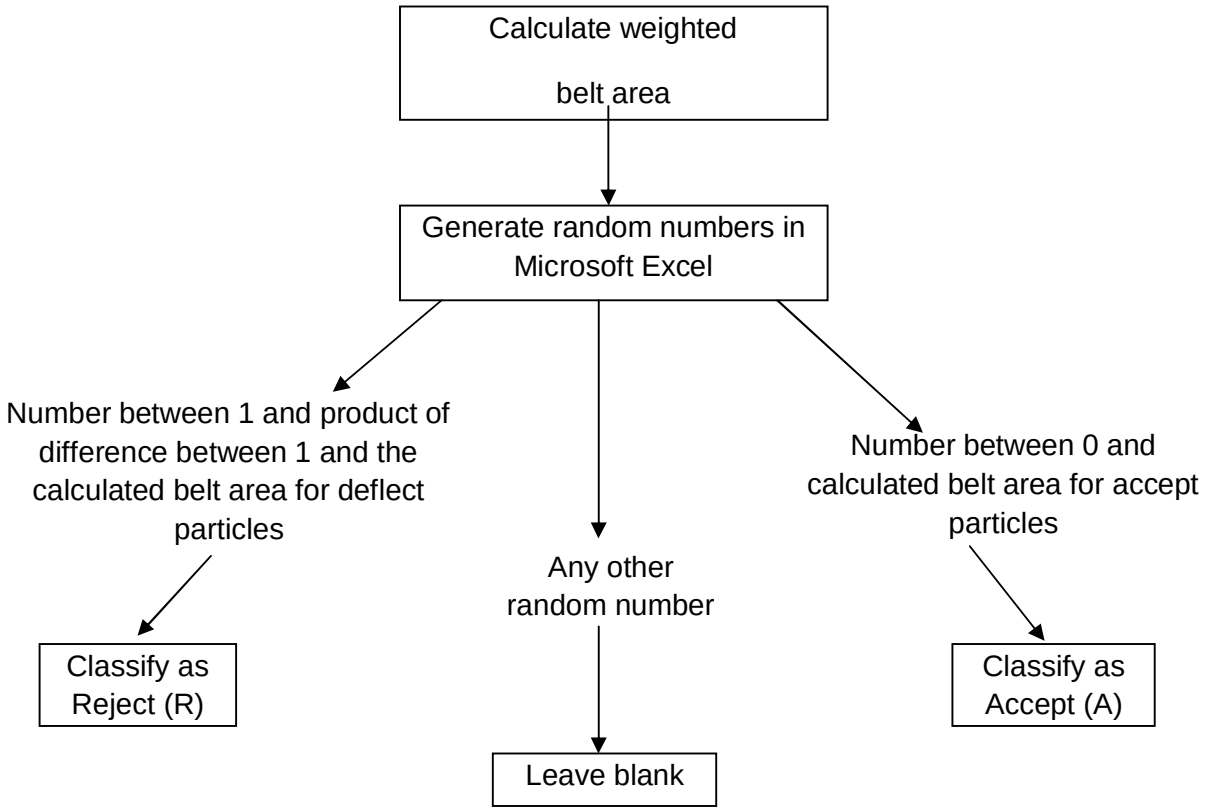

Figure 5.10: Flow chart showing the classification procedure for Monte Carlo analysis

In each cell, if the random number falls between 0 and the calculated weighted 'accept' belt area covered by a particle, such a cell is taken as an accept particle. If the random number falls between 1 and the product of 1 minus the calculated weighted 'reject' belt area, it is taken as a reject particle. The rest of the cells are considered to be without particles and is left blank.

If the weighted accept belt area is 0.87% (0.0087) and the weighted reject belt area is 0.87% (0.0087), then a random number would be considered an accept particle if that number value ranged between 0 and 0.0087, while a reject particle would range between 0.9913 and 1.

For the occupied cells comparison between the classified positions were utilised to determine the single touching particles. From the particles classification positions descriptions such as accept (A) or reject (R) are

determined (see Table 5.5). Figure 5.11 indicates the particle position utilised for the classifications.

Table 5.5: Sample groupings

Position no.	Symbol	Description
1	AA	An accept particle positioned to the right of another accept particle
2	AR	An accept particle positioned to the right of a reject particle
3	RR	A reject particle positioned to the right of another reject particle
4	RA	A reject particle positioned to the right of an accept particle
5	A/A	An accept particle positioned on top of another accept particle
6	A/R	An accept particle positioned on top of a reject particle
7	R/A	A reject particle positioned on top of an accept particle
8	R/R	A reject particle positioned on top of another reject particle
9	AdiagA	An accept particle positioned diagonally on top another accept particle
10	AdiagR	A reject particle positioned diagonally on top of an accept particle
11	RdiagA	An accept particle positioned diagonally on top a reject particle
12	RdiagR	A reject particle positioned diagonally on top another reject particle
13	AdiagA	A reject particle positioned diagonally beneath another accept particle
14	AdiagR	A reject particle positioned diagonally beneath an accept particle
15	RdiagA	An accept particle positioned diagonally beneath a reject particle
16	RdiagR	A reject particle positioned diagonally beneath another reject particle

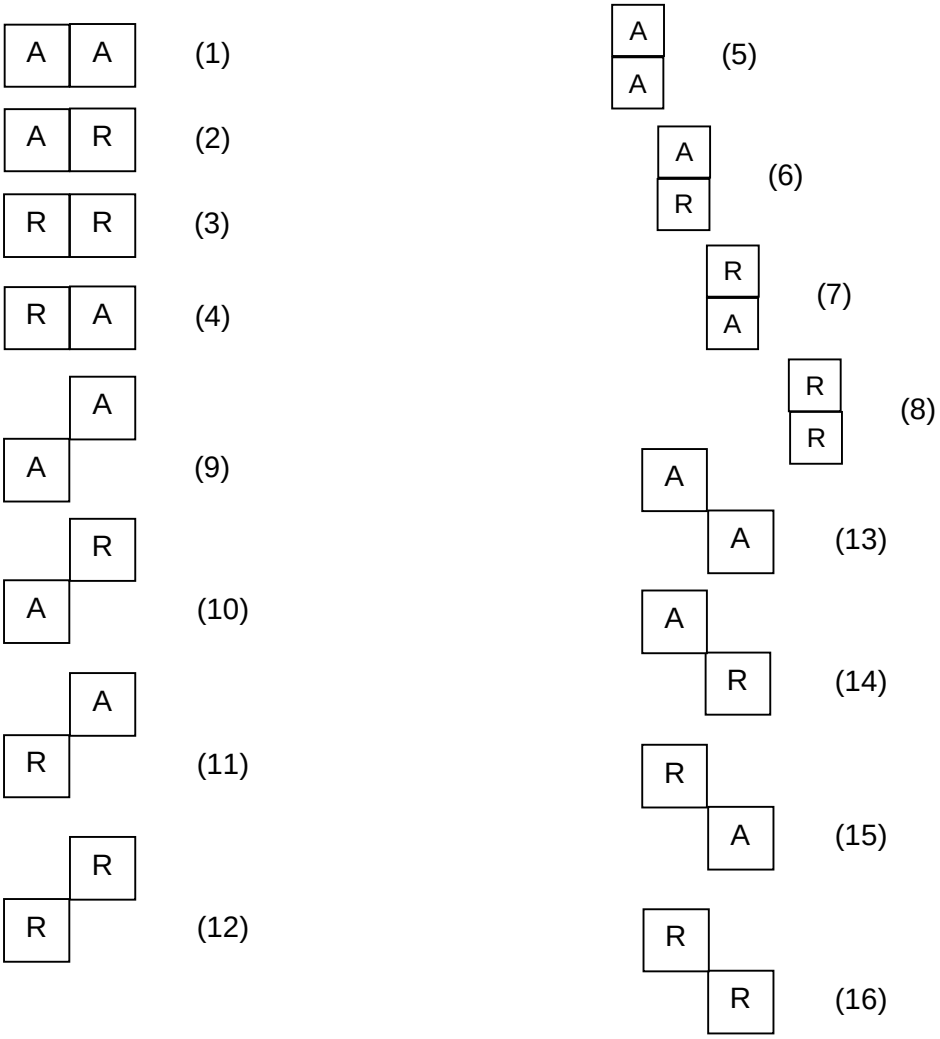

Figure 5.11: Particle positioning for Monte Carlo analysis

A small section of the particle positioning obtained for the -10+6mm fraction is shown in Figure 5.12 where 'A' signifies an accept particle and 'R' reject.

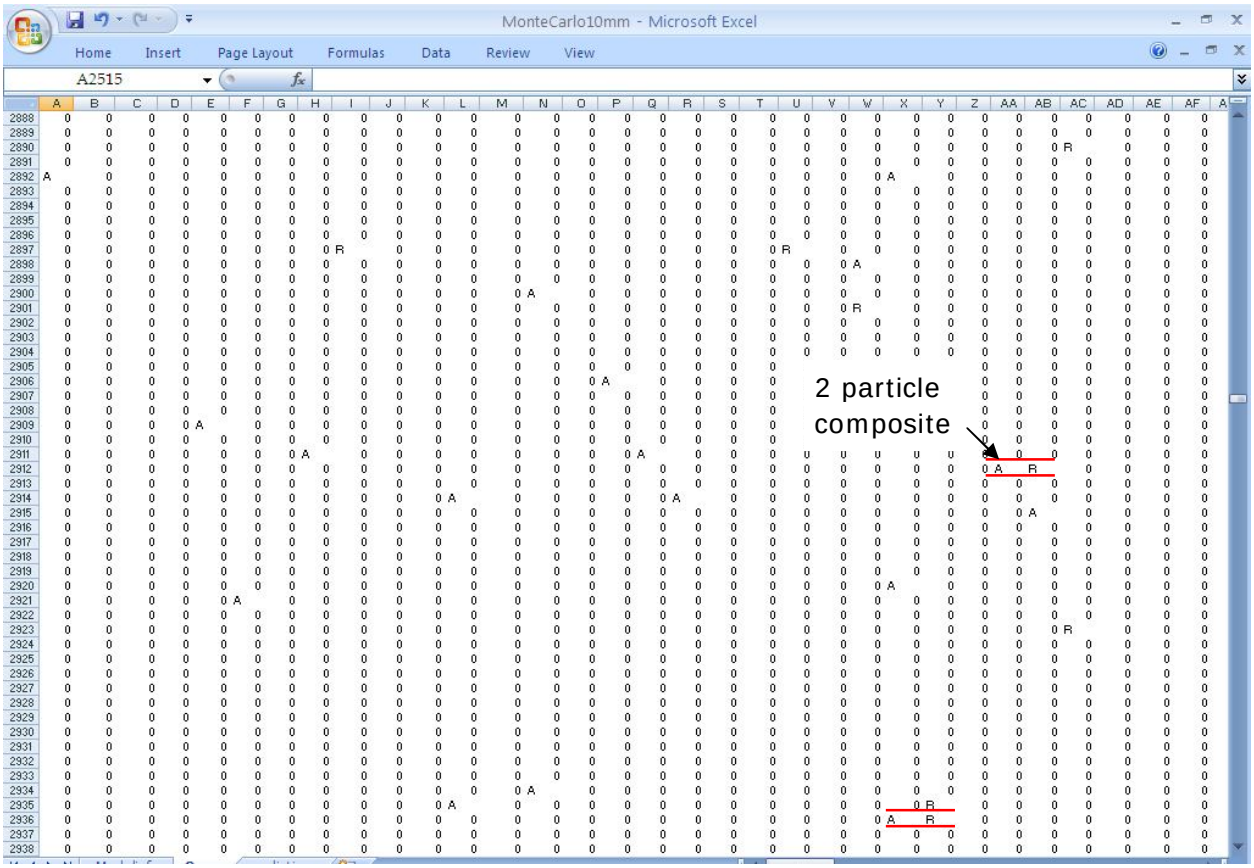

Figure 5.12: Picture of Monte Carlo analysis of belt loading for -10+6mm fraction 30% blue deflect, at 2.5 tonnes/hr

With these positions determined, the total number of occurrences of each position classification is summed and utilised to calculate the number of touching single particles including an 'R' particle (ΔS) as follows:

$$\Delta S\ (\%) = \frac{\text{Sum of particles positioned at numbers } (2,4,6,7,10,11,14,15)}{\text{Total number of particles}} \text{ X } 100$$

Figures 5.13 (a) to (c) indicates the comparison between the actual single particles obtained utilising the image processing analyser data with single touching particles estimated utilising Monte Carlo analysis for the coarse size fraction only.

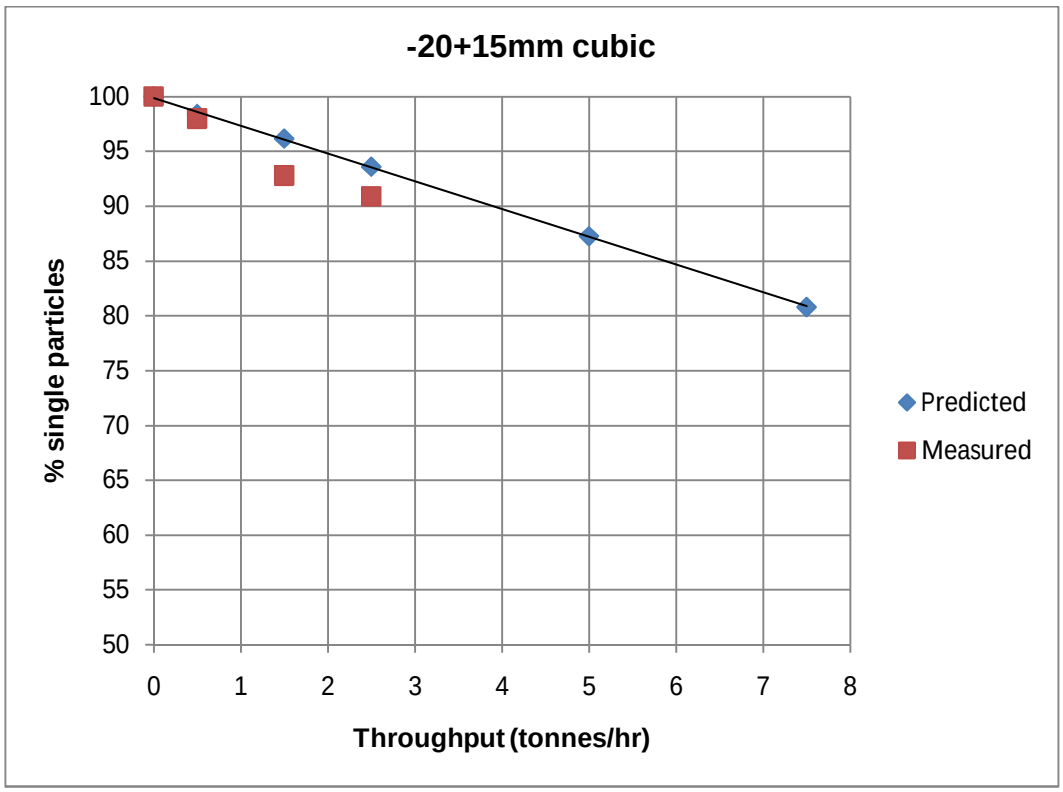

Figure 5.13(a): Comparison of Monte Carlo analysis determination with actual single touching sample particles for cubic shaped -20+15mm fraction

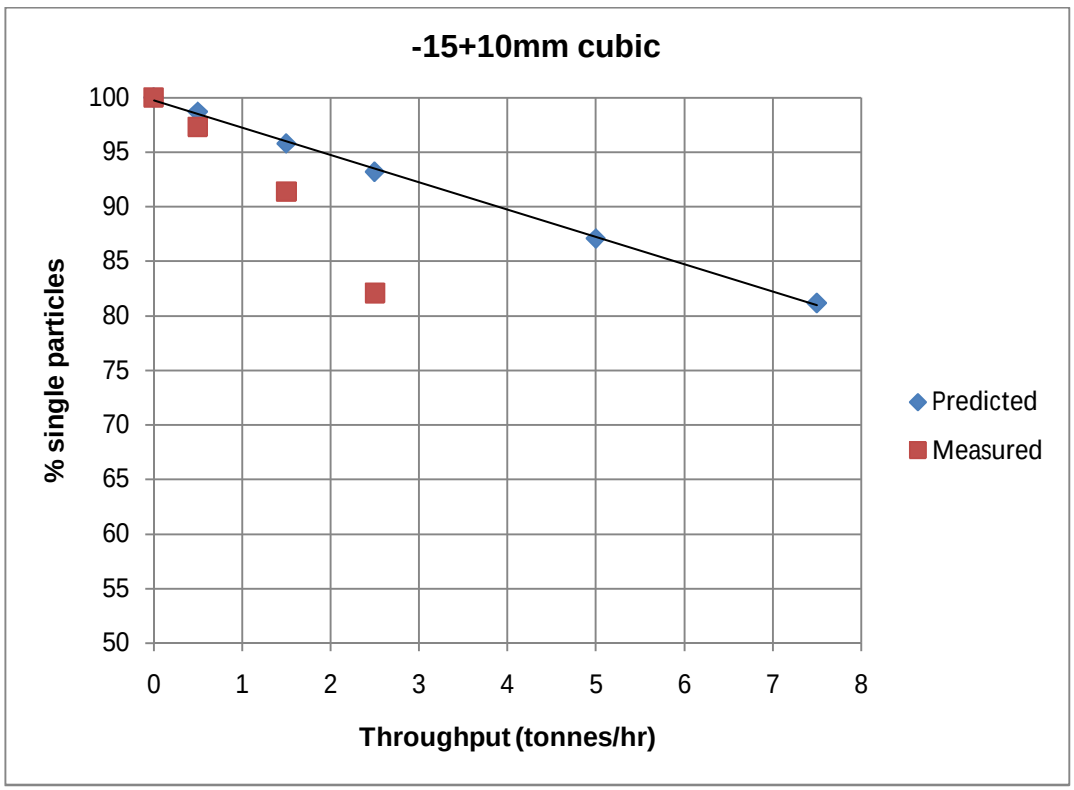

Figure 5.13(b): Comparison of Monte Carlo analysis determination with actual single touching sample particles for cubic shaped -15+10mm fraction

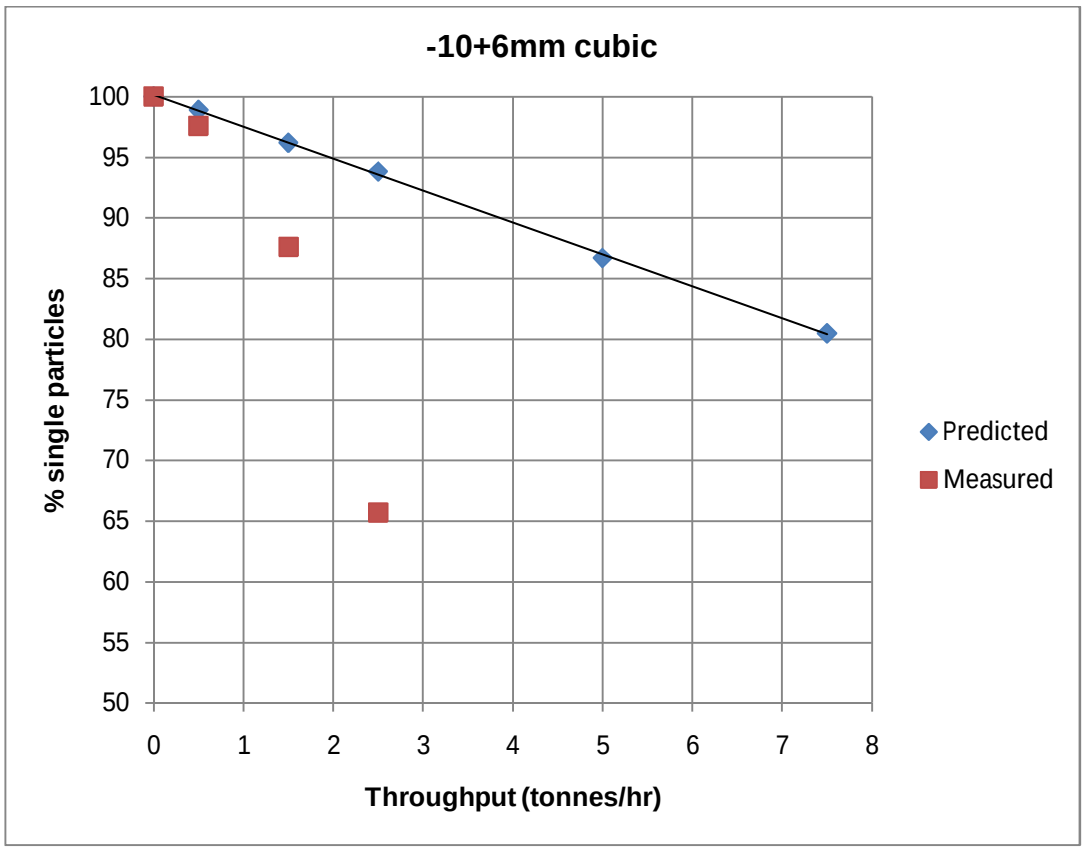

Figure 5.13(c): Comparison of Monte Carlo analysis determination with actual single touching sample particles for -10+6mm fraction

The comparison between actual single particles and those obtained utilising Monte Carlo simulation indicates for all three size fractions that the Monte Carlo simulation predicts a much smaller percentage of multiple particles compared to analysis of data collected from the automated sorter. This result may be due to the fact that the actual distribution may not be random. Another reason can be linked with the chute width being smaller than the belt width leading to possible channelling of the particles.

5.2.6 Particle zone of influence

To determine the area of influence that each valve nozzle had on sample deflection and drawing inference on the sensitivity of each valve tests discussed in Chapter 4, sub-section 4.2.6 were undertaken. It should be noted that particles that may not be touching may appear as a 'composite'. Due to the precision of the air ejection system a particle that appears separate may also be affected by an air blast of another particle.

Tables 5.6(a) to (c) indicates the results of the tests for finer (-10+6mm), intermediate (cubic shaped -15+10mm) and coarser (flaky shaped

-20+15mm) size fractions. The position numbers are shown in Figure 5.14.

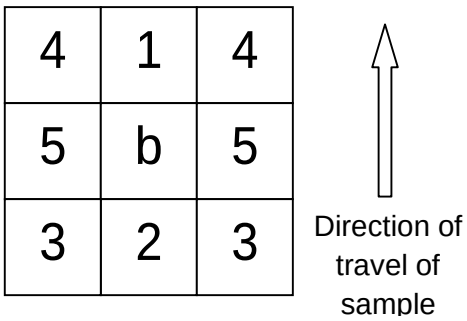

Figure 5.14: Positions of the blue and granite particles utilised to investigate zone of influence of sample composites

Table 5.6(a): Particle positions for the -10+6mm fractions

	Fraction of co-deflected granite at specified distance from blue particle				
Position number	Close together	2mm	4mm	6mm	10mm
1	0.9	0.9	0.7	0.4	0.1
2	0.9	0.3	0.1	0.0	-
3	0.5	0.0	-	-	-
4	0.8	0.3	0.2	0.0	-
5	0.7	0.2	0.1	0.0	-

5.6(b): Particle positions for the -15+10mm fractions

	Fraction of co-deflected granite at specified distance from blue particle				
Position number	Close together	2mm	4mm	6mm	10mm
1	1.0	0.9	0.7	0.2	0.0
2	0.9	0.5	0.2	0.0	-
3	0.4	0.0	-	-	-
4	0.8	0.5	0.3	0.0	-
5	0.8	0.3	0.1	0.0	-

Table 5.6(c): Particle positions for the -20+15mm fractions

	Fraction of co-deflected granite at specified distance from blue particle				
Position number	Close together	2mm	4mm	6mm	10mm
1	1.0	0.9	0.7	0.2	0.0
2	1.0	0.3	0.1	0.0	-
3	0.6	0.0	-	-	-
4	1.0	0.5	0.3	0.0	-
5	1.0	0.2	0.0	-	-

A fraction of co-deflected granite value of 1.0 indicates that for all 100 pairs of particles placed at a certain distance from each other, both particles were always co-deflected. A value of 0.9 indicates that 90 out of the 100 pairs were co-deflected for that distance and so on.

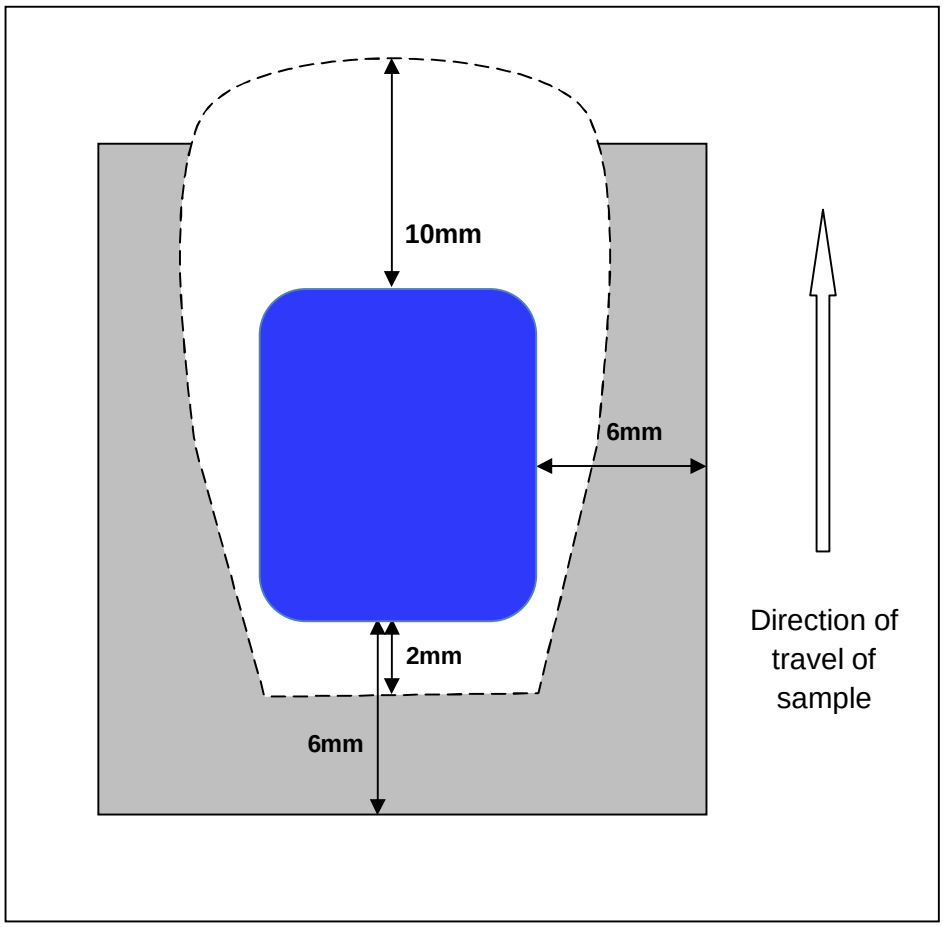

Figure 5.15: Particle zone of influence. The white zone represents approximately an area where the granite particles are likely to be co-deflected

These results indicate that particles close together and up to approximately 2mm apart are co-deflected. Depending on the positioning, particles greater than 2mm apart are co-deflected to varying degrees as displayed in Figure 5.15.

The particles which have the blue particle placed before the granite particle may not be deflected especially in positions number 2 and 3 (see Figure 5.14). In this position, the valves are already opened ensuring deflection. For position number 5 since the nozzle diameter is 2.1mm particles greater than 4mm apart are rarely affected.

The zone of influence of a particle obtained from the coverage of a valve on each particle is skewed to the initial 10mm in the direction of travel of the particle on the conveyor belt especially if a granite particle is placed approximately 6mm to the top of the blue particle. The reason for this outcome is related to the valve opening and closing times, which are the time it takes the valve to energize and de-energize (see Chapter 2, sub-section 2.0.3).

5.2.7 Summary

The calculated % belt loading in this research ranged between 0.5 – 3.35% (as shown in Figures 5.5). There is a linear relationship between belt loading and co-deflections as indicated in Figure 5.6. Since co-deflection affects separation efficiency with this relationship, separation efficiency could be calculated if the belt loading and % to be deflected is known. For all the samples sizes and shape classes, the number of composites formed increased with an increase in % blue deflect and throughput as indicated in Figures 5.8. There is a reasonable relationship between composites formation and co-deflections as shown in Figure 5.9.

Monte Carlo analyses tend to underestimate the number of single particle 'composites' as shown in Figures 5.13. This could be explained by the automated sorter seeing particles close together (but touching each other) as composites. Another reason could be that the distribution of the

particles on the belt is not random. An occurrence due to channelling linked with the chute width.

The zone of influence of a particle obtained from the coverage of a valve on each particle is controlled by the positioning of the blue particle as shown in Figure 5.15.

5.3 DISCUSSION: FACTORS CONTROLLING AUTOMATED SORTER EFFICIENCY

Manouchehri (2003) discussed the factors for optimal optical sorting. These factors included feed size, feed surface (where a clear surface is ideal) and appropriate colour identification of the feed. These criteria were applied while undertaking these investigations with investigations designed to maximize identification. It is known that throughput increases with size for the automated sorter and a decrease in the fraction of particles requiring deflection (De Jong and Harbeck, 2005). The results presented in the previous sections confirm these findings. The effect of shape not previously mentioned is also discussed.

This section is sub-divided into machine controlled and material controlled factors.

5.3.1 Machine Controlled Factors

5.3.1.1 Air ejector precision

The medium by which materials were deflected or separated was compressed air. Sufficient air pressure was required for efficient separation. A major factor controlling performance is the occurrence of 'touching' particles in close proximity leading to co-deflections. However observations with regards to valve design and sensitivity of the automated sorter suggest that lower energising (and de-energising times) times could yield improved separation due to lower co-deflections. This is because the zone of potential disturbance around a particle which has a relationship with valve energize and the de-energize times would be smaller. For particles fed at a speed of $3ms^{-1}$ in a millisecond 3mm is covered. For a valve with energising time of 3.4ms it follows that a 10.2mm distance is covered before the valve is fully energized. Approximately 4 to 6mm spacing is required (depending on the positioning of the particle required to be deflected) between particles for adequate separation due to a de-energising valve timing of 1.5ms. Also the skewed configuration shown in Figure 5.15 could be corrected for by valve designs with equal energize and de-energize timings.

For the TiTech design, rejection settings are also important factors for separation. For instance should the materials be small sized (less than 10

mm) and less dense (less than 2650kgm^{-3} of granite), with adequate compressed air then separation of such materials using 'rejection mode 3' could yield improved separation efficiency.

5.3.2 Material Controlled Factors

These are factors associated with the materials that require sorting. They include size, shape and colour if the sensor is a colour camera.

5.3.2.1 Size

A reduction in particle size leads to an increased belt coverage for a specific throughput, leading to a higher probability of particles coming into close contact and being co-deflected. Conversely, separation improves with larger sizes as there is a lower probability of particles coming into close contact and forming composites. These effects are shown in Figure 5.1.

These tests were also discussed in section 5.1 where the relationships between sizes and throughput were investigated. Manouchehri (2006) suggested that % deflection 'grades' greater than 30% may not be economic for sample fractions less than 5mm. Results shown in Figure 5.3 help explain why this may be the case. Figure 5.3 indicated that co-deflections increase with an increase in throughput and percent deflections and for the -10+6mm fraction at 30% deflection for 2.5tonnes/hr throughput, up to 25% co-deflection was recorded. It follows therefore that at such a throughput with a 70 to 75% separation efficiency, the sorter separation may not be economic.

5.3.2.2 Shape

Investigations into the effect of particle shape indicate that although flaky shaped particles required less compressed air for deflection when compared to cubical shaped particles, they did not yield the highest separation efficiency. This suggests that cubical shaped materials even with slightly higher compressed air consumption are an ideal particle shape for separation. Particle shape was shown to affect co-deflection up to 10% depending on the throughput and % blue deflect (see Figure 5.4).

For our sorter, in summary, the deflecting mechanism such as the design of valve nozzles and rejection settings together with the particle size and shape are important factors affecting separation efficiency. The % blue deflect less than 50% would yield improved separation efficiency. This is because there is a higher probability that particles inadvertently get co-deflected at higher deflection rates.

At a reduced cut-off recovery percentage (% blue of measured particle used in ejection algorithm) the separation efficiency may be improved. The settings for these investigations were a 20% blue content which was to enhance recovery of all blue painted particles. Preliminary investigations indicate that at a 50% blue content setting the recovery of blue materials will be reduced but could reduce co-deflections of granite materials into the deflect collector bins (see Table 4.8). A two stage sorting process would be expected to potentially improve the separation of the materials.

Particle identification is still a key separation efficiency parameter. However in this research for ease of model calculations, identification was enhanced more than may be obtained for materials requiring sorting.

CHAPTER 6

MODELLING EFFICIENCY

This Chapter discusses how the previously proposed model discussed in Chapter 2 (King, 1978), was modified. The model comprises the identification and deflection parameters together with the parameter representing the % blue deflect. The identification and deflection probabilities were calculated by undertaking separation efficiency tests.

6.0 MODEL CALCULATIONS

6.0.1 Material parameters

Consider a mixture of accept and deflect particles fed to the sorter for which the deflect particles are always deflected,

The identification parameters (I)

I(d/d) = Fraction of deflect particles that are identified as deflect

I(a/d) = Fraction of deflect particles that are identified as accept (1-I(d/d))

I(d/a) = Fraction of accept particles that are identified as deflect (1-I(a/a))

I(a/a) = Fraction of accept particles that are identified as accept

The identification parameters are represented as fractional values ranging between 0 and 1. So a value of 99% will be recorded as 0.99. With a clear painting of test particles identification parameters I(d/d) and I(a/a) approximate to 1 and I(a/d) and I(d/a) approximate to 0.

The deflection parameters (D)

D(d/d) = Fraction of identified deflect particles deposited in the deflect bin

D(a/d) = Fraction of identified deflect particles deposited in the accept bin

D(a/a) = Fraction of identified accept particles deposited in the accept bin

D(d/a) = Fraction of identified accept particles deposited in the deflect bin

The deflection parameters are also represented as values ranging between 0 and 1.

Another parameter is the % blue deflect (P).
P_a = Fraction of the test batch to be accepted
P_d = Fraction of the test batch to be deflected

The blue % deflect varies between 0 and 1 with a 10% deflection recorded as 0.1, 20% 0.2 up to 50% (0.5) which is a 50:50 split between accept and deflect particles.

King noted that the mass fraction of particles that would be recovered from accept or the deflect bins is shown below.

$$E(l) = D(o/o,l)I(o/o,l)P(o/l) + D(o/o,l)I(o/w,l)P(w/l) + D(o/w,l)I(w/o,l)P(o/l) + D(o/w,l)I(w/w,l)P(w/l)$$

Using the calculations, this equation now becomes:

Deflect product = P_d x I(d/d) x D(d/d) + P_d x I(a/d) x D(d/a) + P_a x I(d/a) x D(d/d) + P_a x I(a/a) x D(d/a)

Accept product = P_a x I(a/a) x D(a/a) + P_a x I(d/a) x D(a/d) + P_d x I(a/d) x D(a/a) + P_d x I(d/d) x D(a/d)

These products can also be represented graphically as shown in Figure 6.1.

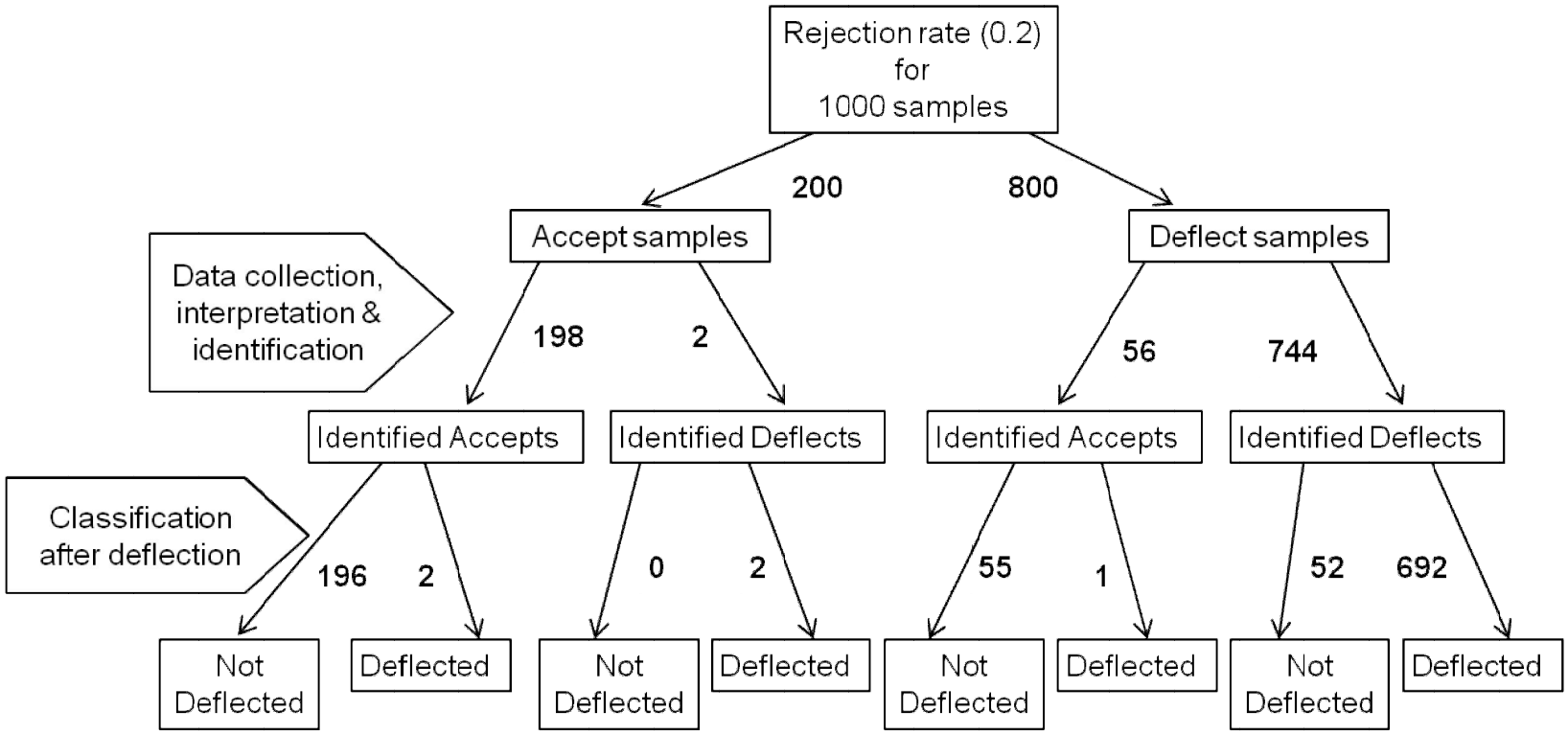

Figure 6.1: Distribution of samples based on identification parameters (I(a/a) = 0.99, I(d/d) = 0.93) and deflection parameters (D(a/a) = 0.98 and D(d/d) = 0.99

The separation efficiency (R_b - R_g) relationship has also been applied to model separation efficiency. This relationship is discussed in sub-section 6.1.

6.1 EFFICIENCY LOSS RELATIONSHIPS

6.1.1 Efficiency of blue particle deflection (R_b)

Results for most of the separation efficiency tests shown in Table 5.1 indicate that the recovery of blue particles to be approximately 99.5% except for the cubic shaped -20+15mm fraction. Hence the identification parameters [I((a/a), I(d/d) = 1] and R_g = 99.5%. Investigations suggest that separation efficiency losses occur as a result of co-deflections. The number of co-deflected particles [D(d/a)] is therefore of importance.

6.1.2 Efficiency of granite particle co-deflection (R_g)

One reason for accept particles being co-deflected could be that they are touching or within close proximity of at least 1 blue particle. It is assumed that if one blue particle were present in a composite the majority of the composite's particles would be deflected. This is because of the low blue threshold that was used in this work (to maximise recovery). Figure 5.6 shows the likely combinations of accept and deflect particles in a composite. The probability of a composite containing a blue particle increases as the % blue deflect of the particles increases.

The probability of a composite containing all accept, all blue or mixed components is given by.

$$P_{(a/a)} + P_{(d/d)} + P_{(a/d)} = 1 \qquad (6.1)$$

Where:

$P_{(a/a)}$ = probability of only accept particles in the composite

$P_{(d/d)}$ = probability of only blue (deflect) particles in the composite

$P_{(a/d)}$ = probability of a combination of accept and blue (deflect) particles in the composite.

The probabilities depend on the fraction of feed that is accepted and blue particles to be deflected (P_a and P_d). For a composite made up of 'n' particles:

$$P_{(a/d)} = 1 - P_d^n - (1-P_d)^n \qquad (6.2)$$

6.2 THE MODEL

Using the distribution of composites shown in Figure 5.6 the measured value of D(d/d) and the likely composition of composites from equation 6.2 a prediction of the misplaced accepts/co-deflection (R_g) was made for various operating conditions.

To calculate separation efficiency (SE), the formula utilised (See Equation 2.17) is shown below

$$SE\ (\%) = R_b - R_g \tag{6.3}$$

Where

R_b = Recovery of deflect particle to the deflect bin

R_g = Recovery of co-deflected accept particles to the deflect bin

From the elongated/flaky particles it was demonstrated that the probability of deflecting blue particles [D(d/d)] was close to unity suggesting that these particles follow a predictable trajectory. Inefficiency in sorter performance could therefore, in the case of easily identifiable materials [I(d/d) and I(a/a) = 1], be attributed to accept particles that are inadvertently deflected due to their proximity to particles that are deflected [with D(d/a) <1].

Since R_b for most of the tests is approximately 99.5%, it follows that equation 6.3 can be written as

$$SE\ (\%) = 99.5 - R_g \tag{6.4}$$

For the feed characteristics (perfect identification) and sorting system set-up, R_g and separation efficiency can be estimated.

Using the graph of R_g vs B_L (belt loading) produced (see Figure 5.6), applying the equation of a line (y = mx), the relationship between R_g and B_L can be calculated as follows

$$R_g = mB_L$$

(6.5)

Where

'm' is the slope for the graph shown in Figure 5.6, 'm' can be represented as shown in equation 6.6, where 'K' is a constant and N_d is the % blue deflect.

$$m = KN_d \quad (6.6)$$

For N_d of 50%, y = 7.0286x; for 30%, y = 5.1437x; for 10%, y = 1.9938x. Plotting m versus N_d and forcing the regression line through 0 presented in Figure 6.2, the slope for the equation represents K which is approximately 15.

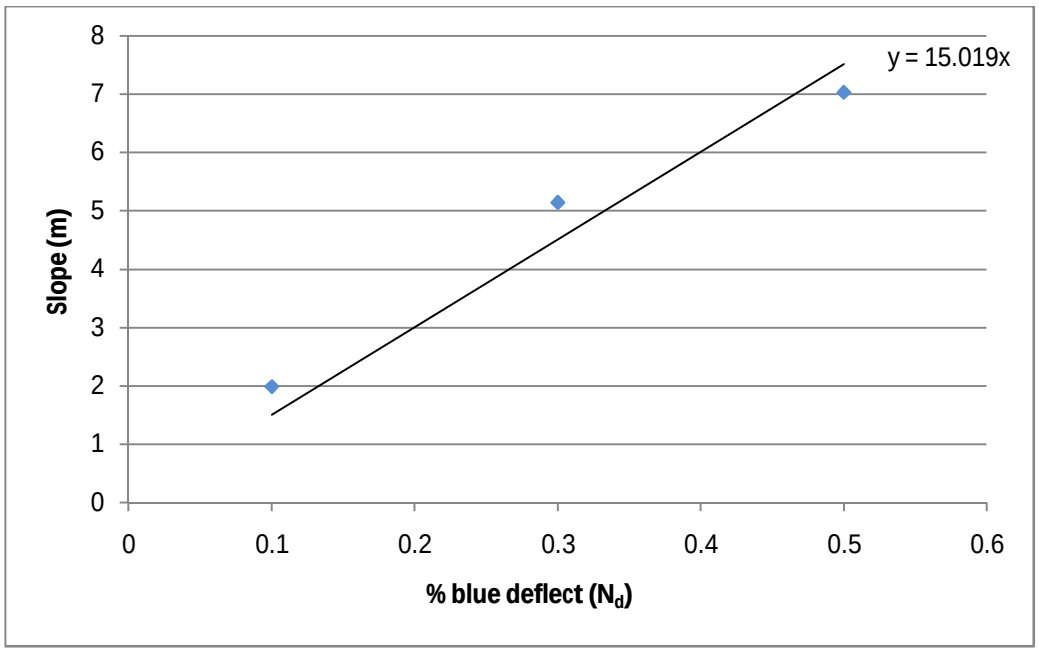

Figure 6.2: The slope and belt loading relationship

Hence

$$R_g = 15N_dB_L \quad (6.7)$$

Where

N_d = % blue deflect

B_L = Belt loading

The separation efficiency can then be calculated as follows:

$$SE\ (\%) = 99.5 - 15N_dB_L \tag{6.8}$$

Assuming identification is perfect, R_b can be rounded off and equation 6.8 can be represented as

$$SE\ (\%) = 100 - 15N_dB_L \tag{6.9}$$

6.3 MODEL VALIDATION

Validating the model involved procedures similar to those for experimental investigations discussed in Chapter 4. The procedures are discussed further. The validation was undertaken with 'black' and 'white' separation of -20+14mm sized particles at 25% deflection and 0.5 and 2.5tonnes/hr throughputs.

6.3.1 Sample preparation

Ore from Greenland with carbonate (dolomite, marble) and metamorphosed mudstone or slate (pelite) composition was screened into the -20+14mm size fraction. The shape of the samples was not considered. The dolomite and marble have a white-like colour while the pelites were dark grey to black in colour. To ensure clear colour differentiation between the carbonates and pelites, the darker particles was painted black with proprietary water based masonry paint. The density of the ore was determined to be 2795kgm^{-3} using the procedure discussed in Chapter 4, sub-section 4.0.

6.3.2 Machine preparation and test procedures

Machine preparation and test procedures followed similar procedures to those discussed in Chapter 4, sub-section 4.1 and 4.2.

Colour separation was based on the Y (brightness) colour scale only (see Table 6.1).

Table 6.1: Y colour scale values used for validation tests

Classification	Y Min	Y Max
Black	0	65
White	65	255
Background	65	115
Off-white	65	125

With these classification any particle with a brightness intensity <65 was considered black. The material separation rules were set to deflect particles with a >30% black pixel intensity cut off (see Chapter 4, sub-section 4.2.2), and accept the white and off-white particles.

The throughput of the samples was calibrated with the procedure described in Chapter 4, sub-section 4.2.2. The results of the calibration are presented in Figure 6.3.

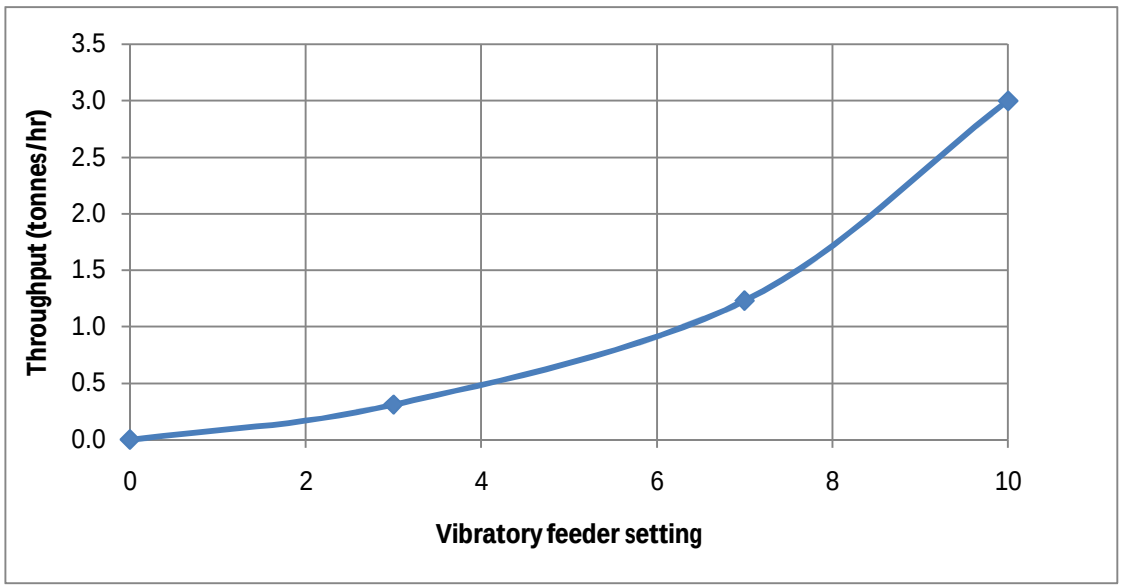

Figure 6.3: Throughput calibration for the -20+14mm particles

As the sample size was similar to that used for the earlier experimental investigations, a similar delay time of 26ms was used for these tests.

The splitter positioning used was 68°; the distance between the tip of the splitter to the edge of the conveyor belt was 33cm (see Chapter 4, sub-section 4.2.2). The air pressure used was 550kNm^{-2}. Deflection was undertaken using rejection rule 1.

Separation efficiency validation investigations were undertaken for a 25% black deflection at 0.5 and 2.5tonnes/hr. Each set of tests were repeated 4 times.

6.3.3 Calculating separation efficiency using the model

The particle x, y, z diameter were 20mm, 14mm for the x and y components. For the 'z' component, the method described in Chapter 4, sub-section 4.3.1 was used. For a total of 210 particles the weight obtained was 1644.8kg. Using the density-mass-volume relationship the 'z' diameter

was calculated to be 10mm. With a particle density of 2795kgm^{-3} the belt loadings at 0.5 and 2.5tonnes/hr can be calculated as follows:

$$B_L\ (\%) = 100 \times \frac{Nxy}{WS}$$

First 'N' the number of particles in calculated. Using particle dimensions of 20, 14 and 10mm representing the x, y and z diameters respectively, produces a volume of 0.0000028m^3, with a density of 2795kgm^{-3}, the mass of the particles was 0.007826kg.

Therefore 'N' for 0.5tonnes/hr, 25% deflection is:

$$\text{Number of particles} = \frac{0.1389\ \text{kgs}}{0.007826\ \text{kg}} = 18\text{ptc/sec}$$

Where:
The conversion of throughput 0.5tonnes/hr gives 0.1389kgs^{-1}.

The belt loading for a belt width (W) of 0.55m and speed (S) of 3.02ms^{-1} is:

$$B_L\ (\%) = 100 \times \frac{18\text{ptc/sec} \times 0.02\text{m} \times 0.014\text{m}}{0.55\text{m} \times 3.02\text{ms}^{-1}} = 0.3036\text{m}$$

With the belt loading calculated the separation efficiency for a 25% deflection (N_d) at 0.5tonnes/hr is:

$$SE = 99.5 - (15 \times 0.25 \times 0.3036\text{m}) = 98.4\ \%$$

Following the same procedure, the separation efficiency at 2.5tonnes/hr was 93.9%.

6.3.4 Results

A comparison of the calculated and actual SE is presented in Table 6.2.

Table 6.2: Validation and calculated separation efficiency results

Number of test repeats	Separation efficiency SE (%)	
	At 0.5 tonnes/hr	At 2.5 tonnes/hr
1 2 3 4	98.8 99.1 97.2 98.7	93.1 95.0 94.6 95.1
Average	98.45	94.45
Calculated SE (%)	98.4	93.9

It can be seen that there is a reasonable correlation between the model and actual separation efficiency results.

6.4 DISCUSSION

The model indicates that once a clear cut colour identification is achieved, the fraction of particles requiring deflection and belt loading are key parameters to determining separation efficiency. The belt loading which is linked to the machine throughput and particle size increases with throughput.

The fraction of the whole feed that requires deflection is also of importance. Ideally the least number of particles should be deflected. This is not just to save on compressed air (if the separation was via air jets) but also to reduce the probability of co-deflections.

If there is perfect identification up to 100%, then the R_g component of the model can be set at 100 instead of 99.5. For situations where identification is less than ideal then a lower R_g value (approximately 95 to 98%) could be substituted. This value could be determined from preliminary experimentation.

CHAPTER 7

CONCLUSIONS AND RECOMMENDATIONS FOR FUTURE RESEARCH

7.0 CONCLUSIONS

The tests indicate that separation efficiency decreases with an increase in throughput and decrease in size. For finer sizes (< 10mm) the separation efficiency was lower than for coarser sizes (-20+15mm). The decrease in separation efficiency can be explained by the 'touching' of sample particles to form composites as the particles are transported for sorting. These composites lead to the inadvertent deflection of 'accept' with 'deflect' particles being deflected by the compressed air jets.

The fraction of particles requiring deflection is of importance. Investigations indicate that increased percentage of particles requiring deflection gives greater probability that a deflect particle would be in a composite, increasing the probability of a co-deflection.

The effect of shape on separation efficiency indicates that cubic shaped particles generally produce a higher separation efficiency. Valve sensitivity was also identified to be an important separation efficiency factor. Solenoid valves which have lower overall energise and de-energising times would be of advantage as the amount of co-deflections would be reduced.

Monte Carlo simulations of particle distribution under-predicts the number of particles coming in contact (touching) on the conveyor belt suggesting that the actual distribution was not random. This was a limitation of the feed chute.

The separation model presented comprises of two variables, the belt loading (representing samples size shape throughput) and % blue deflect (the

fraction of particles requiring deflection) N_d. The separation efficiency (SE) can be calculated once N_d and belt loading B_L are known as follows:

$$SE\ (\%) = 99.5 - 15N_dB_L$$

To improve separation efficiency, between 1 to 30% of the total test batch of particles should be deflected and cubic shaped particles should be used where possible.

7.1 RECOMMENDATIONS FOR FUTURE RESEARCH

Future research is suggested in the following areas:

- Discrete element methods

Results discussed in Chapter 5, sub-section 5.2.5 indicate that Monte Carlo simulation of belt distribution under-predicted the number of touching particles. These discrepancies may be as a result of a non-random particle distribution. To further study the interaction of particles on a belt and the formation of composites, discrete element methods could be applied to explore the relationships between particles.

- Tests at a feeding system design

Test observations indicated that the distribution of particle is important. Better design of the feeding system can reduce the likely formation of composites. It would be worthwhile to investigate further into means of producing uniform particle distribution on the belt through other means of feeding particles.

This can be undertaken by using a hopper with a feeding chute equivalent to the width of the belt. Another method would be by restricting the belt to fit with the width of the feeding chute.

- Tests at a different presentation configuration

This research investigations were undertaken with particles presented using a conveyor belt. It would be worthwhile to investigate particle composite formation and distribution for particles presented from a chute discharged in free-fall to the sensors.

- Two stage separation modelling

The model was based on a single stage separation. It is known that a two stage separation process could yield higher separation efficiency and would be worthy of investigation to incorporate the results into the model.

REFERENCES

Acharya, T. and Ray, A.K. 2005. Image processing: Principles and applications. John Wiley and sons Inc., New Jersey, 427p.

Adams, J.A.S. and Gasparini, P., 1970. Gamma-ray spectrometry of rocks. Elsevier publishing company Amsterdam 295p.

Adorjan, L.A., 1985. Mineral processing innovations. *Canadian Metallurgy Quarterly,* **24** (1) 15-25. Canadian Inst. Mining & Metall. publication.

Amankwah, R.K., Khan, A.U., Pickles, C.A. and Yen W.T., 2005. Improved grindability and gold liberation by microwave pre-treatment of a free-milling gold ore. *Trans. Institutions of Mining and Metallurgy, Section C*, **114** (1) 30-36.

Anon, 2006. X-rays for high-grading coal. Mining Mirror magazine, (Dec.), 24.

Anselmi, B. and Harbeck, H., 2000. Multicolour optical sorting: A large scale application in a feldspar treatment plant in Sardinia, Italy. In: Proceedings of the XXI International mineral processing congress, Rome 2000, Massacci, P. (ed.) Elsevier, Amsterdam Vol. C, C11-9 to C11-16.

Arvidson, B.R., 1988. Industrial minerals beneficiation by ore sorting. In: 8th Industrial Minerals International Congress, Boston, G.M. (ed.) London Metal. Bulletin plc., 138-146.

Arvidson, B.R., 2002. Photometric Ore Sorting. In: Mineral Processing Plant Design, Practise and Control Proceedings Vol 1. Mular *et al* (eds.) Society of Mining, Metall & Exploration Colorado USA, 1033 -1048.

AU, 2008. {Internet} Available at: http://www.appliedsorting.com.au/ (Accessed January 2008).

Barlow, D., 2001. Glass recycling – The UK scene In: Recycling and Reuse of Glass Cullet. Dhir, R.K., Limbachiya, M.C. and Dyer T.D. (eds.) Proc. International Symposium of the Concrete Technology Unit, University of Dundee, UK, 11 -14. Thomas Telford publishers, London.

Bayram, M. and Oner, M.D. 2006. Determination of applicability and effects of colour sorting system in bulgur production line. *Jour. food Engng.* **74** 232-239.

Bibby, P., 1982. Preconcentration By Radiometric Ore Sorting. Mill Operators Conference, Australasian Inst. of Min. and Metall. (Australasian IMM symposia series no 30) 193 -201.

Blasco, J., Cubero, S., Gomez-Sanchis, J., Mira, P. and Molto, E. 2009. Development of a machine for the automatic sorting of pomegranate (*Punica granatum*) arils based on computer vision. *Jour. food Engng.* **90** 27-34.

Brockington, J., Stamper, P.J. and Browning, D.R., 1985. Physical chemistry for higher education. Longman publishers New York 392p.

Bruno, E.A, 2000. {Internet} Automated sorting of plastics for recycling. Available at: www.p2pays.org (Accessed April 2009).

BS 1997. British standard EN 933-1 aggregate sizing standards.

Cinque, L and Lombardi, L, 1995. Shape description and recognition by a multiresolution approach, *Image and vision computing*, **13** (8), 599 - 607.

CommoDas, 2006. {Internet} Available at: www.commodas.com (Accessed October 2007).

Cutmore, N.G., Liu, Y. and Middleton, A.G., 1998. On-line Ore characterisation and sorting. *Minerals Engineering,* **11** (9) 843 -847.

Cutmore, N.G., Evans, T.G., McEwan, A.J., Rogers, C.A. and Stoddard, S.L., 2000. Low frequency microwave technique for on-line measurement of moisture. *Minerals Engineering,* **13** (14-15) 1615 -1622.

Cutmore, N.G. and Eberhardt, J.E., 2002. The future of Ore Sorting in Sustainable Processing. Aus. IMM, **4** 287-290.

Dalmijn, W.L. and De Jong, T.P.R., 2004. Sorting systems for recycling and waste treatment. Voordracht VUB Brussel, 25e seminarie Het beheer van afvalstoffen.

De Jong, T.P.R., Mesina, M.B. and Kuilman, W., 2003. Electromagnetic de-shaling of coal. *Physical separation in Sci. & Engng.* **12** (4) 223-236.

De Jong, T.P.R., Fabrizi, L. and Dalmijn, W.L., 2004. Dry separation of mixed construction and demolition waste. *Recycling International*

De Jong, T.P.R. and Harbeck, H., 2005. Automatic sorting of minerals: Current status and future outlook. Proceedings of 37th Annual Meeting of the Canadian Mineral Processors, 629-648.

Delwiche, S.R., Pearson, T.C., and Brabec, D.L. 2005. High-speed optical sorting of soft wheat for reduction of Deoxynivalenol. *Plant disease* **89** (11) 1214-1219.

Denney, R.C, and Sinclair, 1987. Visible and Ultraviolet spectroscopy. John Wiley and sons publishers, Chichester, 197p.

Dodbiba, G., Shibayama, A., Miyazaki, T and Fujita, T. 2003. Separation performance of PVC and PP plastic mixture using air table. *Phy. Sep. Sci. & Engng.* **12** (2) 71-86.

Dodbiba, G., and Fujita, T. 2004. Progress in separating plastic materials for recycling. *Phy. Sep. Sci. & Engng.* **13** (3-4) 165-182.

Dowell, F.E., Boratynski, T.N., Ykema, R.E., Dowdy, A.K. and Staten, R.T., 2002. Use of Optical Sorting to detect wheat kernels infected with *Tilletia indica*. *Plant Disease,* **86** 1011–1013.

ERIEZ, 2009 {Internet} Available at: www.eriez.com (Accessed January 2009).

FESTO, 2009. FESTO valve catalogue. {Internet} Available at: https://xdki.festo.com/xdki/data/doc_engb/PDF/EN/ISO15407VSVA_EN.PDF (Accessed October, 2009).

Fernlund, J.M.R., 2005. Image analysis method for determining 3-D size distribution of coarse aggregates. *Bull. Engng. Geol. Environ.* **64** 159-166.

Fitzpatrick, R.S., 2008. The development of a methodology for Automated sorting in the Minerals Industry. Unpublished PhD thesis. Camborne School of Mines, University of Exeter 323p.

Fleischer, U. and Bergmann, J., 2004. Waste separation with the Mogensen AR 1200 x-ray sorter. A*ufbereitungs Technik,* **45** (11) 5-10.

Forsthoff, W. 2000. Optical sorting of coarse materials. *ZKG International,* Bauverlag GmbH Germany.

Fuerstenau, MC and Han, K.N (eds.) 2003. Principles of Mineral processing. Society of Mining metallurgy and Exploration Inc. Colorado 570p.

Gaydon, J.W., Glass, H.J. and Pasoce, R.D. 2009. Method for near infrared sensor-based sorting of a copper ore. *Jour. Near infrared spectroscopy* **17** 177-194.

Goldbook, 2009. {Internet} Available at: http://goldbook.iupac.org/X06718.html (Accessed August 2009).

Gomez, A.H., Yong, H., and Pereira, A.G. 2006. Non-destructive measurement of acidity, soluble solids and firmness of Satsuma mandarin using Vis/NIR-spectroscopy techniques. *Jour. food Engrg.* **77** 313-319.

Gonzalez, R.C. and Woods, R.E. 1992. Digital image processing. Addison-Wesley publishing Reading 716p.

Gordon, H.P and Heuer, T. 2000. New age radiometric ore sorting – the elegant solution. In: Proceeding of the Int. symposium of process metallurgy of uranium, Saskatchewan 2000, Ozberk E., Oliver, A.J. (eds.) 323-337.

Jack, K. 2005. Video demystified: A handbook for the digital engineer (4th ed.) Elsevier Inc. Oxford, UK, 921p.

Kattentidt, H.U.R., De jong, T.P.R., and Dalmijn, W.L. 2003. Multi-sensor identification and sorting of bulk solids. *Control Engng. Practice.* **11** 41-47.

Kelly R.M, and Rowson, N.A. 1995. Microwave reduction of oxidized ilmenite concentrates. *Minerals Engineering.* **8** (11) 1427-1438.

KEY, 2010. {Internet} Product description of Tegra sensor based sorter for food processing. Available at: www.key.net (Accessed March 2010).

Killmann, D., and Pretz, T. 2006. Possibilities of sensor-based sorting regarding recycling of waste. *Acta Mettalurgica Slovaca* **12** 188-193.

King, R. P., 1978. Automatic sorting of ores. *Mineral Sci. Engng.,* **10** (3) 198-207.

Kingman, S.W., Voster, W. and Rowson, N.A. 2000. Influence of mineralogy on microwave assisted grinding. *Mineral Engineering* **13** 313-327.

Kingman, S.W., Jackson, K., Cumbane, A., Bradshaw, S.M., Rowson, N.A. and Greenwood R. 2004. Recent developments in microwave-assisted comminution. *Int. Jour. Min. Pro.* **74** 71-83.

Kolacz, J., and Chmelar, J. 2002. Cost effective optical sorting system. *Recycling and waste treatment in Min. & Metal Pro.* 313-322.

Krummenacher, B., Peuch, P., Fisher, M., Biddle, M., 1998. Automatic identification and sorting of plastics from different waste streams. *Assoc. of Plastics Manu. In Europe* Technical report.

Kwok, H., Cheng, P., Huang, H., Li, H., Zheng, Z., Gu, P. and Liu, X. 2000. Trichroic prism assembly for separating and recombining colours in a compact projection display. *Applied optics* **39** (1) 168-172.

Lamprecht, G.H., Human, H.G.C. and Snyman, L.W. 2007. Detection of diamond in ore using pulsed laser Raman spectroscopy. *Int. Jour. Min. Pro.* **84** 262-273.

Lees G., 1964. The measurement of particle shape and its influence in engineering materials. In Smith, M.R. and Collins, L (eds) Aggregates: Sand, gravel and crushed rock aggregates for construction purposes. *Geol. Soc. Engng. Geology special pub*. 9. 340p.

Leitner, R., Mairer, H and Kercek, A., 2003 Real-time classification of polymers with NIR spectral imaging and blob analysis. *Real-Time Imaging* **9** 245-251

MAC, 2008. MAC 44 valve catalogue. {Internet} Available at: http://www.macvalves.com/support/catalogs_files/NT.pdf (Accessed November, 2008).

Manouchehri, H.R., 2003. Sorting: Possibilities, Limitations and Future. *Proc. Mineral Pro. Conference Feb. 2003* Luleå, Luleå University of Technology, Sweden (Mf MinFo 33)

Manouchehri, H.R., 2006. Application of Optoelectronic sorting technique for upgrading minerals and wastes. *Proc. Mineral Pro. Conference Feb. 2006* Luleå, Luleå University of Technology, Sweden.

Mesina, M.B., De Jong, T.P.R. and Dalmijn, W.L., 2007. Automatic sorting of scrap metals with a combined electromagnetic and dual energy X-ray transmission sensor. *Int. Journal of Min. Processing,* **82** 222-232.

Mora, C.F., Kwan, A.K.H. and Chan, H.C., 1998. Particle size distribution analysis of coarse aggregate using digital image processing. *Cement and Concrete Research*. **28** (6) 921-932.

Morin, M. A. and Ficarazzo, F., 2006. Monte Carlo simulation as a tool to predict blasting fragmentation based on the Kuz–Ram model. *Computers and Geosciences,* **32** 352-359.

MRA, 2004. {Internet} Dilution control by means of Laser-Induced fluorescence. Available at: http://www.miningreview.com/archive/034/44_1.htm (Accessed August, 2009).

Nijkerk, A.A. and Dalmijn, W.L., 1998. Handbook of Recycling Techniques. 4th ed. Nijkerk Consultancy, The Hague 216p.

Pascoe, R.D., 2000. Sorting of waste plastics for recycling *Rapra review reports* **11** (4). Rapra Technology ltd. UK, Report 124.

Pasquini, C., 2003. Near infrared spectroscopy: Fundamentals, practical aspects and analytical applications. *J. Braz. Chem. Soc.* **14** (2) 198-219.

Pickles, C.A, 2005. Microwave drying of nickeliferous limonitic laterite ores *Canadian Metallurgical Quarterly*, **44**, (3), 397-408.

Pike D.C., 1990 (ed.) Standard for aggregates. Ellis Horwood (Ltd.) England. 280p.

Rayner, J. (ed) 2005. Materials Recycling Handbook. Emap Maclaren Ltd. Publications

Salter, J.D. and Wyatt, N.P.G., 1991. Sorting in the Minerals Industry: Past, Present and Future. *Minerals Engineering* **4** (7-11) 779-796.

Schapper, M.A. 1977. Beneficiation at large particle size using photometric sorting techniques. *Australian Mining* **69** (4) 44-53.

Schulz, N.F. 1970. Separation efficiency. *Trans SME-AIME,* **247** (1) 81-87.

Serranti, S., Bonifazi G., and Pohl, R., 2006. Spectral cullet classification in the mid-infrared field for ceramic glass contaminants detection. *Waste Management Research,* **24** (48) 48-59.

Singh, V. and Rao, S.M. 2006. Application of image processing in mineral industry: a case study of ferruginous manganese ores. *Min. Pro. and Extractive Metallurgy (Trans. Inst. Min. Metall. C).* **115** (3) 155-160.

Sivamohan, R. and Forssberg, E., 1991. Electronic Sorting and other Preconcentration Methods. *Minerals Engineering* **4** (7-11) 797-814.

Skoog, D.A West, D.M. and Holler, F.J. 1996. Fundamentals of Analytical Chemistry (7th ed.) Saunders College Publishing, New York 870p.

Smith, M.R. and Collis, L.(eds) 1993. Aggregates: sand, gravel and crushed rock aggregates for construction purposes. Engng. Geology Special Publications **9**, Geological Society of London.

Soldinger, M., 2002. Transport velocity of a crushed rock material bed on a screen. *Minerals Engineering* **15** 7-17.

Straughan, B.P. and Walker, S. (eds.) 1976. Spectroscopy. Vol. 2 and 3. John Wiley and sons publishing New York.

Stuart-Dick, D. and Royal, T.A. 1992. Design principles for chutes to handle bulk solids. *Bulk solids handling* **12** (3) 447-450.

Suzaimah, R., Mohd, M. M., Aini, H and Dzuraidah, A.W., 2008. Histogram of Intensity feature extraction for automatic plastic bottle recycling system using machine vision. *American Jour. of Env. Sciences* **4** (6) 583-588.

TOMRA, 2009. Tomra group structure {Internet} Available at: http://www.tomra.com/media/2008edition/group_structure_aug2008.htm (Accessed October 2009).

TVI, 2010. {Internet} True colour line scan technology. Available at: http://www.tvivision.com/articles.php (Accessed January, 2010).

UNICE, 2009. AOTF-NIR spectrometers. {internet} Available at: http://www.unice.com.tw/products/ome/c/c31.pdf (Accessed October, 2009).

USGS, 2006. USGS spectroscopic library {Internet} Available at: http://speclab.cr.usgs.gov/spectral.lib06 (Accessed October, 2009).

Varela, J.J., Petter, C.O. and Wotruba, H. 2006. Product quality improvement of Brazilian impure marble. *Minerals Engineering,* **19** 355-363.

VERTEX, 2008. Monte Carlo simulation basics {Internet} Available at: www.vertex42.com/ExcelArticles/mc/MonteCarloSimulation.html (Accessed September 2008).

Wells, I.S and Rowson, N.A., 1992. Application of rare earth magnets in Mineral processing. *Magnetic and Electrical separation* **3** 105-111.

Wills, B. A., 2006. Mineral Processing Technology. Butterworth Heinmann (7^{th} ed.) 444p.

Worrell, W.A. and Vesilind, P.A., 1979. Testing and evaluation of air classifier performance. *Resource recovery & conservation* **4** 247-259.

Zeiger, E. 2005. Glass recycling with Mogensen sorting and screening systems. A*ufbereitungs Technik* **46** (6) 1-7.

Zeuch, N., 2005. Machine vision in the food industry {Internet} Available at: http://www.machinevisiononline.org/public/articles/archivedetails.cfm?id=790 Accessed August, 2009.

APPENDIX A - DESCRIPTION OF THE PACT SOFTWARE AND LIST OF COMPLETE DATA EXTRACTED USING PACT

This section describes the various tab descriptions of the MicroSort© PACT sorting control system PACT version 1.18.406. The 23 image component data obtained from the automated sorter are also discussed.

Description of PACT software tabs

When PACT software is initialized the initial screen looks like that of Figure 1.

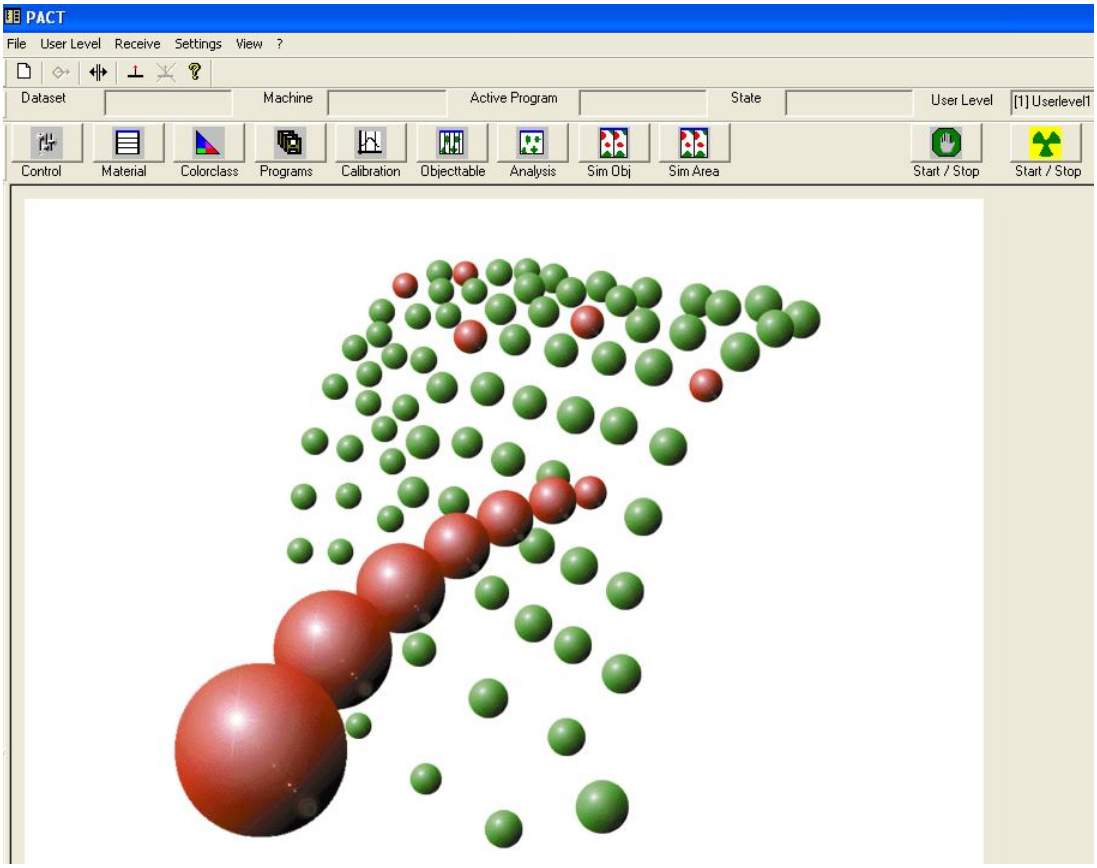

Figure 1: The initial start up screen of the PACT software

The overview of all the key tabs had been described in Chapter 3 of the thesis. This section describes these tabs with screen dump of the dialog boxes of the various tabs which were not described previously.

In Figure 1 the ***Dataset*** tab indicates which dataset is in operation from the various datasets programmed into the sorter. The ***Machine*** tab indicates which of the automated sorters is in operation if there is more than one sorter connected. ***State*** represents the status of the machine whether the sorter is ready, faulty or disconnected. The ***Userlevel*** is the administrative profile of the user. Each user level allows for control of the automated sorter, administrative powers progressing from user levels 1 to 5. For the ***Control*** tab, the operational state of the machine is indicated. The control activation button and the operational mode of the sorter are displayed. The Machine state is also displayed on the top ribbon, which runs through the whole software tabs as highlighted with arrows in Figure 2.

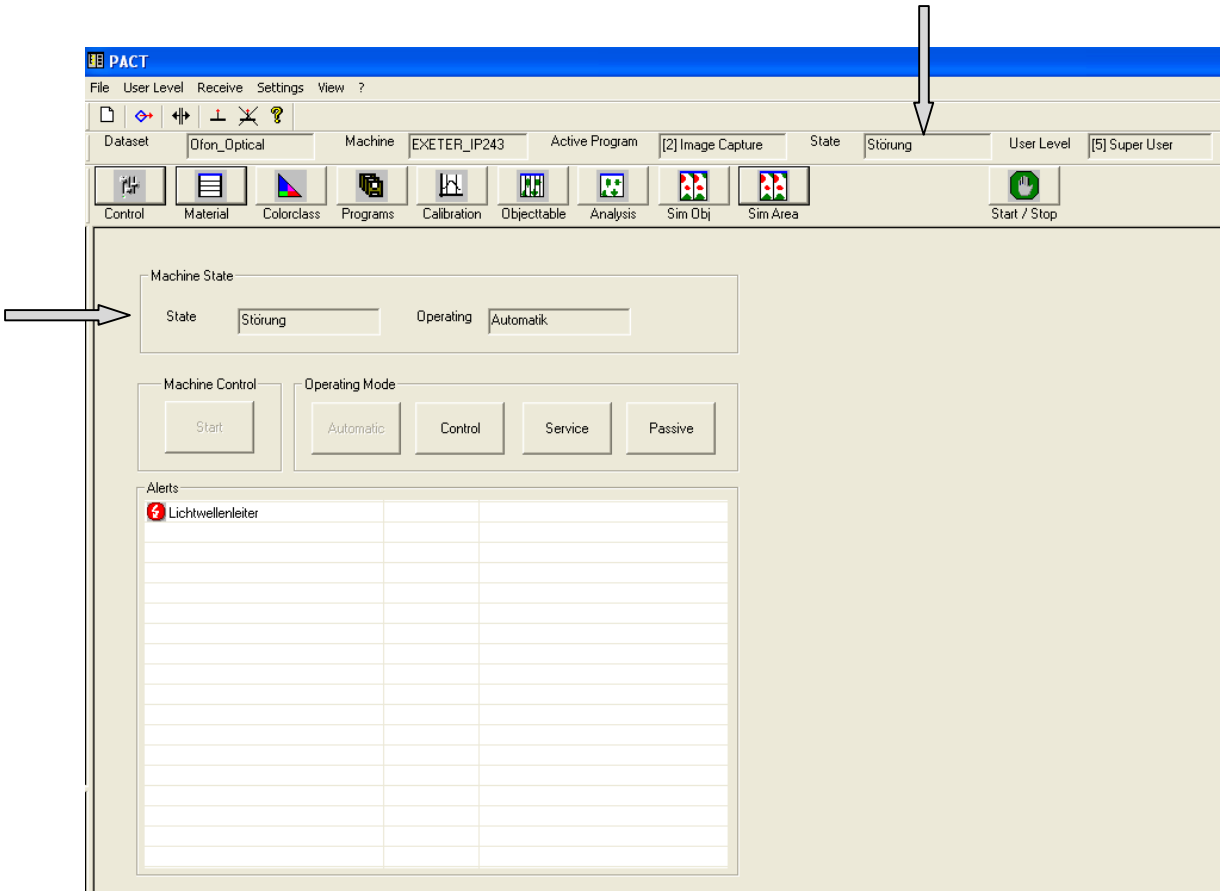

Figure 2: The control dialog box

Machine error alerts are also displayed in this tab. The sorter initializes in the 'automatic' operating mode the 'control' tab has to be selected to be able to manually control/operate the sorter. The service and passive tabs are not required.

The ***Material*** tab is where the major decision for sorting is undertaken and is discussed in Chapter 4 of the thesis. Figure 3 indicates the material tab.

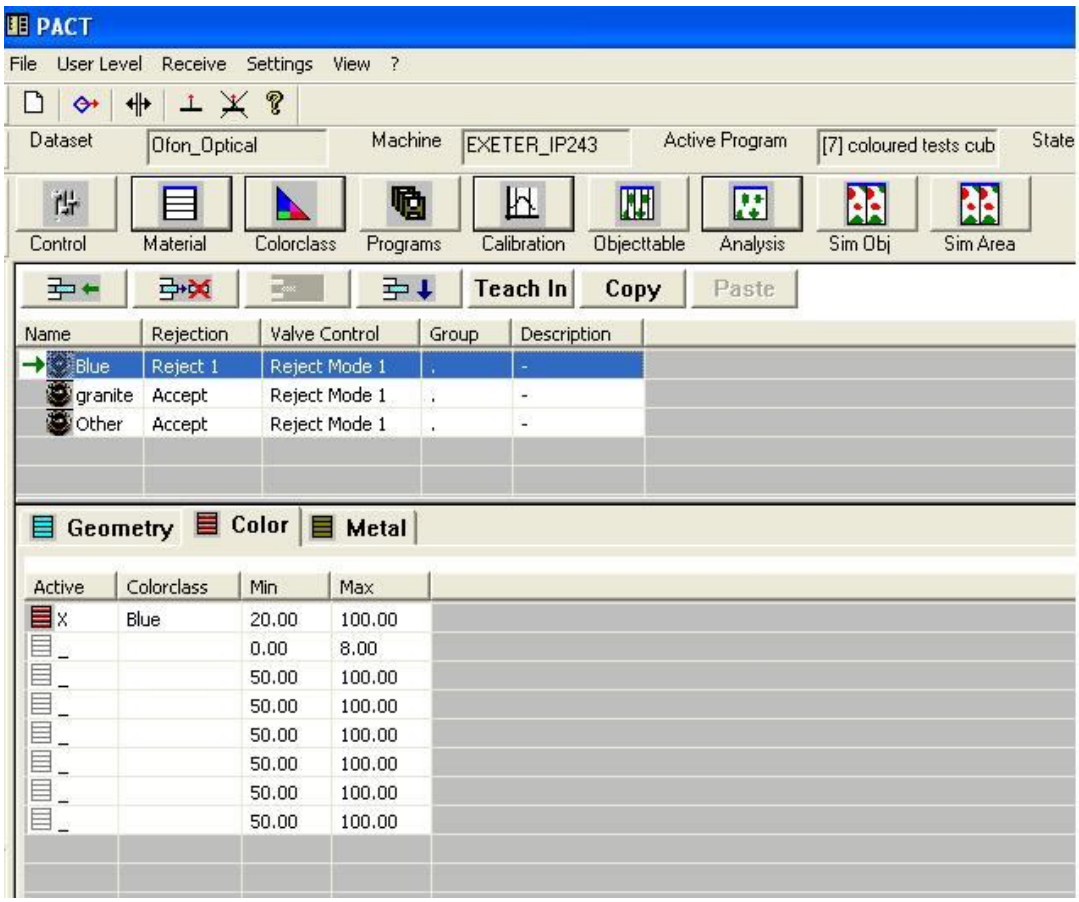

Figure 3: The material rule setting tab showing 'colour' only (this setting deflected blue coloured granite with a minimum of 20% blue content allowing the other materials to travel into the accept bin)

Three materials are utilized for separation (blue, granite and other) where the cut off setting for the blue material to be rejected is 20%. Rejection rule1 is utilized for deflection of the blue materials while the other two classes of materials are accepted.

After the colour of the samples have been calibrated utilizing the functions in the ***Analysis*** tab, the YUV values are input in the ***Colour class*** section indicated in Figure 4.

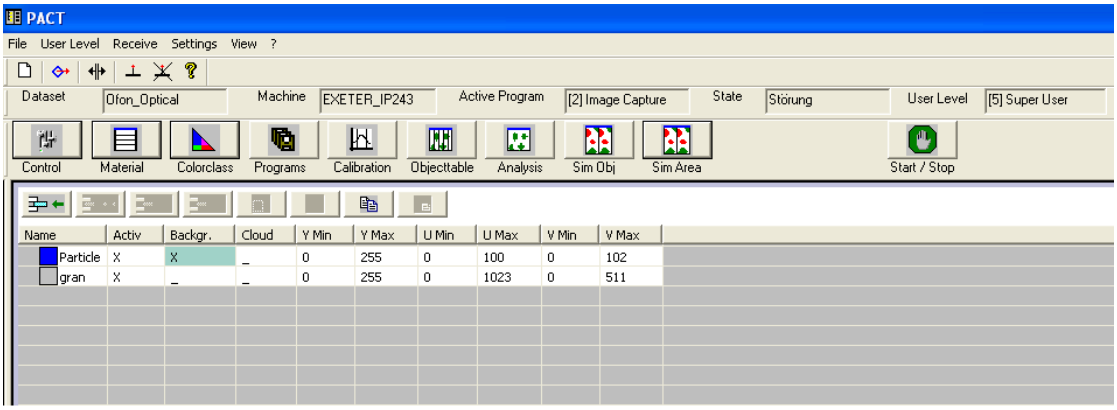

Figure 4: The colour class dialog box

Various program settings can be configured into the sorter by the operator based on the materials that require separation. The active program is highlighted by the green bullet point to the left of the program as indicated in Figure 5. To activate each program, the desired program is selected and the activate tab is depressed. Programs can be copied and utilized to build fresh calibrations.

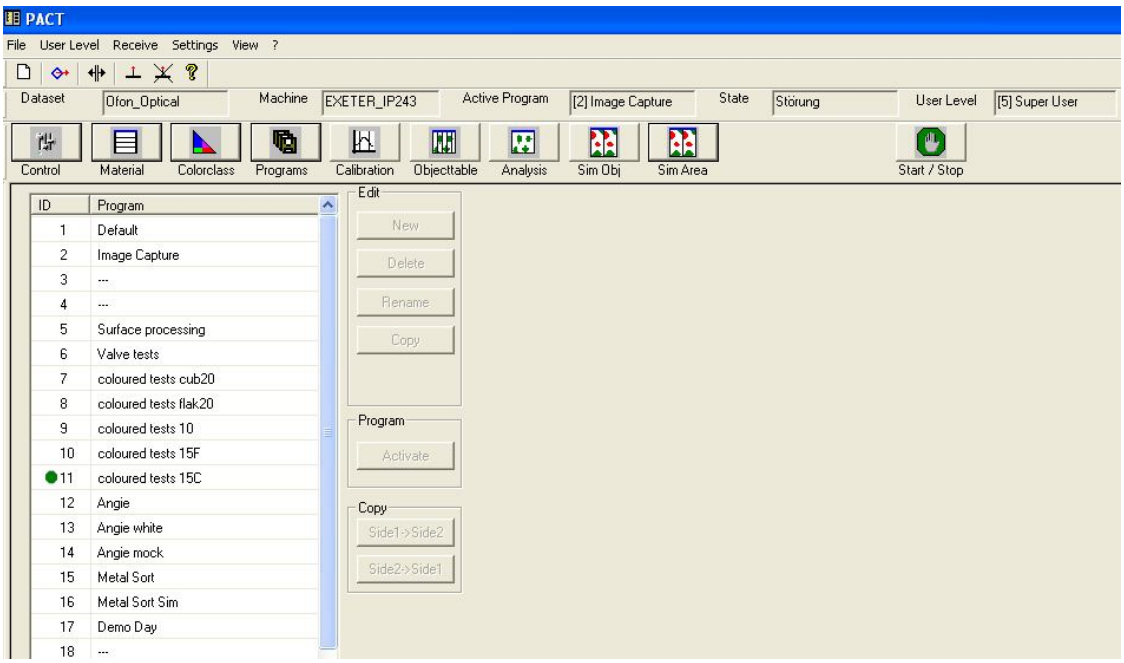

Figure 5: The programs dialog box

The ***calibration*** tab is where the exposure time, line time and various camera calibrations are undertaken. The black and white balances have to be correctly calibrated before camera tests are undertaken. When the balances are set right the BB and WB signs would be highlighted green. The ***object table*** tab discussed in Chapter five of the thesis is where the data recorded by the image capture device of the automated sorter are displayed. The last tab to be discussed is the ***Analysis*** tab indicated in Figure 6.

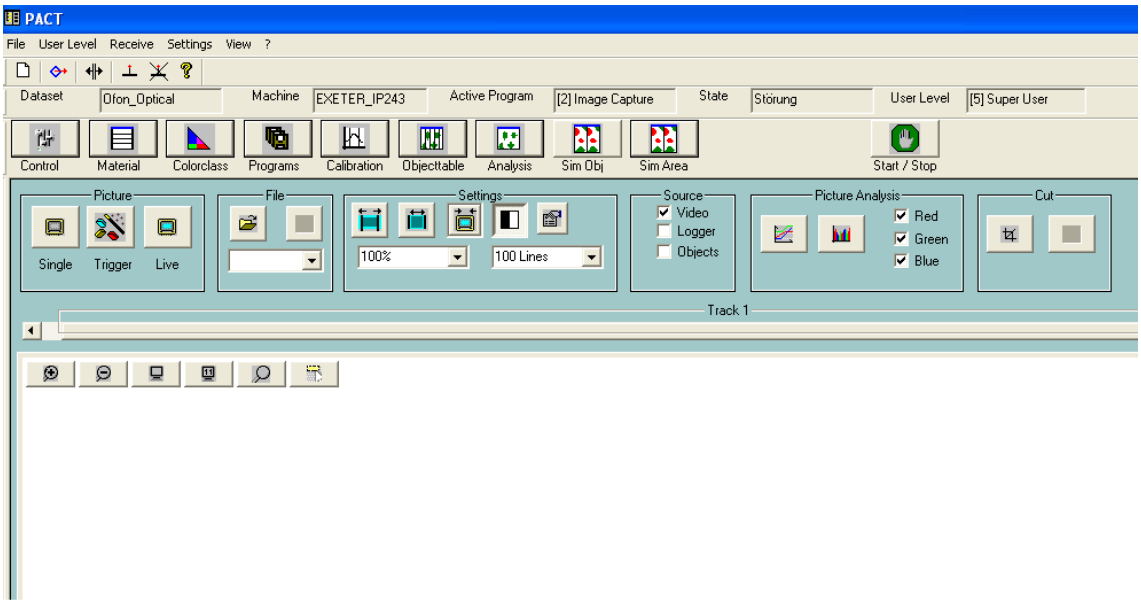

Figure 6: The analysis dialog box

This is where all the analyses of the sorted materials are undertaken. To capture the image for analysis, the 'picture' settings are utilized. A single picture, live picture or a picture is taken after a triggered event. The 'file' setting is utilized to save pictures acquired by the camera of the sorter. The 'settings' setting allows for the control of the number of lines which are scanned for analysis. The 'source' setting determines the video source. The 'picture analysis' setting is where the image is analysed extracting the YUV values which are input in the colour class section. The pictures can be analysed as histograms or graphs. The last group of settings is the 'cut' setting which serves for further image manipulation.

The data captured by the image processing device can be extracted into 23 components shown in Table 1.

Table 1: The image components extracted utilizing the image processing analyser of the TiTech automated sorter

Obj No.	Time	XMin	YMin	XMax	YMax	X Centre of Gravity	Y Centre of Gravity	Surface	Width	Height	Max Extend	Shape Factor	Homogen - eity	Moment1	Moment2	Aspect Ratio	Metal	Metal [%]	Blue	granite	Other	Pixel filter
4001	86872141	1180	1.74E+08	1214	1.74E+08	1196	9942054	656	35	24	1261	771428	110592	26317	-1.8E+09	520725	0	0	480	0	176	0
4002	86874540	1459	1.74E+08	1496	1.74E+08	1476	7683304	849	38	31	1493	700501	132843	17629	8.5E+08	569105	0	0	0	466	383	0
4003	86874911	404	1.74E+08	443	1.74E+08	423	7548273	864	40	30	1600	711250	116902	13569	8.69E+08	540546	0	0	0	589	275	0
4004	86876295	1498	1.74E+08	1532	1.74E+08	1514	10552745	618	35	24	1241	726785	135441	31534	-1.2E+09	498497	0	0	0	364	253	0
4005	86877635	997	1.74E+08	1040	1.74E+08	1019	7170229	910	44	28	1937	716507	129199	13689	6.76E+08	470043	0	0	0	697	212	0
4006	86878005	616	1.74E+08	650	1.74E+08	634	8027977	813	35	34	1241	664596	110219	15734	1.1E+09	655273	0	0	594	0	218	0
4007	86878388	1787	1.74E+08	1806	1.74E+08	1796	19976592	326	20	21	477	767857	94663	107607	-1	685110	0	0	0	12	314	0
4008	86878781	1535	1.74E+08	1564	1.74E+08	1549	17530480	372	30	16	936	742424	162115	81190	-1	397860	0	0	0	136	235	0
4009	86880278	1738	1.74E+08	1761	1.74E+08	1750	17179870	379	24	22	625	694444	139620	80814	-1	607995	0	0	0	82	297	0
4010	86880957	850	1.74E+08	876	1.74E+08	861	14559211	448	27	24	730	682870	118387	51862	-1	614242	0	0	0	319	129	0
4011	86881067	1182	1.74E+08	1209	1.74E+08	1194	13944699	468	28	25	833	647058	107817	49832	-1	562012	0	0	311	0	156	0
4012	86881310	1345	1.74E+08	1380	1.74E+08	1363	5981848	1091	36	41	1682	738683	108013	10907	3.1E+08	648841	0	0	784	0	307	0
4013	86881530	762	1.74E+08	787	1.74E+08	774	10710642	609	26	33	1186	701049	120403	28175	-8.2E+08	513925	0	0	3	408	197	0
4014	86881639	1438	1.74E+08	1474	1.74E+08	1453	10900932	598	37	25	1378	626391	118387	33004	-7.5E+08	434597	0	0	0	325	273	0
4015	86881717	753	1.74E+08	794	1.74E+08	773	6949785	939	42	36	2088	613095	108335	12210	6.1E+08	449881	0	0	740	0	199	0
4016	86881887	1300	1.74E+08	1353	1.74E+08	1328	6260885	1042	54	30	3141	635185	117274	11694	3.75E+08	331968	0	0	0	732	310	0
4017	86881969	747	1.74E+08	782	1.74E+08	764	6577285	992	36	42	1813	647817	100158	10967	4.89E+08	547464	0	0	784	0	208	0
4018	86882100	733	1.74E+08	772	1.74E+08	752	10129640	644	40	19	1616	815384	106496	25186	-1.5E+09	398809	0	0	0	500	144	0
4019	86882174	845	1.74E+08	896	1.74E+08	871	4735355	1378	52	39	2704	670857	144421	6055	1.28E+08	509848	0	0	1	1108	269	0

APPENDIX B - Shape test results

Table 1: Shape diameter test results for flaky shaped -20+15mm fraction

S/No.	X	Y	Z	Z/Y	Y/X
1	25	20	7	0.35	0.80
2	50	20	8	0.40	0.40
3	34	25	8	0.32	0.74
4	33	22	8	0.36	0.67
5	26	20	10	0.50	0.77
6	29	20	10	0.50	0.69
7	25	24	9	0.38	0.96
8	29	22	9	0.41	0.76
9	31	25	8	0.32	0.81
10	26	25	6	0.24	0.96
11	22	21	6	0.29	0.95
12	22	20	5	0.25	0.91
13	26	20	7	0.35	0.77
14	24	22	10	0.45	0.92
15	36	19	9	0.47	0.53
16	24	21	9	0.43	0.88
17	23	21	9	0.43	0.91
18	26	18	8	0.44	0.69
19	30	21	9	0.43	0.70
20	30	20	7	0.35	0.67
21	45	19	9	0.47	0.42
22	30	21	6	0.29	0.70
23	29	21	8	0.38	0.72
24	30	20	6	0.30	0.67
25	30	16	9	0.56	0.53
26	30	20	9	0.45	0.67
27	28	19	7	0.37	0.68
28	36	19	7	0.37	0.53
29	35	25	9	0.36	0.71
30	19	18	8	0.44	0.95
31	43	23	8	0.35	0.53
32	26	20	6	0.30	0.77
33	26	24	7	0.29	0.92
34	25	22	7	0.32	0.88
35	26	21	7	0.33	0.81
36	25	21	8	0.38	0.84
37	27	20	6	0.30	0.74
38	28	24	7	0.29	0.86
39	20	18	7	0.39	0.90
40	30	14	6	0.43	0.47
41	28	21	5	0.24	0.75
42	26	21	6	0.29	0.81
43	23	19	7	0.37	0.83
44	36	18	9	0.50	0.50
45	23	21	7	0.33	0.91
46	28	18	6	0.33	0.64
47	30	22	7	0.32	0.73
48	26	17	7	0.41	0.65

49	43	17	8	0.47	0.40
50	24	19	6	0.32	0.79
51	26	21	8	0.38	0.81
52	27	17	7	0.41	0.63
53	31	23	7	0.30	0.74
54	31	18	6	0.33	0.58
55	32	21	6	0.29	0.66
56	39	20	7	0.35	0.51
57	19	16	5	0.31	0.84
58	24	20	8	0.40	0.83
59	30	23	8	0.35	0.77
60	25	21	7	0.33	0.84
61	28	22	7	0.32	0.79
62	20	20	8	0.40	1.00
63	21	18	7	0.39	0.86
64	22	20	8	0.40	0.91
65	25	22	8	0.36	0.88
66	20	20	7	0.35	1.00
67	31	15	8	0.53	0.48
68	20	19	6	0.32	0.95
69	20	19	8	0.42	0.95
70	24	18	8	0.44	0.75
71	21	14	6	0.43	0.67
72	26	18	6	0.33	0.69
73	20	16	6	0.38	0.80
74	25	18	7	0.39	0.72
75	27	18	6	0.33	0.67
76	25	20	6	0.30	0.80
77	25	20	5	0.25	0.80
78	23	22	7	0.32	0.96
79	22	21	8	0.38	0.95
80	22	19	9	0.47	0.86
81	23	19	6	0.32	0.83
82	25	20	8	0.40	0.80
83	27	21	8	0.38	0.78
84	24	17	8	0.47	0.71
85	22	14	5	0.36	0.64
86	27	18	8	0.44	0.67
87	35	24	8	0.33	0.69
88	26	23	6	0.26	0.88
89	21	19	5	0.26	0.90
90	25	19	8	0.42	0.76
91	21	20	8	0.40	0.95
92	23	18	7	0.39	0.78
93	16	16	5	0.31	1.00
94	23	21	6	0.29	0.91
95	25	23	6	0.26	0.92
96	31	15	8	0.53	0.48
97	24	23	8	0.35	0.96
98	27	20	8	0.40	0.74
99	22	19	7	0.37	0.86
100	24	18	6	0.33	0.75

Table 2: Shape diameter test results for cubic shaped -20+15mm fraction

S/No.	X	Y	Z	Z/Y	Y/X
1	26	20	14	0.70	0.77
2	33	26	15	0.58	0.79
3	28	20	16	0.80	0.71
4	26	21	15	0.71	0.81
5	32	28	17	0.61	0.88
6	24	18	15	0.83	0.75
7	30	21	17	0.81	0.70
8	27	21	16	0.76	0.78
9	26	20	15	0.75	0.77
10	26	20	17	0.85	0.77
11	40	17	16	0.94	0.43
12	25	18	15	0.83	0.72
13	30	21	14	0.67	0.70
14	29	20	16	0.80	0.69
15	38	25	16	0.64	0.66
16	35	19	17	0.89	0.54
17	30	17	15	0.88	0.57
18	27	20	18	0.90	0.74
19	20	18	15	0.83	0.90
20	28	24	17	0.71	0.86
21	32	20	16	0.80	0.63
22	32	21	20	0.95	0.66
23	26	21	14	0.67	0.81
24	32	22	15	0.68	0.69
25	33	20	16	0.80	0.61
26	36	20	18	0.90	0.56
27	26	19	15	0.79	0.73
28	30	20	15	0.75	0.67
29	27	20	19	0.95	0.74
30	30	20	17	0.85	0.67
31	26	22	17	0.77	0.85
32	28	17	12	0.71	0.61
33	32	18	16	0.89	0.56
34	27	17	15	0.88	0.63
35	23	17	15	0.88	0.74
36	25	22	14	0.64	0.88
37	26	16	10	0.63	0.62
38	35	22	13	0.59	0.63
39	28	19	16	0.84	0.68
40	21	17	15	0.88	0.81
41	22	15	12	0.80	0.68
42	22	17	15	0.88	0.77
43	20	16	13	0.81	0.80
44	26	16	14	0.88	0.62
45	27	16	15	0.94	0.59
46	28	25	15	0.60	0.89
47	21	18	16	0.89	0.86
48	30	16	13	0.81	0.53
49	19	16	12	0.75	0.84
50	21	18	12	0.67	0.86

51	22	17	17	1.00	0.77
52	36	17	14	0.82	0.47
53	31	19	15	0.79	0.61
54	30	18	11	0.61	0.60
55	28	16	14	0.88	0.57
56	23	21	13	0.62	0.91
57	22	16	12	0.75	0.73
58	24	18	13	0.72	0.75
59	23	18	14	0.78	0.78
60	19	16	10	0.63	0.84
61	20	15	14	0.93	0.75
62	25	15	13	0.87	0.60
63	30	16	14	0.88	0.53
64	25	18	17	0.94	0.72
65	22	16	14	0.88	0.73
66	25	17	12	0.71	0.68
67	27	15	13	0.87	0.56
68	21	18	13	0.72	0.86
69	19	17	14	0.82	0.89
70	31	15	14	0.93	0.48
71	21	16	15	0.94	0.76
72	25	20	18	0.90	0.80
73	31	19	17	0.89	0.61
74	28	18	15	0.83	0.64
75	25	17	10	0.59	0.68
76	20	19	12	0.63	0.95
77	26	20	13	0.65	0.77
78	24	15	14	0.93	0.63
79	22	14	13	0.93	0.64
80	21	17	14	0.82	0.81
81	22	18	14	0.78	0.82
82	30	19	15	0.79	0.63
83	25	15	13	0.87	0.60
84	19	17	15	0.88	0.89
85	24	16	15	0.94	0.67
86	32	16	12	0.75	0.50
87	36	20	18	0.90	0.56
88	22	20	18	0.90	0.91
89	25	17	14	0.82	0.68
90	29	18	15	0.83	0.62
91	22	20	14	0.70	0.91
92	24	17	15	0.88	0.71
93	27	16	12	0.75	0.59
94	32	16	13	0.81	0.50
95	29	19	12	0.63	0.66
96	22	22	11	0.50	1.00
97	22	18	15	0.83	0.82
98	21	19	13	0.68	0.90
99	36	18	15	0.83	0.50
100	33	20	18	0.90	0.61

Table 3: Shape diameter test results for flaky shaped -15+10mm fraction

S/No.	X	Y	Z	Z/Y	Y/X
1	29	14	8	0.57	0.48
2	26	18	8	0.44	0.69
3	16	15	7	0.47	0.94
4	33	12	6	0.50	0.36
5	26	16	8	0.50	0.62
6	28	12	7	0.58	0.43
7	24	18	3	0.17	0.75
8	21	9	8	0.89	0.43
9	20	16	7	0.44	0.80
10	29	18	9	0.50	0.62
11	26	21	7	0.33	0.81
12	17	14	9	0.64	0.82
13	21	17	7	0.41	0.81
14	35	15	7	0.47	0.43
15	16	14	10	0.71	0.88
16	37	12	6	0.50	0.32
17	32	18	8	0.44	0.56
18	26	15	7	0.47	0.58
19	23	13	8	0.62	0.57
20	22	15	7	0.47	0.68
21	31	13	7	0.54	0.42
22	23	15	7	0.47	0.65
23	25	17	6	0.35	0.68
24	24	17	8	0.47	0.71
25	22	17	7	0.41	0.77
26	17	13	8	0.62	0.76
27	25	16	8	0.50	0.64
28	48	12	7	0.58	0.25
29	30	17	6	0.35	0.57
30	30	10	9	0.90	0.33
31	21	15	7	0.47	0.71
32	22	13	8	0.62	0.59
33	18	12	8	0.67	0.67
34	23	13	8	0.62	0.57
35	23	20	6	0.30	0.87
36	28	17	7	0.41	0.61
37	28	15	7	0.47	0.54
38	20	18	8	0.44	0.90
39	21	15	8	0.53	0.71
40	28	18	5	0.28	0.64
41	24	15	6	0.40	0.63
42	27	18	7	0.39	0.67
43	28	17	8	0.47	0.61
44	37	18	8	0.44	0.49
45	20	17	6	0.35	0.85
46	22	15	6	0.40	0.68
47	28	15	4	0.27	0.54
48	20	15	8	0.53	0.75
49	21	17	6	0.35	0.81
50	20	12	6	0.50	0.60

51	22	13	7	0.54	0.59
52	20	13	6	0.46	0.65
53	37	14	8	0.57	0.38
54	25	14	8	0.57	0.56
55	30	13	7	0.54	0.43
56	29	15	7	0.47	0.52
57	26	17	9	0.53	0.65
58	22	14	7	0.50	0.64
59	20	11	7	0.64	0.55
60	24	17	6	0.35	0.71
61	25	15	3	0.20	0.60
62	17	12	8	0.67	0.71
63	18	14	6	0.43	0.78
64	18	12	4	0.33	0.67
65	28	16	8	0.50	0.57
66	17	16	5	0.31	0.94
67	27	11	8	0.73	0.41
68	27	16	7	0.44	0.59
69	21	15	8	0.53	0.71
70	20	17	8	0.47	0.85
71	22	12	8	0.67	0.55
72	14	13	7	0.54	0.93
73	17	14	7	0.50	0.82
74	19	12	8	0.67	0.63
75	35	17	7	0.41	0.49
76	26	17	7	0.41	0.65
77	25	15	8	0.53	0.60
78	26	14	7	0.50	0.54
79	23	14	6	0.43	0.61
80	17	16	8	0.50	0.94
81	16	12	7	0.58	0.75
82	27	18	6	0.33	0.67
83	19	15	9	0.60	0.79
84	17	14	7	0.50	0.82
85	23	19	6	0.32	0.83
86	20	12	9	0.75	0.60
87	20	11	8	0.73	0.55
88	31	15	9	0.60	0.48
89	28	15	4	0.27	0.54
90	31	22	5	0.23	0.71
91	21	14	7	0.50	0.67
92	24	13	8	0.62	0.54
93	24	14	7	0.50	0.58
94	31	14	7	0.50	0.45
95	29	14	6	0.43	0.48
96	17	15	5	0.33	0.88
97	24	13	6	0.46	0.54
98	22	14	4	0.29	0.64
99	18	16	7	0.44	0.89
100	19	17	8	0.47	0.89

Table 4: Shape diameter test results for cubic shaped -15+10mm fraction

S/No.	X	Y	Z	Z/Y	Y/X
1	20	13	12	0.92	0.65
2	22	14	10	0.71	0.64
3	27	13	11	0.85	0.48
4	19	14	11	0.79	0.74
5	29	19	11	0.58	0.66
6	38	11	9	0.82	0.29
7	29	17	9	0.53	0.59
8	23	16	13	0.81	0.70
9	32	13	9	0.69	0.41
10	24	13	10	0.77	0.54
11	24	16	11	0.69	0.67
12	16	14	11	0.79	0.88
13	26	19	11	0.58	0.73
14	28	14	11	0.79	0.50
15	21	11	9	0.82	0.52
16	23	15	10	0.67	0.65
17	25	14	13	0.93	0.56
18	18	13	12	0.92	0.72
19	34	14	9	0.64	0.41
20	16	14	13	0.93	0.88
21	26	11	10	0.91	0.42
22	19	15	11	0.73	0.79
23	27	16	8	0.50	0.59
24	42	17	9	0.53	0.40
25	40	13	10	0.77	0.33
26	29	15	11	0.73	0.52
27	24	14	13	0.93	0.58
28	26	13	10	0.77	0.50
29	27	15	10	0.67	0.56
30	30	15	11	0.73	0.50
31	20	13	9	0.69	0.65
32	19	15	10	0.67	0.79
33	19	18	9	0.50	0.95
34	18	13	9	0.69	0.72
35	18	15	9	0.60	0.83
36	38	11	9	0.82	0.29
37	18	12	10	0.83	0.67
38	16	15	9	0.60	0.94
39	27	15	10	0.67	0.56
40	29	14	9	0.64	0.48
41	20	17	11	0.65	0.85
42	30	14	11	0.79	0.47
43	36	11	10	0.91	0.31
44	40	15	10	0.67	0.38
45	25	13	11	0.85	0.52
46	20	13	11	0.85	0.65
47	18	15	9	0.60	0.83
48	27	10	10	1.00	0.37
49	18	15	9	0.60	0.83
50	18	14	10	0.71	0.78

51	20	17	9	0.53	0.85
52	32	14	12	0.86	0.44
53	26	13	10	0.77	0.50
54	23	16	11	0.69	0.70
55	26	11	10	0.91	0.42
56	23	21	10	0.48	0.91
57	18	12	11	0.92	0.67
58	25	16	10	0.63	0.64
59	23	15	9	0.60	0.65
60	19	14	11	0.79	0.74
61	22	13	10	0.77	0.59
62	27	13	9	0.69	0.48
63	28	16	11	0.69	0.57
64	37	16	13	0.81	0.43
65	34	14	12	0.86	0.41
66	20	15	11	0.73	0.75
67	25	13	9	0.69	0.52
68	26	14	13	0.93	0.54
69	21	11	9	0.82	0.52
70	24	15	10	0.67	0.63
71	22	13	10	0.77	0.59
72	28	14	9	0.64	0.50
73	20	13	10	0.77	0.65
74	18	13	11	0.85	0.72
75	30	14	10	0.71	0.47
76	31	17	9	0.53	0.55
77	38	12	9	0.75	0.32
78	28	12	10	0.83	0.43
79	24	16	11	0.69	0.67
80	27	14	10	0.71	0.52
81	24	14	9	0.64	0.58
82	24	15	9	0.60	0.63
83	24	15	10	0.67	0.63
84	22	14	12	0.86	0.64
85	30	17	12	0.71	0.57
86	20	14	12	0.86	0.70
87	17	14	11	0.79	0.82
88	18	14	10	0.71	0.78
89	30	15	10	0.67	0.50
90	29	15	12	0.80	0.52
91	29	16	11	0.69	0.55
92	27	14	9	0.64	0.52
93	31	12	11	0.92	0.39
94	21	13	12	0.92	0.62
95	22	15	13	0.87	0.68
96	21	14	9	0.64	0.67
97	20	10	9	0.90	0.50
98	19	12	12	1.00	0.63
99	28	12	11	0.92	0.43
100	26	12	10	0.83	0.46

Table 5: Shape diameter test results for -10+6mm fraction

S/No.	X	Y	Z	Z/Y	Y/X
1	12	8	7	0.88	0.67
2	11	6	4	0.67	0.55
3	18	8	6	0.75	0.44
4	11	8	4	0.50	0.73
5	15	8	5	0.63	0.53
6	11	10	4	0.40	0.91
7	17	11	6	0.55	0.65
8	12	7	7	1.00	0.58
9	13	11	5	0.45	0.85
10	7	7	6	0.86	1.00
11	11	9	5	0.56	0.82
12	10	7	5	0.71	0.70
13	10	8	3	0.38	0.80
14	11	10	7	0.70	0.91
15	12	11	5	0.45	0.92
16	10	9	5	0.56	0.90
17	11	7	4	0.57	0.64
18	12	7	6	0.86	0.58
19	10	7	5	0.71	0.70
20	16	6	5	0.83	0.38
21	13	9	4	0.44	0.69
22	14	8	6	0.75	0.57
23	11	10	4	0.40	0.91
24	9	8	5	0.63	0.89
25	10	9	5	0.56	0.90
26	11	8	7	0.88	0.73
27	9	5	5	1.00	0.56
28	10	6	5	0.83	0.60
29	13	8	4	0.50	0.62
30	13	7	4	0.57	0.54
31	13	9	6	0.67	0.69
32	13	8	7	0.88	0.62
33	9	8	6	0.75	0.89
34	11	10	4	0.40	0.91
35	13	9	4	0.44	0.69
36	12	10	5	0.50	0.83
37	10	10	5	0.50	1.00
38	12	5	4	0.80	0.42
39	13	9	7	0.78	0.69
40	12	11	4	0.36	0.92
41	12	9	7	0.78	0.75
42	10	9	5	0.56	0.90
43	12	7	7	1.00	0.58
44	15	9	7	0.78	0.60
45	14	9	6	0.67	0.64
46	21	9	6	0.67	0.43
47	17	8	5	0.63	0.47
48	14	10	5	0.50	0.71
49	22	7	6	0.86	0.32
50	9	6	5	0.83	0.67

51	9	6	5	0.83	0.67
52	12	6	5	0.83	0.50
53	12	8	5	0.63	0.67
54	15	9	5	0.56	0.60
55	13	5	4	0.80	0.38
56	10	8	5	0.63	0.80
57	14	10	6	0.60	0.71
58	15	7	6	0.86	0.47
59	9	7	6	0.86	0.78
60	10	8	6	0.75	0.80
61	14	7	5	0.71	0.50
62	12	8	5	0.63	0.67
63	14	8	6	0.75	0.57
64	11	11	6	0.55	1.00
65	11	9	6	0.67	0.82
66	14	7	4	0.57	0.50
67	11	9	6	0.67	0.82
68	14	10	4	0.40	0.71
69	15	7	6	0.86	0.47
70	18	10	6	0.60	0.56
71	13	10	7	0.70	0.77
72	9	8	5	0.63	0.89
73	11	8	8	1.00	0.73
74	12	9	7	0.78	0.75
75	13	7	5	0.71	0.54
76	14	11	9	0.82	0.79
77	10	9	7	0.78	0.90
78	18	8	5	0.63	0.44
79	15	10	5	0.50	0.67
80	11	10	6	0.60	0.91
81	13	8	6	0.75	0.62
82	15	9	8	0.89	0.60
83	8	8	7	0.88	1.00
84	10	8	5	0.63	0.80
85	21	8	6	0.75	0.38
86	12	10	7	0.70	0.83
87	12	7	6	0.86	0.58
88	11	8	5	0.63	0.73
89	12	7	5	0.71	0.58
90	17	10	8	0.80	0.59
91	11	10	6	0.60	0.91
92	15	10	5	0.50	0.67
93	15	9	5	0.56	0.60
94	10	8	5	0.63	0.80
95	16	11	5	0.45	0.69
96	13	9	6	0.67	0.69
97	16	11	4	0.36	0.69
98	16	10	5	0.50	0.63
99	10	6	4	0.67	0.60
100	13	7	4	0.57	0.54

APPENDIX C – Separation efficiency test results of all size fractions used to determine standard deviation

Stated in Tables 1 to 3 are the results of repeats of separation efficiency tests for the -20+15, -15+10mm and -10+6mm fractions.

Table 1: Separation efficiency at varying blue % deflect and throughputs for the -20+15mm sample fraction

		SEPARATION EFFICIENCY								
		0.5tonnes/hr			1.5tonnes/hr			2.5tonnes/hr		
		10%	*30%*	*50%*	*10%*	*30%*	*50%*	*10%*	*30%*	*50%*
Flaky										
Repeats	**1**	98.9	97.1	96.8	97.6	93.5	90.4	96.0	88.1	83.4
	2	99.5	97.7	96.5	98.0	93.5	92.9	95.3	87.9	79.9
	3	99.0	97.7	95.7	97.2	94.2	89.1	96.1	84.9	81.0
	4	99.1	97.9	97.0	96.8	92.1	90.5	93.8	87.7	82.9
Standard dev.		0.26	0.35	0.57	0.52	0.88	1.58	1.06	1.51	1.64
Cubic										
Repeats	**1**	96.3	97.3	94.9	95.4	95.1	94.9	95.3	91.9	89.4
	2	99.6	94.9	97.3	95.9	93.5	93.9	96.0	91.0	90.3
	3	96.0	97.2	96.1	92.5	95.1	92.7	96.2	93.5	91.3
	4	97.3	96.3	93.6	95.4	91.2	95.2	97.9	92.6	89.2
Standard dev.		1.63	1.11	1.59	1.55	1.84	1.13	1.10	1.06	0.96

Table 2: Separation efficiency at varying blue % deflect and throughputs for the -15+10mm sample fraction

		SEPARATION EFFICIENCY								
		0.5tonnes/hr			1.5tonnes/hr			2.5tonnes/hr		
		10%	*30%*	*50%*	*10%*	*30%*	*50%*	*10%*	*30%*	*50%*
Flaky										
Repeats	1	99.0	97.6	95.9	97.2	94.1	92.3	95.7	87.8	83.8
	2	99.0	97.6	96.7	98.2	93.4	89.4	96.0	87.7	79.5
	3	99.1	97.7	96.4	97.4	92.2	88.5	95.1	86.9	80.4
	4	99.1	97.8	97.4	97.5	92.6	88.0	95.0	87.0	81.0
Standard dev.		0.06	0.10	0.63	0.43	0.85	1.92	0.48	0.47	1.86
Cubic										
Repeats	1	99.2	98.3	97.8	98.3	94.9	94.8	97.6	93.4	86.0
	2	99.8	97.8	97.2	97.9	96.4	95.0	96.4	91.6	89.0
	3	99.8	98.1	97.8	97.9	96.8	93.6	98.3	92.9	88.4
	4	99.0	98.3	98.6	98.3	94.9	93.0	97.1	92.3	87.0
Standard dev.		0.41	0.24	0.57	0.23	0.99	0.96	0.80	0.78	1.36

Table 3: Separation efficiency at varying blue % deflect and throughputs for the -10+6mm sample fraction

		SEPARATION EFFICIENCY							
		0.5tonnes/hr			1.5tonnes/hr			2.5tonnes/hr	
		10%	*30%*	*50%*	*10%*	*30%*	*50%*	*10%*	*30%*
Repeats	1	98.2	95.6	93.7	94.7	85.1	79.6	90	72.7
	2	98.4	94.9	93.1	94.6	81.0	79.6	89.6	73.6
	3	98.3	94.5	92.6	95.1	82.5	76.3	90.9	-
	4	98.0	95.1	91.2	93.1	83.6	75.0	-	-
Standard dev.		0.17	0.46	1.07	0.88	1.70	2.34	0.67	0.64